Electrical and Thermal Transport Measurements on Nano-structured Materials

by

Chih-Wei Chang

B.S. (National Taiwan University) 1996

M.S. (National Taiwan University) 1998

A dissertation submitted in partial fulfillment of the requirements for the degree of

Doctor of Philosophy

in

Physics

in the

GRADUATE DIVISION

of the

UNIVERSITY OF CALIFORNIA, BERKELEY

Committee in charge:

Professor Alex Zettl, Chair

Professor Steven G. Louie

Professor Peidong Yang

Fall 2006

The dissertation of Chih-Wei Chang is approved:

_____

Chair Date

_____

Date

_____

Date

University of California, Berkeley

Fall 2006

Electrical and Thermal Transport Measurements on Nano-structured Materials

By

Chih-Wei Chang

Abstract

Electrical and Thermal Transport Measurements of Nano-structured Materials

by

Chih-Wei Chang

Doctor of Philosophy in Physics

University of California, Berkeley

Professor Alex Zettl, Chair

This thesis discusses electrical and thermal transport measurements on C_{60}, carbon nanotubes, and boron-nitride nanotubes. Chapter 1 describes the anomalous resistivity behavior of Ag films on C_{60} crystals. The correlation of the resistivity anomaly and the structural phase transition is established. Chapter 2 gives an introduction to the physical properties and the synthesis methods of carbon and boron nitride nanotubes. Chapter 3 shows two different approaches on chemical functionalization of boron-nitride nanotubes. Chapter 4 gives the theoretical background of thermal conductivity, especially for nano-structured materials. A summary of theoretical and experimental works on the thermal conductivity of nanotubes is given. Chapter 5 discusses the experimental results of thermal conductivity of nanotube mats. An absolute value of the thermal conductivity of boron nitride nanotubes is bracketed and can be compared to the results of the following chapters on individual nanotubes. Chapter 6 describes the experimental methods of measuring thermal conductivity of individual nanotubes. Chapter 7 shows the

temperature dependent thermal conductivity and thermopower of individual nanotubes. Chapter 8 discusses the isotope effect and the diameter dependence of the thermal conductivity of nanotubes. In chapter 9, it is shown that the thermal conductivity of nanotubes is robust against electron irradiation and structural deformation. Importantly, the observation challenges current understandings on the thermal transport of nano-structured materials. In chapter 10, it is shown that it is possible to reversibly tune the thermal conductivity of a multiwalled nanotube by controllably sliding the outer-shells against inner cores. Chapter 11 describes a thermal rectifier by engineering the mass distribution along a nanotube. The observed non-zero thermal rectification effect provides strong evidence for solitons in nanotubes. The soliton model also coherently explains many phenomena described in chapter 10 and chapter 12. In chapter 12, it is shown that Fourier's law is violated in nanotubes and the observed anomalous heat transport is consistent with the soliton model. The significance of these discoveries can provide new thoughts for current thermal management problems. Based on these results, it is proposed to utilize phonons as information carriers.

_____

Professor Alex Zettl

Dissertation Committee Chair

To my parents

Table of Contents

List of Figures

List of Tables

Acknowledgements

First of all, I would like to thank my advisor, Alex Zettl. Alex's hand-off style not only made me enjoy the excitements of doing scientific research but also cultivated a young student into a scientist. I still remember the day when I was naïve but too ambitious, and was overwhelmed by my ideas: ranging from synthesizing room temperature superconductors to probing electrons in four-dimensional materials. When hearing these ideas, Alex did not discourage me but he clearly knew that I was at the edge of becoming a mediocre researcher. He advised me to stay focus on a practical project, which has continued to benefit me. Although today I am still driven by crazy ideas, without Alex's guidance, I would have achieved nothing.

I have been benefited from many people in the Zettl group. John Cummings served me as a scientific model. Masa Ishigami always gave frank opinions and was instrumental when I joined the lab. Adam Fennimore helped the thermal conductivity project in all aspects. Anderi Afanasiev and I shared many frustrating moments during the early days of the thermal conductivity project. Hope they are happy to see the project has finally brought fruitful results. I appreciate Xiaosheng Huang for showing me the technique of high pressure diamond anvil cell. Willi Mickelson and I have collaborated from moving the glass shop to dreaming high temperature superconductors. Tom Yuzvinsky always keeps the SEM in its highest morale. Kevin Jones and I always enjoy sharing crazy ideas to each other. Xing Chen is always ambitious. Gavi Begtrup is a constant source of entertainment. Kenny Jensen is full of capabilities that I admire.

Sharing Çağlar Girit's enthusiasm on his research reminds me how lucky I am for being a scientist. David Okawa's success in synthesizing BN nanotubes is of crucial importance to my experiments. And this success will not happen without his patience, diligence and perseverance. Henry Garcia has also made high quality carbon nanotubes. Other fresh minds, Brian Kessler, Michael Rousseas and Benjamín Alemán will help the group go into a new future. Members in the Majumdar group, Deyu Li and Renkun Chen, have made excellent devices that are indispensable to my experiments.

I have learned a lot of things from the postdoctoral researchers. Shaul Aloni, as Alex said, is the center of the universe and knows every detail about all technical stuffs. Weiqiang Han is always able to make magic samples. Chris Regan is the person willing to answer my questions about fundamental physics. Andras Kis is capable of doing any experiments. Haibing Peng is generous in sharing his knowledge. Takashi Ikuno has taught me everything from TEM techniques to speaking Japanese.

Many friends from Taiwan have made Berkeley like a second home to me. The fierce debates, ranging from physical problems to political issues, between the members of our weekly lunch meetings: Chih-Hao Li, Dah-Wei Chiou, Chih-Wei Lai and Yun-Pei Chang, have become the most memorable days while studying at Berkeley. I also cherish the moments with Sherry Cho, Cheng-Han Yu, I-Sheng Yang, Tzu-Ching Chang, ChengEn Wu, and Roland Jiang.

All of these would not be possible without the constant supports from my parents.

Chapter 1 Anomalous resistivity behaviors of Ag films on C_{60} crystals

1.1 Introduction to C_{60} crystals

C_{60}, the most symmetric molecule known, was discovered by H. W. Kroto *et al.* [1]. The original motivation for that study was to look for inter-galaxial molecules that are exclusively composed of carbon atoms. In order to compare the optical absorption spectrum of such molecules, Kroto *et al.* prepared soot from laser-ablated graphite and observed several peaks in the mass-spectrum. Later its structure was identified as being similar to the geodesic domes of the architect Buckminister Fuller. Hence the C_{60} molecules were called fullerenes. However, intensive research of C_{60} was only possible after W. Krätschmer and D. Huffman discovered bulk arc-discharge synthesis and purification methods for C_{60} [2]. Subsequently, families of fullerenes were discovered using similar techniques, including C_{36}, C_{70}, C_{128}, etc.

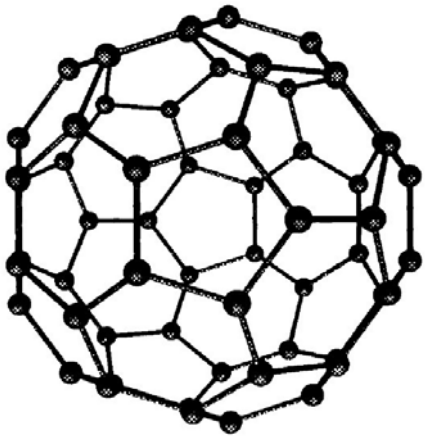

Figure 1-1 The structure of a C_{60} molecule

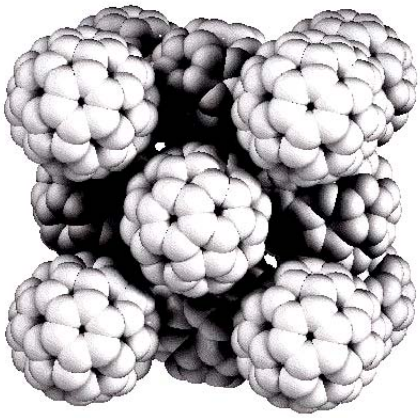

Figure 1-2 A C_{60} crystal of fcc structure

Figures 1-1 and 1-2 show the structures of C_{60} molecules and C_{60} crystals. C_{60} crystals can be made by subliming C_{60} molecules in an Ar atmosphere. At room temperature the C_{60} crystal is fcc with each C_{60} molecule in nearly free rotation. Upon cooling through 261K the C_{60} molecules lose two rotational degrees of freedom and acquire strong orientational correlation with their neighbors, ratcheting around one of the four <111> axes. This rotational ordering transition is also a first order fcc to sc structural transition [3]. At a surface, the effect of reduced symmetry lowers the corresponding transition to ~230K [4]. Cooling below 261K slows the ratcheting, stopping it entirely near 50K in the bulk sample. However, because there are two nearly degenerate (~11.4 meV) orientations separated by a substantial (290 meV) potential barrier, the rotational ordering is incomplete even in the low temperature limit. Below 90K the occupation of the nearly degenerate states does not change, so this temperature is identified with the quenched disorder transition [5].

Alkali-doped solid C_{60} has been known to be superconducting with T_c = 19K~30K [6,7]. Due to charge transfer, it is possible to dope the surface of a C_{60} crystal by depositing thin metal films on it. If the underlying C_{60} crystal becomes superconducting, it will create a short circuit to the whole system and result in a resistance drop. In addition, a photoemission experiment paper that suggested an observation of superconductivity of a C_{60} monolayer on an Ag(111) surface directly motivated this work [8]. Amazingly, the photoemission experiment indicated a BCS-like gap at 250K, though this result is not confirmed by subsequent STM spectroscopy measurements [9]. Furthermore, a series of papers by H. Schön *et al.* claiming discoveries of high T_c superconductivity in field-gated C_{60} crystals also motivated this work. But it was later found that these discoveries were due to scientific misconduct of H. Schön [10].

In order to unravel the interaction between metal films and C_{60} crystals, and also to search for superconductivity in these systems, I have systematically measured the temperature dependent resistivity of different metal films with various thicknesses on C_{60} crystals.

1.2 Sample preparation

C_{60} crystals were grown by subliming powder from MER Corporation (99.5% purity) in a flowing Ar atmosphere. The crystals so produced were several millimeters in size and had flat surfaces. Metal films (Ag, Au, Cu, Pd, Pt) were dc-sputtered onto a crystal face to various thicknesses as determined by a 6 MHz quartz-crystal monitor. Generally the deposition rate was controlled at 0.1nm/sec. Silver paint contacts on the metal films

were used for four-probe quasi-dc electrical resistance measurements. A helium gas-flow probe provided cooling from room temperature down to ~16K. Both cooling and warming gave consistent results, but only warming data will be presented because of its superior temperature resolution.

1.3 Results and discussions

Figure 1-3(a) shows a scanning electron microscope (SEM) image of a nominally 10nm thick Ag film deposited on C_{60}. The film is not uniform, but is granular with an average feature size of ~10nm and has a morphology reminiscent of thin film percolation networks. Electrical measurements at room temperature on this film indicate an average resistivity $\rho \sim 6$ μΩ-cm, ignoring the film inhomogeneity. As expected, this value significantly exceeds the resistivity ρ ~1.6 μΩ-cm usually observed for high quality homogeneous Ag specimens.

Figure 1-3(b) shows the temperature dependent resistance *R(T)* of a 10 nm thick Ag film on C_{60}, similar to the one pictured in Fig. 1-3(a). Relative to the typical behavior of Ag films on benign substrates, several anomalies are present in Fig. 1-3(b). First, instead of displaying linear temperature dependence, there is a slope change near 100K. Second, as the sample warms through 240K, the resistance decreases, reaching a minimum value (0.17 Ω) even smaller than the residual resistance (~0.18 Ω). Third, at 261K the resistance shows a very sharp jump upward with increasing temperature. Fourth, for $T >$ 261K, although the *R(T)* curve becomes linear again, its slope is not the same as that between 100K~240K. Control experiments with Ag films similarly deposited on mica or

glass substrates do not show any of these anomalies. As I will discuss later in this chapter, the three anomalies of Fig. 1-3(b) at T = 100K, 240K, and 260K are associated with well-known structural phase transitions of the underlying C_{60} crystal.

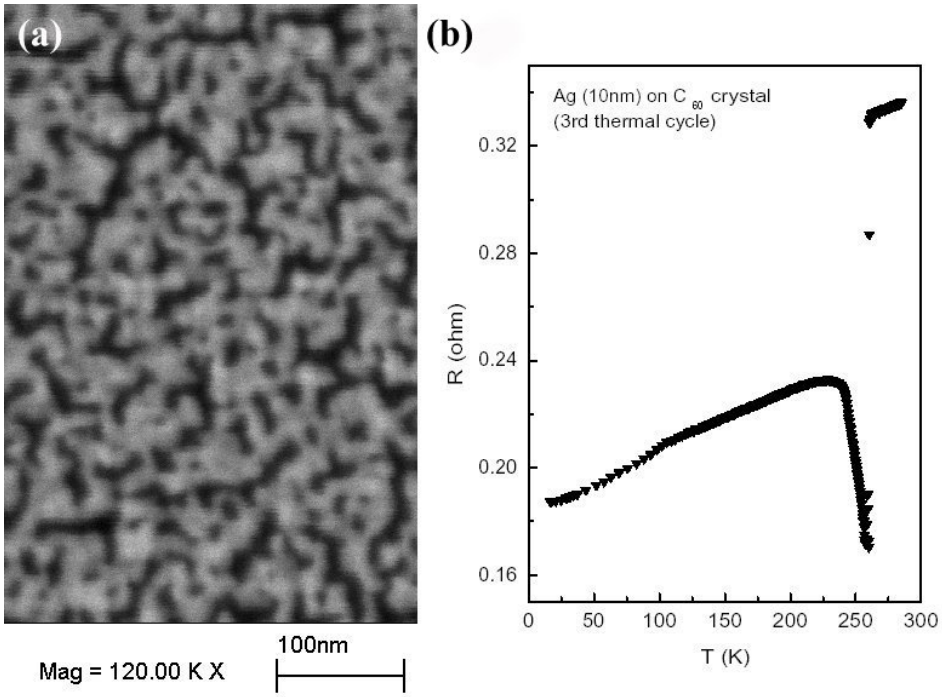

Figure 1-3 (a) Scanning electron micrograph of a 10 nm silver film on a C_{60} crystal. Scale bar is 100nm. (b) Resistance vs. temperature for a similar film.

The measurements described above have been repeated as a function of sample thermal history, for different Ag film thicknesses, and for films composed of different metals. Figure 1-4(a) and (b) show the *R(T)* curves of 5nm and 10 nm Ag film over multiple thermal cycles (only warming curves are shown for clarity). The residual resistance increases monotonically with thermal cycling, and the anomalous behavior between 240K and 261K becomes more dramatic. The resistance dip near 240K is not pronounced at first, but becomes effectively deeper, finally reaching a minimum value

even lower than the residual resistance. The resistance jump at 261K also increases with thermal cycling, as well as the slope of *R(T)* between 100K~240K.

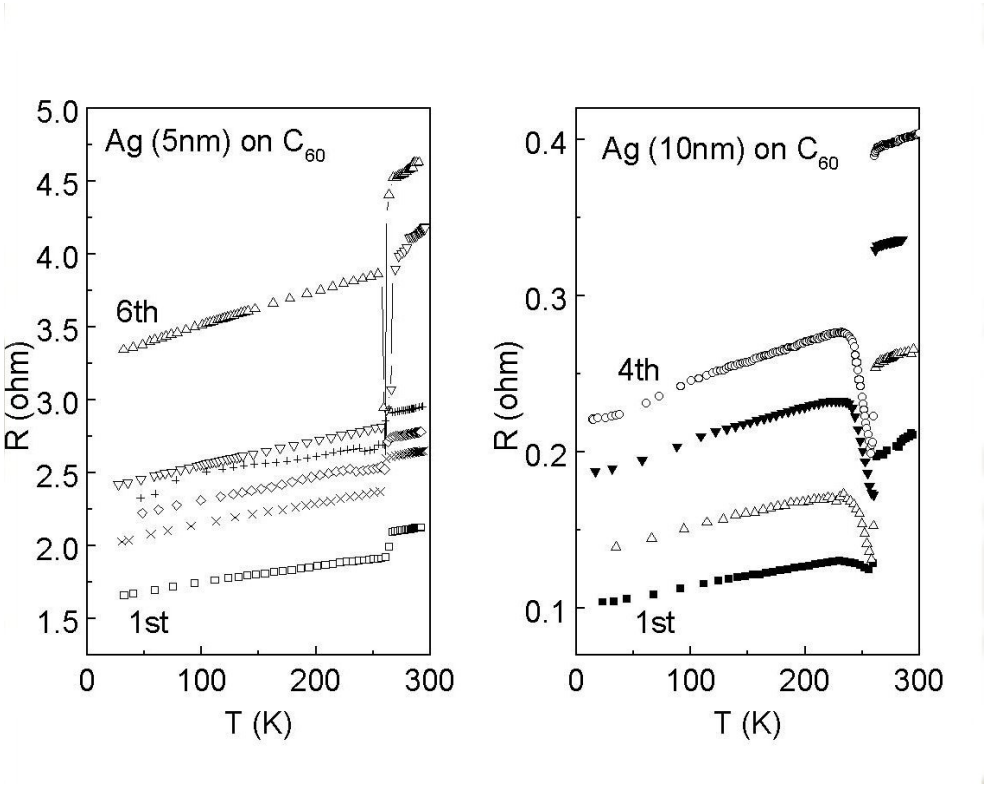

Figure 1-4 Resistance behavior of the 5nm (a) 10 nm (b) Ag film on C_{60} with thermal cycling. Only warming curves are shown for clarity.

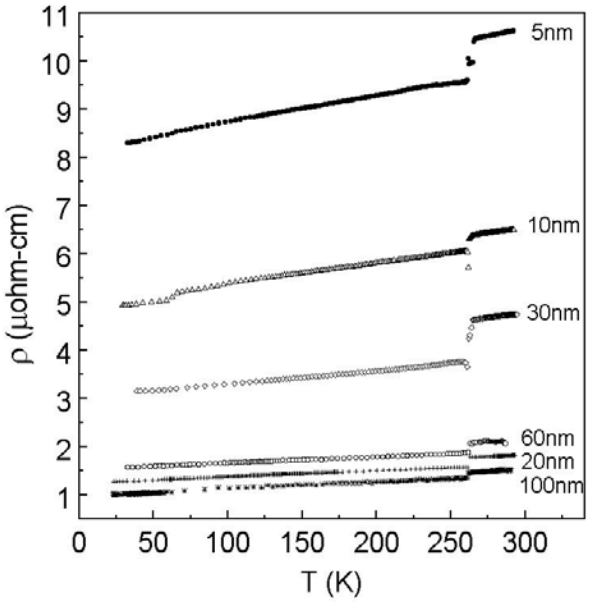

Figure 1-5 Resistivity vs. temperature of Ag films with different thicknesses on C_{60} crystals (first thermal cycle).

Figure 1-5 shows the effect on the resistivity of systematically varying the thickness (t) of the Ag films between 5nm and 100nm. All data sets in Fig. 1-4 are for different newly prepared samples, measured during their first thermal cycle (where the resistive anomalies are smallest). The three-dimensional resistivity ρ has been calculated using the measured resistance R, the in-plane film/contact geometry, and the nominal film thickness as determined by the sputtering system crystal monitor. No attempt has been made to correct for film granularity. With the exception of the 20nm sample (which was prepared with a higher deposition rate that likely produced a less granular film), the resistivities $\rho(T)$ generally increase with reduced thickness. However, the slope $d\rho/dT$ between 100K~240K also increases notably with reduced thickness, in apparent violation

of Matthiessen's rule. The thickest film has a room temperature resistivity of approximately 1.6μΩ-cm, consistent with that expected for a uniform silver film in the bulk limit.

Figure 1-6 shows the *R(T)* data from the first thermal cycle of four thin metal films on C_{60} crystals, where the metals are Pd (20 nm), Cu, Pt, and Au (all 10 nm). Although the *R(T)* curves differ markedly, the anomaly near 261K generally reproduces for each metal. For Pd and Pt films, the resistance dips are more evident than those of Au and Cu films. The Pt *R(T)* curve shows apparently semiconducting behavior, possibly due to disconnected granular structures with thermally activated conductivity. The overall results suggest that the anomalies are universal to different metallic films and a general mechanism must be considered for this metal-C_{60} interface effect.

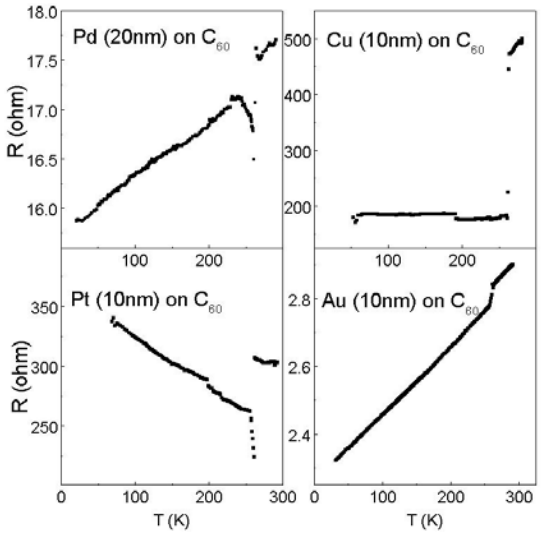

Figure 1-6 Resistance vs. temperature behavior for Au, Cu, Pd, and Pt films on C_{60} crystals.

1.4 Discussions

Crystalline C_{60} is a band insulator with room temperature resistivity in excess of 10^6 Ω-cm, while silver is a good electrical conductor with a resistivity of 1.6 μΩ-cm at room temperature. Due to this eleven order of magnitude difference, one would naively expect that the resistance measurement on the Ag-C_{60} system would only reflect the behavior of pure Ag. However, the observed anomalies clearly coincide with the structural phase transitions of crystalline C_{60}, as shown in Fig. 1-7. The slope change at 100K is near the quenched disorder phase transition, and the anomalies at 240K and 261K correspond to the surface and bulk rotational ordering transitions, respectively. The correlation between the resistance anomalies and the phase transitions suggests a strong coupling between the Ag film and the C_{60} crystal.

The clear relationship between the structural phase transitions of the C_{60} crystals and the resistivity anomalies in the metal films is the main result of this chapter. To explain this relationship, I propose a simple model where the thin metallic film acts as a resistive strain gauge, and thus is sensitive to the unusual phase structural phase transitions (including lattice discontinuities) of the substrate crystal. Although some features of the data are well accounted for by this model, others are not. The most serious failing of the model is an inability to account for, even qualitatively, the sharp resistance dip near 260K. To some extent this 'failing' highlights the most interesting feature of the data, for the unexplained resistance dip at C_{60}'s rotational ordering transition seems to indicate the presence of a truly novel interaction.

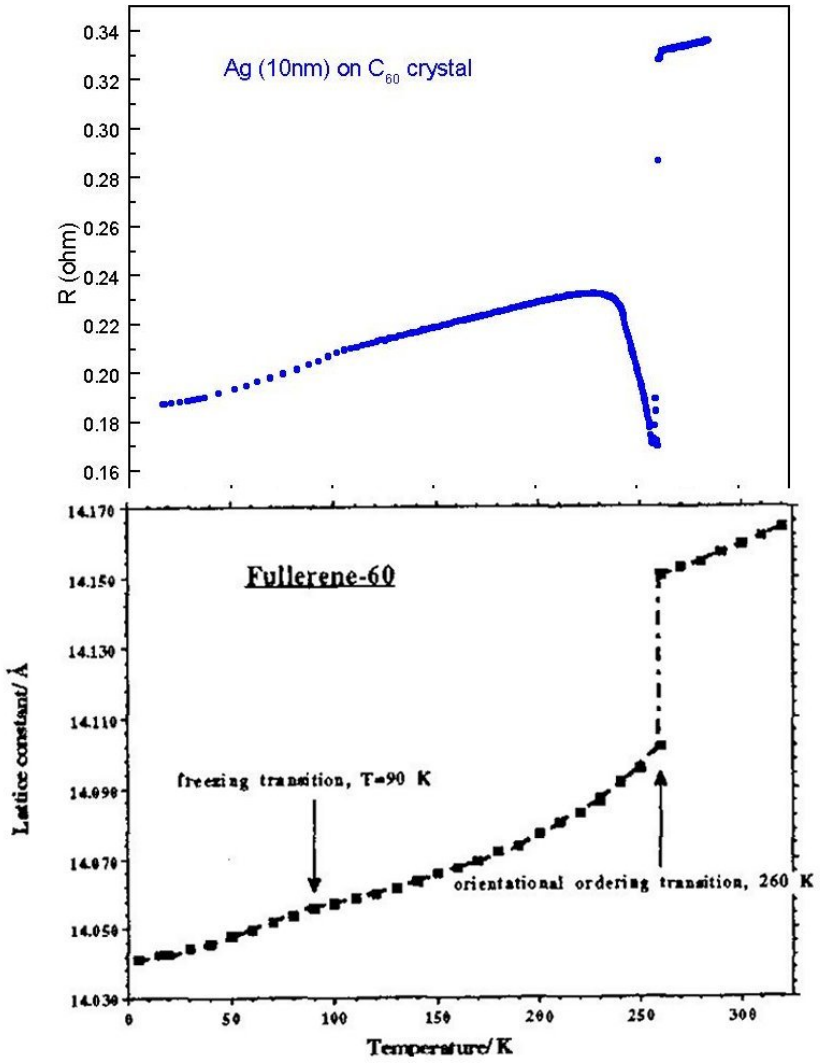

Figure 1-7 Comparison of the temperature dependent resistivity anomaly (top panel) and lattice constant (lower panel) of C_{60} crystals.

A key enabling feature of the strain gauge model is a differential thermal expansion $\Delta\alpha$ between the metallic overlayer and the substrate crystal. In the range 100-300K but away from the 261K transition the linear thermal expansion coefficients of Ag and $C_{60,}$ though comparable, are not matched: 1.9×10^{-5}/K vs. 2.1×10^{-5}/K, respectively. Below

100K α for Ag decreases with decreasing temperature while for C_{60} α is relatively temperature independent. At the rotational ordering transition the lattice parameter of C_{60} changes abruptly by more than 0.3%. Although the simplest geometric effect gives a contribution orders of magnitude too small to explain the observations, granularity could enhance the film's sensitivity to geometric changes. The network evident in Fig. 1-3(a) supports the granularity hypothesis. Thus, differential thermal expansion could be a factor in driving the $d\rho/dT$ anomalies that are observed over the entire measurement range and are especially dramatic at the lattice parameter discontinuity.

The strain gauge picture might also explain the results of the thermal cycling measurements. Fatigue created by mismatched thermal expansion coefficients is a problem well known in the semiconductor industry, and I observe qualitatively that repeated cycling often leads to macroscopic cracking of the sample. Viewing the film as a network of current paths in parallel, I hypothesize that thermal cycling creates microscopic fractures that break some paths. In the data of Fig. 1-4(b), for instance, the residual resistance ratio ($\equiv R(300\text{K})/R(T\rightarrow 0\text{K})$) is a constant ~ 2 for the four curves. The assumption that thermal cycling cuts some current paths explains this observation (the resistance increases without changing the residual resistance ratio), for eliminating resistors from a parallel network would produce exactly this behavior. If, on the contrary, thermal cycling were introducing defects, the residual resistance ratio would be expected to decrease while the resistance increased.

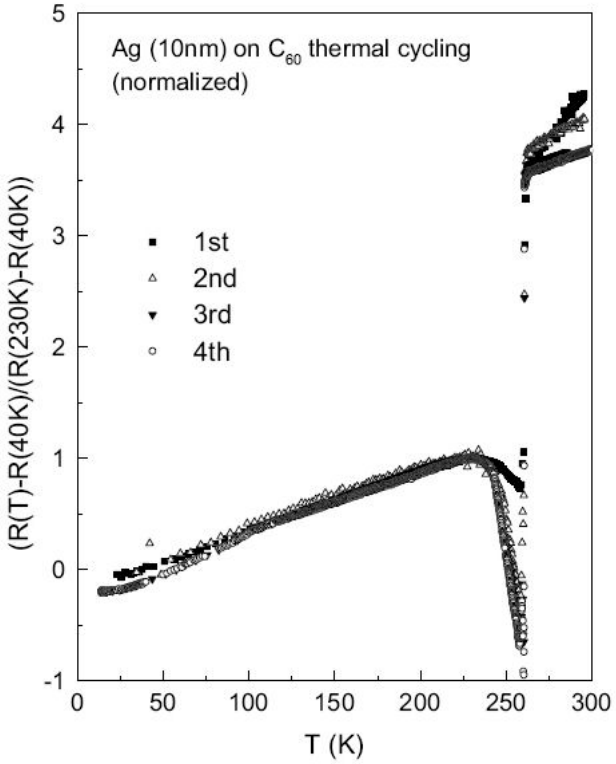

Figure 1-8 The data of Fig. 2(a) rescaled according to the strain gauge model.

Figure 1-8 shows the data from Fig. 1-4(b) rescaled according to this hypothesis. Between the normalization points of 40K and 230K the four curves overlap well, which confirms only that the data are reasonably linear in this temperature region. However, even above the 260K discontinuity the same approximate scaling continues to hold. This result implies that the relative magnitude of the discontinuity is an intrinsic property of the film: the resistivity of the silver film reflects changes in the lattice parameter of the substrate crystal. (By hypothesis this resistivity cannot be calculated from the measured resistance, since the microscopic cracks caused by thermal cycling create substantial geometric uncertainty.) The slow climb of the resistance from 20K to 230K, and the

jump from 230K to 260K, both reflect the corresponding thermal expansion of the substrate crystal.

Although the strain gauge picture provides a useful view of the observations, the model is incomplete and probably overlooks interesting physics. The mechanism by which the resistive sensitivity of the film is amplified is not established. While SEM characterization implicates film granularity, this feature alone does not guarantee amplification. Indeed, with the exception of the platinum curve, the data presented show positive dR/dT at low temperature, demonstrating that the continuous limit (insulating islands in a conducting matrix) is appropriate here. In this limit, away from the percolation threshold, extraordinary sensitivity to differential thermal expansion is not expected.

However, the biggest failing of the strain gauge model comes in the temperature range 240-260K, which this discussion has until now ignored. The lattice constant of C_{60} is thought to be a monotonically increasing function of temperature, which makes it difficult for this mechanism to explain the region of negative dR/dT seen in the range 240-260K. The appearance at 261K of a resistance lower than the residual resistance, also unanticipated by this simple model, is even more striking. As illustrated by Fig. 1-4, the dip resistance remains relatively constant with thermal cycling, as compared with the resistance away from the rotational ordering transition. The trivial explanation of macroscopic, temperature-dependent, nested currents has been tested with auxiliary measurements featuring rapid switching through different current/voltage four-probe

configurations, and no evidence for such spurious effects is seen. Thus, at the rotational ordering transition a new interaction seems to dominate the conductance of the film.

A more complete understanding of these resistive anomalies, particularly the 261K dip, might reveal interesting phenomena. Exotic superconductivity has been apparently excluded, as I have found that these anomalies are independent of magnetic field up to 4.6 kG. I have also searched for evidence of critical exponents near the rotational ordering transition, but the available data are inadequate for such analysis. Charge transfer between various metallic films and C_{60} crystals has been widely reported [11,12], and two groups have reported anomalous conductance enhancements at room temperature in layered structures of metal films and C_{60} [11,13,14]. They suggest that charge transfer creates an additional conduction band in the interfacial monolayer of C_{60}. Structural transitions of the C_{60} crystal might perturb this two-dimensional channel, creating the resistance anomalies reported here. It is also possible that the 261K anomaly is related to a proposed intermediate phase that occurs in narrow temperature range around 261K [15], or an unusual electron-phonon scattering effect. Interestingly, conductance peaks have been observed at phase transitions in other exotic materials [9].

On a more speculative note, there is an analogy between the rotational transition of C_{60} crystal and the ferromagnetic transition of magnetic materials. The isotropic rotation of each C_{60} above 261K corresponds to a paramagnetic state, and the constrained spinning below 261K is analogous to a ferromagnetic state with anisotropic axes. These correspondences can be seen in the heat capacity of C_{60} crystals and magnetic materials (for example, Ni) near their transition temperatures [16]. Both show a sharp lambda-

shape anomaly [17]. The divergent behavior of the heat capacity suggests that many degrees of freedom are involved for excitation, thus fluctuation effects should dominate near the phase transition temperature. Regarding the resistivity behavior for magnetic materials, some theoretical works find that fluctuations lead to divergence in resistivity or $d\rho/dT$ at Curie temperature [18,19]. However, the results show divergent behavior in conductivity near 261K. The qualitative discrepancy could indicate a more profound origin which is beyond the scope of this chapter.

In summary, I have measured the $\rho(T)$ behavior of different metal films on C_{60} crystals as a function of thermal cycling and film thicknesses. I find features that correlate with structural phase transitions of C_{60} crystals, thus demonstrating that metallic films can be sensitive probes of the underlying phase transitions of C_{60} crystals. Finally, I observe a dramatic resistivity dip near the rotational ordering transition of C_{60}, which is unexplained by the simple model and may be evidence for a novel interaction.

Chapter 2 Introduction to carbon and boron-nitride nanotubes

2.1 History of carbon nanotubes

In 1990, when Sumio Iijima was studying the C_{60} generated by the arc discharge method under high resolution TEM in NEC's research laboratory, he found a needle-shaped material [20]. This needle-shaped material is the material to which was later given the name "carbon nanotube" (CNT). In the original paper of 1991, only multiwalled carbon nanotubes (MWCNTs) were observed. Later, when people tried to encapsulate Fe particles into carbon nanotubes, they discovered that Fe particles can act as catalysts to make singlewalled carbon nanotubes (SWCNTs). In 1993, Ijima and Ichihashi at NEC and Bethune *et al*. at IBM independently reported the preparation of SWCNTs [21,22]. The structure of CNTs was soon recognized as a graphene sheet rolled up into a tubular structure that has a diameter of nanometer scales.

2.2 Electronic properties

R. Saito *et al.* showed that the rolling vector dictates the electronic band structure of SWCNTs [23]. As shown in Fig 2-1, the rolling vector can be decomposed into a

summation of two lattice vectors $\mathbf{a_1}$,$\mathbf{a_2}$, thus $\mathbf{C} = n\mathbf{a_1}+m\mathbf{a_2}$, where (n,m) are integers. Depending on (n,m), the structure of the SWCNTs can be armchair (n=m), zigzag (n or m=0), or chiral. It is shown that when n-m = 3i (i = integer), the SWCNTs are metallic. Otherwise, they are semiconducting with the band gap varying from 1.5eV to 0.3eV for diameters 0.6nm to 3nm.

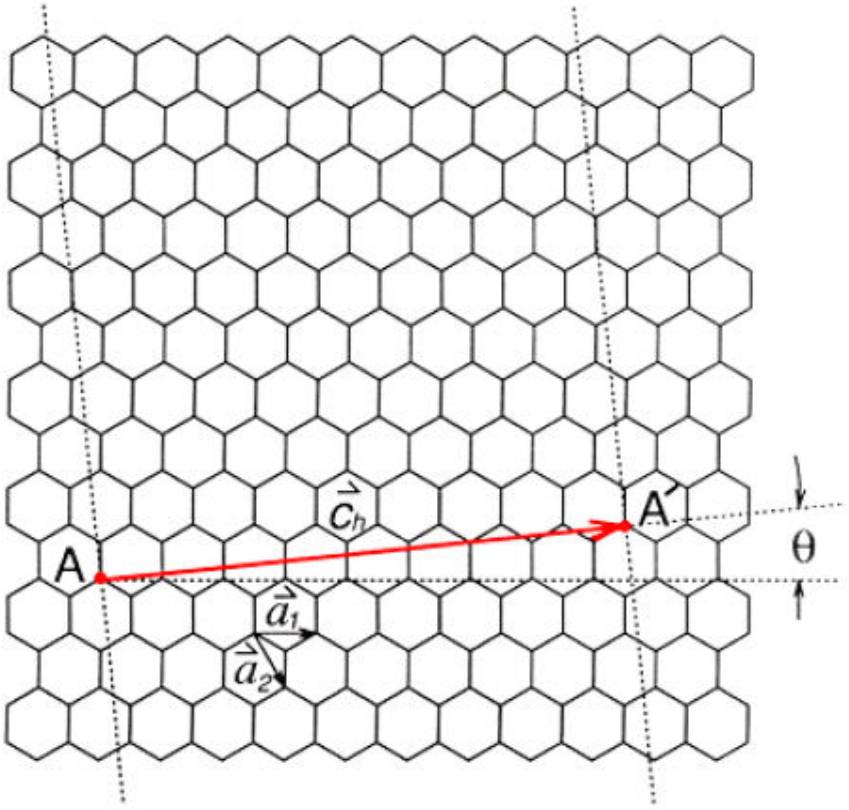

Figure 2-1 CNT rolling vector can be decomposed into a summation of two lattice vector, or a index (n,m). In this figure, we have a (9,1) CNT.

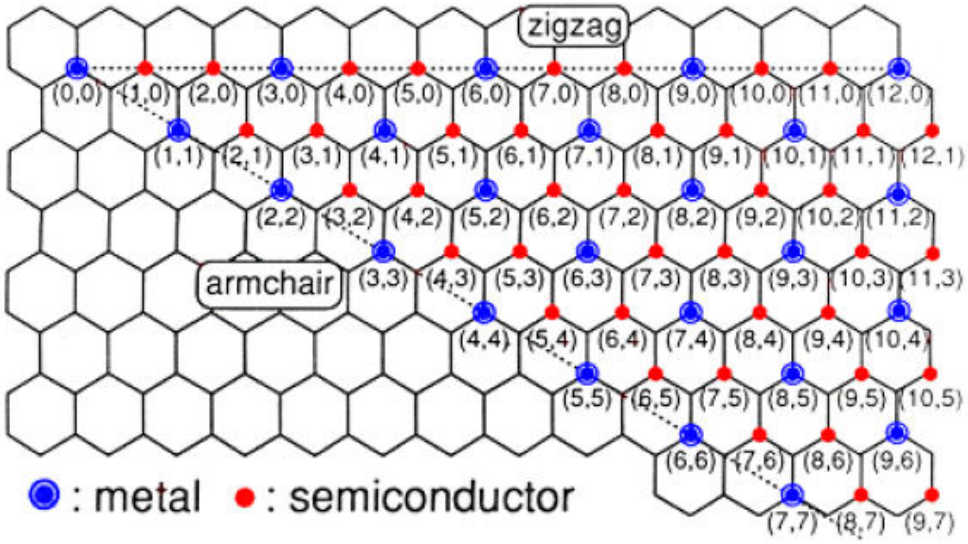

Figure 2-2 The (n,m) index dictates the electronic structure of a CNT.

Tight-binding calculations on the electronic behavior of MWCNTs suggest that if a MWCNT has a metallic shell, then that particular shell can retain its metallic character. Similarly, a combination of nonmetallic CNTs is not expected to become metallic as a result of the interlayer interactions [24].

Experimentally, researchers have shown that CNTs exhibit high electron mobility [25], high current capacity [26], and induced superconductivity [27]. Furthermore, CNTs have been integrated in electronic circuits [28]. These extraordinary features make CNTs very attractive elements for applications.

2.3 Mechanical properties

Due to the strong sp^2 bonding, the mechanical properties of CNTs are also unique. Theoretical and experimental work has shown that the elastic modulus of carbon

nanotubes exceed 1TPa, which is higher than any other material known so far [29,30]. Their measured tensile strength is 63GPa [31], much higher than that of steels (~0.4GPa). The high elastic modulus and low density make CNTs potential high frequency nanomechanical oscillators. The McEuen's group made a nanomechanical resonator based on CNTs [32]. Haibing Peng *et al*. also demonstrated utilizing CNTs as high frequency giga-hertz resonators [33].

On the other hand, the van der Waals force between walls of MWCNTs is extremely weak. Thus it had been proposed to use MWCNTs as nanomechanical devices with ultra-low friction forces. John Cumings demonstrated using MWCNTs as linear bearings and determined the friction force to be less than 10^{-14} N per atom [34]. The result was further investigated by Andras Kis *et al*. who performed cyclic telescoping measurements using an atomic force microscope (AFM) cantilever mounted inside a TEM [35]. Adam Fennimore *et al.* showed it is possible to make rotational actuators based on MWCNTs [36]. Theoretical calculations have suggested using these telescoping properties to build giga-hertz linear oscillators [37].

It is worthy to note that continuum mechanics still applies for the nano-structured materials. It indicates that the common scaling law we encounter in macroscopic objects can still be used for predicting the mechanical properties of nanotubes.

2.4 Thermal properties

An excellent review of the thermal properties of CNTs can be found in James Hone's review article [38]. I will briefly summarize the main results here.

For a single graphene sheet, the lowest lying three phonon modes are two longitudinal acoustic (LA) modes, and one in-plane transverse acoustic (TA) mode. After rolling a graphene sheet into a SWCNT, there are four, rather than three, acoustic modes: one LA mode, two TA modes, and a 'twist' mode. The LA mode is analogous to the LA mode in graphene. The two TA modes correspond to a combination of the in-plane and out-of-plane TA modes in graphene. The twist mode is analogous to the in-plane TA mode. These modes all show linear dispersion and high phonon velocities: v_{LA}=24km/s, v_{TA}=9km/s, and v_{twist}=15km/s for a (10,10) CNT [39].

The reduction of dimensionality in nanotubes results in several pronounced peaks of the phonon density of states, known as van Hove singularities. The splitting between the subbands of phonon modes is of order

$$\Delta E = k\theta_B \sim \frac{\hbar v}{R} \tag{2.1}$$

where R is the radius of the nanotube. The splitting is estimated to be on the order of 100K for a 1.4nm-diameter SWCNT. For a (10,10) tube, it is estimated that the lowest subband enters at ~2.5meV (30K). In the low temperature regime, the thermal properties are dominated by the acoustic modes, giving a linear temperature dependence for the specific heat:

$$C_{ph} = \frac{\pi k_B^2 T}{\hbar v \rho_m} \tag{2.2}$$

where ρ_m is the mass per unit length. One can also evaluate the electronic contribution to the total specific heat. It is estimated that the electronic contribution is less than 1% down to T=0.

The heat capacity of mats of SWCNTs and MWCNTs has been measured by several groups. Experimental deviations from the calculated specific heat of graphene and graphite have been observed in the low temperature measurements of mats of SWCNTs and MWCNTs [40,41]. The deviations were interpreted as the signatures of one-dimensionality of CNTs. However, since the inter-tube couplings, the inter-wall interactions, and the sample morphologies are unknown, the analysis based on simple models should not be taken too seriously.

Another interesting thermal property of CNTs is the thermal conductivity behavior. I will discuss various theoretical and experimental aspects of the thermal conductivity of CNTs in later chapters.

2.5 Overview of carbon nanotube synthesis

CNTs can be synthesized by various methods. Many of them have been conducted in the Zettl group. I will briefly summarize the results of various methods. A very good discussion of CNT synthesis can be found in [42,43].

Arc discharge

Arc discharge method can make very good quality CNTs. Both SWCNTs and MWCNTs can be synthesized by this method. The arc-discharge chamber is filled with

some inert gas (He or N_2). Then a high current is passed through the graphite electrodes. A plasma is created, reaching a temperature higher than 10000°C, and a carbon 'boule' forms on the cathode. CNTs can be found inside the 'boule'. TEM imaging shows that these CNTs are highly crystalline with length 2~10μm, diameter 5~30nm. Willi Mickelson also made isotopically pure CNTs by this method. However, the arc-discharge method also produces many by-products, which becomes its major disadvantage. This makes the filtering and purification process difficult. Besides, it is difficult to control the plasma conditions while arcing, thus reproducibility is another problem.

Laser ablation

Laser ablation method utilizes high-power laser pulses that cause localized spots on the graphite target to reach very high temperatures whereby they evaporate and react with each other in the region near the graphite target. Then CNTs are carried by some inert gas and collected at a cold finger downstream. CNTs synthesized by laser ablation have the same advantages and drawbacks as the arc-discharge method.

Chemical vapor deposition

Chemical vapor deposition (CVD) methods so far have made the longest CNTs. CVD methods often involve catalysts, thus it is possible to control the location of CNT growth. With correct choice of reaction gas, temperature, and flow rate, one can grow CNTs with lengths exceeding centimeters. Various interesting structures, such as CNT "forests" and "bridges" have been demonstrated by employing this method. However, the CNTs synthesized by this method are of poorer quality than those made by arc-

discharge or laser-ablation. Although it is possible to synthesize very long CNTs by this method, they are not always straight, and many of them exhibit defects. Removing the unwanted catalyst particles is another challenge.

Although there are various difficulties in synthesizing good quality CNTs by CVD methods, these methods seem to be the most promising technique. Kenny Jenson *et al.* observed in-situ re-growing of a CNT by reacting with Fe catalysts encapsulated inside a MWCNT [44]. Their in-situ TEM images demonstrated that it is possible to re-grow a highly crystalline CNT with catalysis reaction. Thus if the reaction gas and the flow rate are controlled very well, it is possible to use CVD method to grow good quality CNTs.

2.6 Boron-nitride nanotubes

After CNTs were discovered, people started looking for layered materials that may also form cylindrical structures. Hexagonal boron-nitride (BN) is similar to graphite. Not only the sp^2 bonding nature is similar to that of graphite, but also many physical properties are comparable to that of graphite. Theoretically, it was first suggested that the hexagonal BN sheet can also form a stable cylindrical structure [45].

Carbon-containing nanotubes with stoichiometry of BC_2N and BC_3 were reported by Z. Weng-Sieh *et al.* [46] and O. Stephan *et al.* [47]. In 1995, Nasreen Chopra and co-workers in the Zettl group used a carbon-free arc discharge method to synthesize pure boron-nitride nanotubes (BNNTs) [9]. The structure of a BNNT can be viewed as rolling up a hexagonal sheet into a cylindrical structure like that of CNTs. Later it was demonstrated that BNNTs can be single-walled, double-walled, or multi-walled [48,49].

2.7 Electronic and mechanical properties

Due to the ionic nature of the B-N bond, hexagonal BN has a 5.8eV band gap. Theoretical work suggests the band gap of BNNTs to be 4~5.5eV. This band gap is almost independent of chirality, nanotube diameter, or number of walls [50]. Masa Ishigami measured a gap of ~3.8eV from a single BNNT using a scanning tunneling microscope (STM) [51]. Shaul Aloni in the Zettl group and R. Arenal *et al.* used EELS to determine the band gap of a single BNNT to be 5.8eV [52].

BNNTs are predicted to exhibit mechanical properties similar to those of CNTs. Theoretical calculations suggest that the Young's modulus of BNNTs is 0.7 times that of CNTs [53]. Nasreen Chopra *et al.* measured the elastic modulus of BNNTs to be 1.2TPa [54].

Hexagonal BN has thermal properties comparable to that of graphite [55-57]. Theoretical calculation suggests that hexagonal BN has a phonon dispersion relation similar to that of a graphene sheet [58]. Thus it has been suggested that BNNTs would have thermal conductivity comparable to that of CNTs [59]. However, these calculations do not consider the large isotope impurities found in the natural abundance boron. The details of thermal transports of BNNTs will be discussed in later chapters.

2.8 Overview of boron-nitride nanotube synthesis

Like CNTs, BNNTs can be synthesized by various methods. The Zettl group has a long history of synthesizing BNNTs. Detailed synthesis methods can be found in the theses of former Zettl group members. I will only briefly describe them in the following.

Arc discharge

Although the first successful synthesis of BNNTs was done by arc-discharge method, it suffered from its low yield in the beginning. John Cumings later improved the method by mixing boron with conducting catalysts, such as nickel or cobalt. Thus large quantity production of BNNTs became possible. However, like the drawbacks in making CNTs by the arc-discharge method, many unwanted by-products also exist. So additional purification processes are needed. For BNNTs, these processes are even more elaborate than those of CNTs. Because boron oxides, unlike carbon oxides, are solids and do not go away after burning in air. John Cumings and Kevin Jones had tried to use a chromatography method to purify them but the results were not always successful.

Substitution reaction CVD

A CVD-substitution method developed by Weiqiang Han uses MWCNTs as templates, B_2O_3 as starting materials, and NH_3 or N_2 as reaction gases. The proposed reaction is as follows [60]:

$$B_2O_3 + 3C(\text{nanotubes}) + N_2 \rightarrow 2BN(\text{nanotubes}) + 3CO$$

The resultant materials are B-C-N nanotubes. The B-C-N nanotubes can later be converted to pure BNNTs by oxidizing them in air at ~650°C. Depending on the synthesis conditions, the yield of the BNNTs varies. The B-C-N and BN nanotube mats made by this method were used for the thermal conductivity measurements described in chapter 5. Unlike the CVD method for making CNTs, the CVD-made BNNTs are usually highly crystalline. However, BNNTs made by Weiqiang Han using the substitutional method are generally shorter than 3μm.

Magnesium oxide and boron oxide CVD

Tang *et al.* reported using B and MgO and heating them to 1300°C using an induction furnace [61]. Then they introduced ammonia gas to produce BNNTs. David Okawa and co-workers have systematically investigated this approach and optimized the quality and the yield of BNNTs made by this method. For this method, a mixture of ball milled B and MgO (1:1 molar ratio) was placed in an alumina boat with a silicon substrate laying face down on top of the boat. The reaction vessel was placed in the hot zone of the furnace and heated to 1200°C under N_2. The gas was switched to ammonia and held at temperature for fifteen minutes before switching back to N_2 and cooling to room temperature. David Okawa also made various isotopically pure BNNTs using the ^{11}B(99.56% pure) source material obtained from Cambridge Isotope Inc. The BNNTs made by this method are highly crystalline with diameters 10~50nm. Most importantly, their length exceeds 5μm, which greatly facilitates the thermal transport measurements of individual BNNTs.

Chapter 3 Chemical functionalization of boron-nitride nanotubes

3.1 Potassium and lithium doping of boron-nitride nanotubes

As described in chapter 2, the band gaps of CNTs depend on the chirality, diameter, and number of walls. Although these properties make carbon nanotubes attractive, in practice they become the greatest obstacle for utilizing CNTs as electronic elements. Since so far no one can control the diameters or the chiralities of CNTs, it is difficult to utilize them as reliable electronic devices.

On the other hand, theoretical works have suggested that the band gaps of BNNTs are not sensitive to the diameter, chirality, or number of walls [45,50]. Furthermore, theories also suggest that the lowest conduction band of a BNNT exhibits a free-electron-like dispersion relation [50]. Thus if BNNTs can be doped into conducting, their electronic properties would be uniform and interesting.

For traditional semiconductors like Si, Ge, or GaAs, doping requires replacing host atoms with alien dopants. Although dopants introduce electrons or holes, they also create impurities in the lattice. In general, increasing the doping concentration in traditional semiconductors can reduce their electronic mobility significantly. For cylindrical-

structured nanotubes, ideally, dopants can go into the hollow space of a nanotube and transfer charges. Therefore, unlike traditional doping, the dopants neither replace the host atoms of the nanotube nor create lattice defects. Furthermore, the hollow space of the nanotubes has large capacity to host the dopants. In principle, the doping concentration can be varied by a larger scale without reducing the mobility. All these advantages make doping in nanotubes a very interesting subject.

Alkaline elements like potassium and lithium tend to lose electrons easily. So they are good electron donors. Many researchers have studied alkaline doping on CNTs. For example, R. S. Lee *et al.* observed that potassium-doped CNT mats had lower resistance than the pristine CNTs' and their *R(T)* behavior changed [62]. M. Bockrath *et al.* measured electrical transports on individual potassium-doped CNTs and observed a reduction of the band gap [63]. Here I tried to use potassium and lithium to dope BNNT mats.

BNNTs were made by Weiqiang Han using the substitution process described in chapter 2. The as-synthesized B-C-N nanotubes were converted into BNNTs by oxidizing them at 600°C. The resulting BNNTs are shown in Fig. 3-1. The BNNTs generally have length 2~3μm, which is comparable to the distance of the inter-digitated electrode shown in Fig. 3-2. To allow the potassium or lithium to go into the hollow space of BNNTs, the end caps of the BNNTs should be opened. Weiqiang Han has discovered that the above oxidation process also opens the caps of BNNTs [64]. In Fig. 3-1, it can be seen that the end caps of BNNTs are opened after the oxidation treatment.

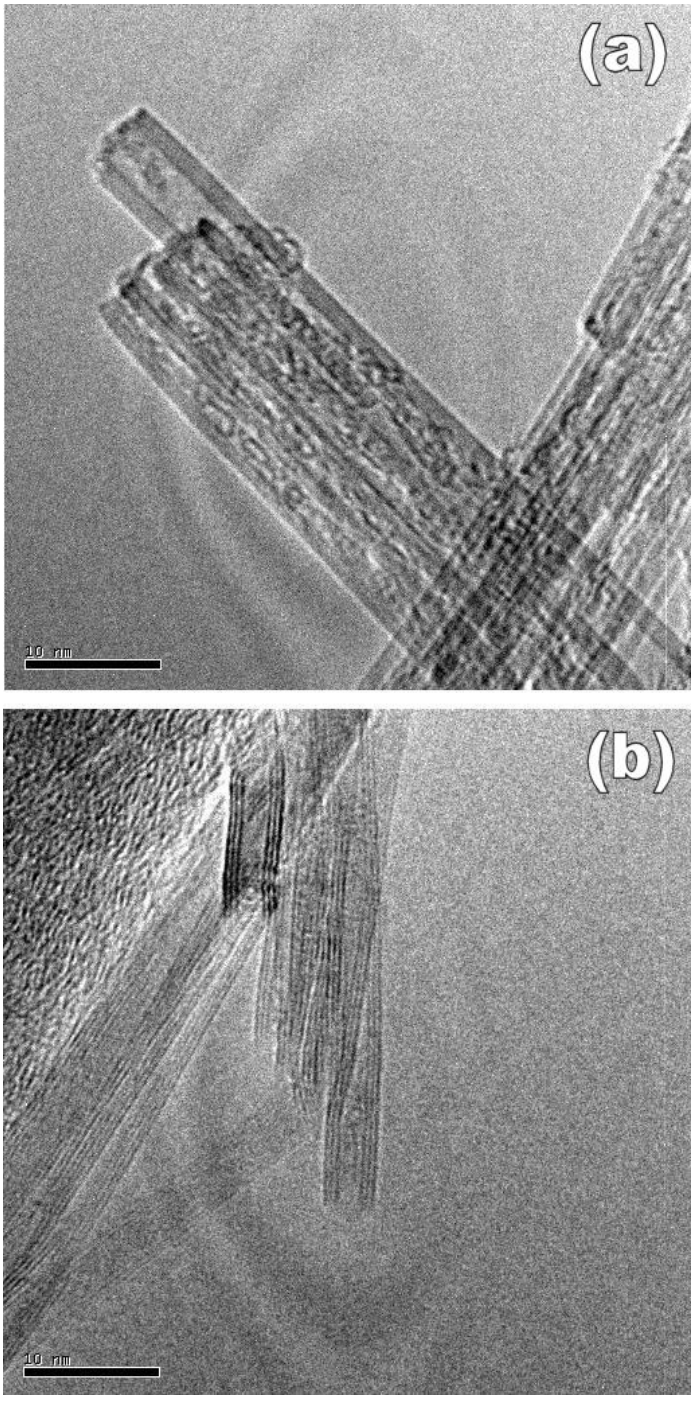

Figure 3-1 TEM images of BNNTs after the oxidation treatments (scale bar =10nm).

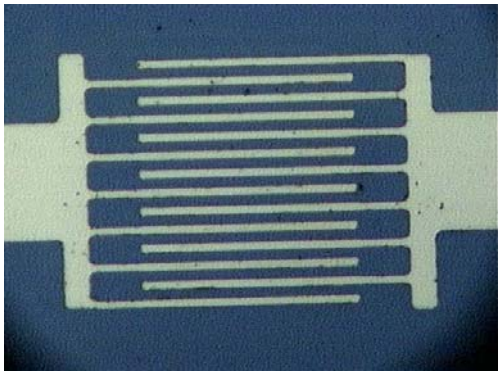

Figure 3-2 An inter-digitaled electrodes used for measuring resistance of BNNT mats. The distance between the electrodes is 2μm.

For potassium and lithium doping, I adapted the method that former group member Michael Fuhrer used for intercalating C_{60} with alkali metals [65]. The BNNT mats were dispersed on top of an inter-digitaled electrode shown in Fig. 3-2. Then the specimen was mounted on the doping vessel with two wires connecting to it. A pair of T-type thermocouple were used for monitoring the temperature. A tantalum boat was inserted into the doping vessel to carry the potassium or lithium as will be described later. The whole setup was transferred into the glove box. For potassium, I heated it up in the glove box and then used a syringe to transfer the molten potassium into the tantalum boat. For lithium, since it oxidizes slower than does potassium, I took a piece of lithium from the storage oil then quickly transferred it into the glove box. Inside the glove box, the surface of the lithium was scratched so that the shining, un-oxidized surface was exposed. Then the lithium piece was transferred to the tantalum boat. After inserting the tantalum boat, the other end of the doping vessel was connected to a closed vacuum valve. So the whole setup was sealed with Ar. When taking the doping vessel out of the glove box, it was quickly connected to a turbo-pump system and then pumped down the pressure

below 10^{-5} torr. A hydrogen-oxygen torch was used for gradually pinching down and finally sealed the doping vessel while maintaining the vacuum. In the mean time, the tantalum boat was carefully moved away from the torch so that the potassium or lithium would not evaporate. Once the doping vessel was sealed, the potassium or lithium remained its shining color for many days. To dope potassium or lithium into the BNNTs, the doping vessel was wrapped by a heating tape and heated to the desired temperature. A Keithley 182 voltage meter (input impedance > 10GΩ) and a Keithley 224 current source were used for measuring the sample resistance. Another Keithley 182 voltage meter was used for measuring the thermocouple voltage.

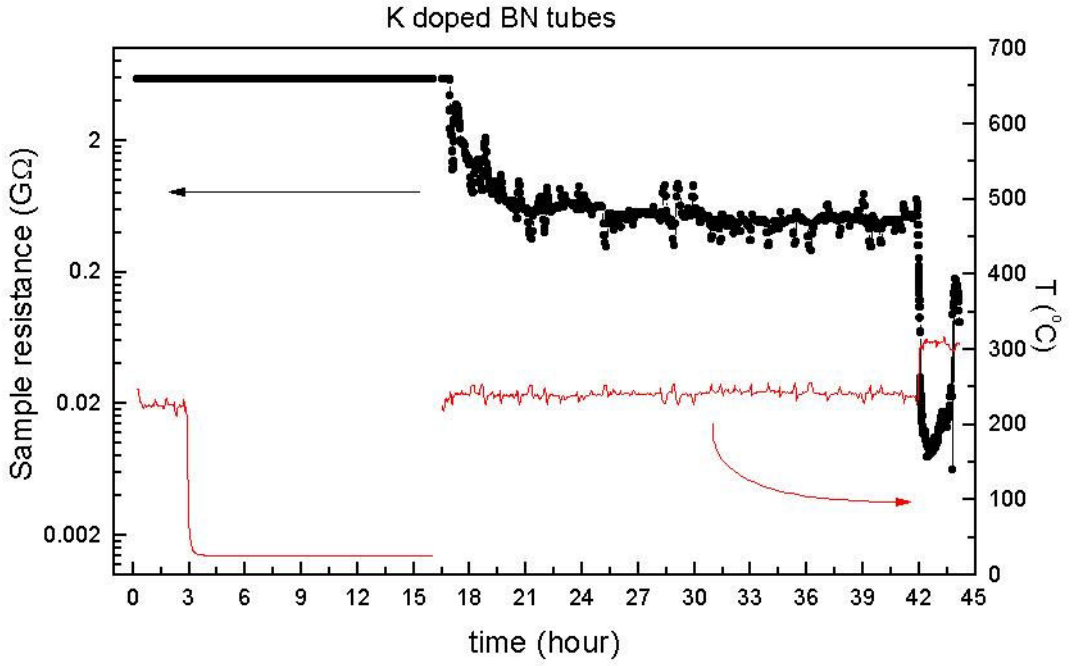

Figure 3-3 Resistance vs postassium doping time of a BNNT mat sample 1.

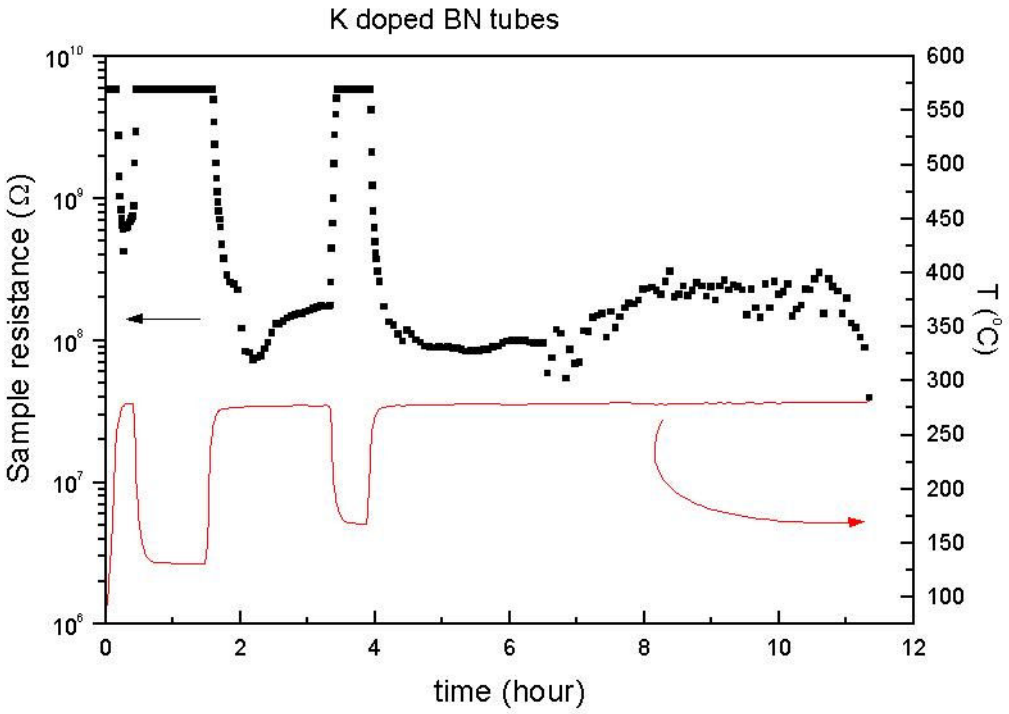

Figure 3-4 Resistance vs. potassium doping time of a BNNT mat sample2.

Figure 3-3 shows the resistance vs. potassium doping time on a BNNT mat sample. Initially, the sample resistance is more than 10GΩ. After raising the temperature of the doping vessel, the sample resistance decreases for more than two orders of magnitudes. However, the sample resistance remains high and increases as the temperature decreases. Figure 3-4 shows the result of potassium doping on another BNNT mat sample, the sample resistance gradually increases even as the temperature is kept constant. It might be due to some leaks in the doping vessel so that the potassium oxidizes gradually.

Since the vapor pressure of lithium is lower than that of potassium, a higher temperature is required to evaporate lithium. Thus a quartz, instead of a glass doping

vessel was used for the experiment. However, a higher temperature made the insulation of the wires unreliable. To improve the insulation of the wires, a thin layer of hexagonal BN was sprayed on the wires before twisting them. A control experiment was done to ensure that the high temperature would not give erroneous results. Generally, for temperatures lower than 400°C, the insulating of the coating did not cause problems. Figure 3-5 shows the sample resistance vs. lithium doping time. Except for the drop of the resistance at the beginning, the resistance of the lithium-doped sample generally increased faster than that of the potassium-doped samples. In some cases, I found the quartz tube broke at high temperatures. The resistance instability of the lithium-doped BNNTs might be due to the seal of the doping vessel becoming leaky at high temperatures so that the sample oxidized.

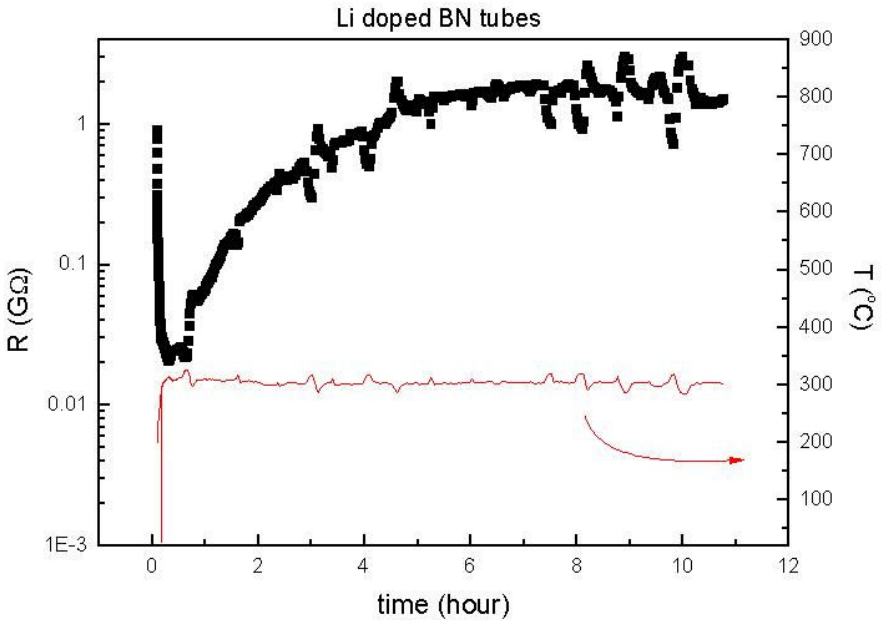

Figure 3-5 Resistance vs. lithium doping time of a BNNT mat.

It is interesting to ask whether it is possible to introduce holes into BNNTs. Halide elements have high electron affinities, thus they are good hole-dopants. Among various halide elements, iodine has the lowest electron affinity, but it is easier to handle and less toxic. So iodine is chosen to dope BNNTs. The experimental procedure is similar to the one used for potassium or lithium doping. Figure 3-6 shows the results of iodine doping on BNNTs. In contrast to the results of potassium or lithium doping, the iodine-doped BNNTs do not show any resistance change. The result indicates that a stronger electron-affinity element must be chosen to dope holes into BNNTs. In fact, recent experiments on fluorine-doped BNNTs showed appreciable resistance decreases [66], suggesting that holes can be doped into BNNTs and modify their electronic structures.

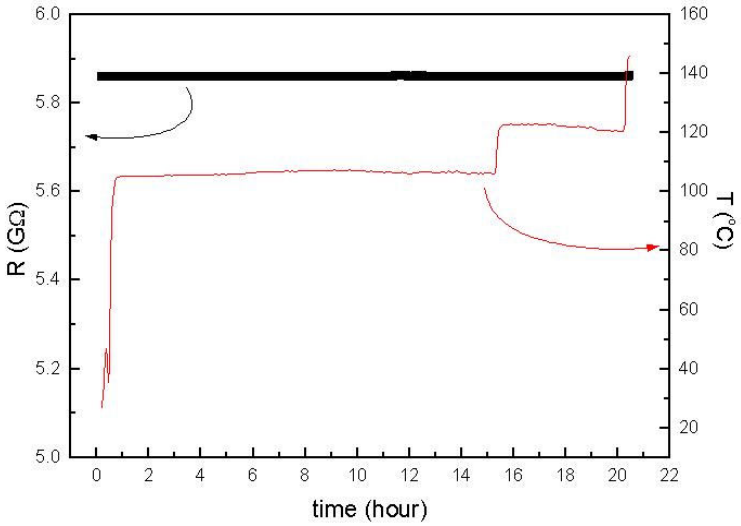

Figure 3-6 Resistance vs. iodine doping time of a BNNT mat sample.

Figure 3-7 shows R(T) of various potassium-doped and lithium-doped BNNT mats. Generally, the resistance increases as the temperature decreases, suggesting that these alkaline-doped BNNTs are semiconductor-like. I-V curves of some potassium-doped and lithium-doped BNNT mats are also measured. As shown in Fig. 3-8, the I-V curve shows non-linear behavior at room temperature. The origin of the non-linearity could be due to the intrinsic semiconductor behavior of the alkaline-doped BNNTs, or due to junction barriers between nanotubes so that they cost electrons' energy to hop from one BNNT to another. However, due to the complex sample geometry and the large sample resistance, further characterization is difficult using present results.

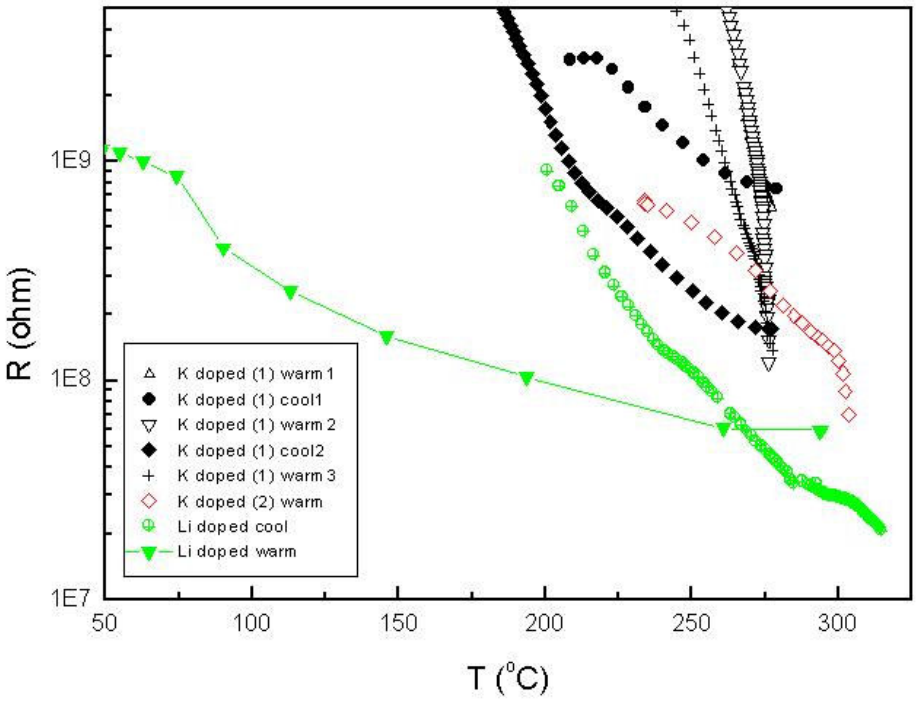

Figure 3-7 Temperature dependent resistance curve of various alkaline-doped BNNT mats.

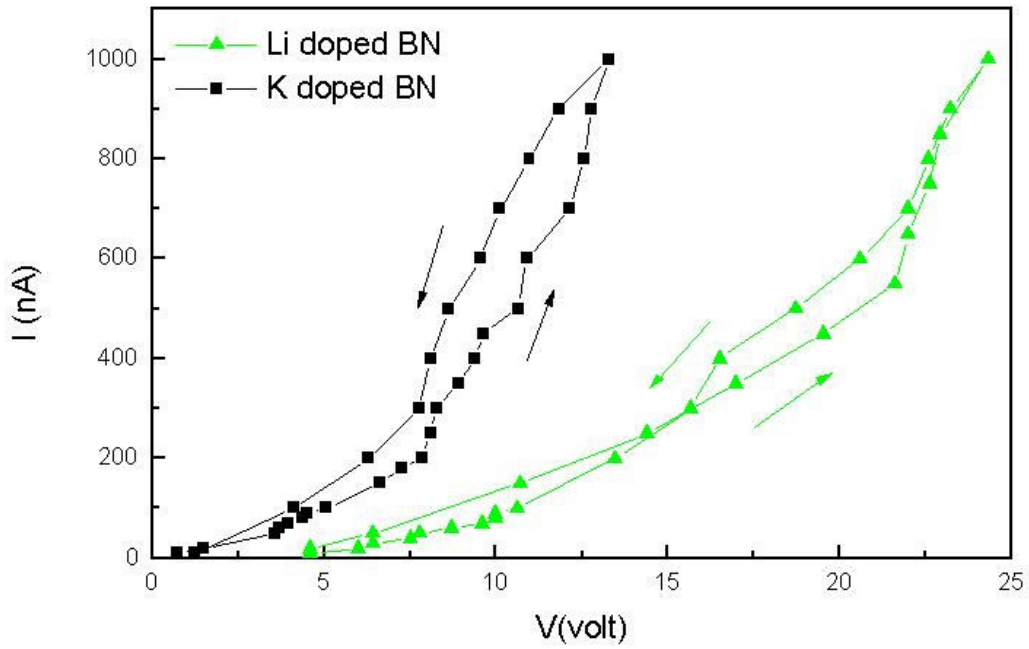

Figure 3-8 Room temperature I-V curves of a lithium (triangle) and a potassium (square) doped BNNT mat samples.

In conclusion, the resistance of potassium-doped and the lithium-doped BNNTs decreases for more than two orders of magnitudes. In contrast, the resistance of the iodine-doped BNNTs does not display any change. The results demonstrate that it is possible to modify the electronic structure of BNNTs by alkaline-doping.

3.2 Encapsulation of potassium halide crystals within boron-nitride nanotubes

Encapsulating of alien materials into nanotubes is of great interest due to its potential of modifying the intrinsic properties of nanotubes. On the other hand, due to the confined space of the nanotube, the encapsulated materials may arrange themselves into exotic lattice structures that do not exist in ordinary bulk samples. The modified structure may further change the electronic, mechanical or thermal properties of the encapsulated materials. Among all chemical bonds, the van der Waals interaction is the weakest. Thus it is easy to perturb the lattice structure of a van der Waals solid, such as a C_{60} crystal. For example, Willi Mickelson *et al.* have filled C_{60} into BNNTs and observed various types of novel structures [67]. On the other hand, ionic bonds are normally three orders of magnitudes stronger than the van der Waals interaction. Thus it is interesting to see whether the confinement effect can affect the lattice structure of ionic crystals. Alkaline-halides compounds are the simplest ionic crystals and all of them have NaCl structures. The monotonic increasing of the binding energy with respect to decreasing anion size makes them of fundamental interest for filling into BNNTs.

This work was done in collaboration with Weiqiang Han [68]. The BNNTs made by the substitutional process were sealed in different evacuated ampules together with different commercially available potassium halides in about 4:1 halide/BNNT mass ratio. The ampules were put into a furnace with temperatures from 670°C to 740°C for four hours. Then the ampules were broken open, and the resultant materials were

ultrasonically dispersed in methanol and dropped onto a holey carbon coated grid for TEM characterization. The TEM images were taken by Weiqiang Han using Philips CM200 FEG equipped with an energy-dispersive X-ray spectrometer (EDS).

Figure 3-9 shows a three-wall BNNT encapsulated with KCl crystals. The EDS spectrum has confirmed that the encapsulated crystal is made by KCl. The crystal structure can be indexed to rock salt KCl. The inner diameter of the BNNT is found to be 1.32nm. Judging from the dark spots of in the image, the lattice constant along the axis of the BNNT of the encapsulated KCl crystal is found to be 3Å, which is less than its bulk value 3.15Å. However, for the direction perpendicular to the nanotube axis, the lattice constant is 3.45 Å, which is larger than the bulk value 3.15Å.

Figure 3-10 shows a BNNT filled with KBr crystals. The crystal structure can be indexed to rock salt KBr. The lattice constant along the axis of the BNNT of the encapsulated KBr crystal is found to be 3.16Å, which is less than its bulk value 3.3Å. For the direction perpendicular to the nanotube axis, the lattice constant is 3.16 Å, which is also smaller than the bulk value 3.3Å.

Figure 3-11 shows a BNNT filled with KI crystals. The crystal structure can be indexed to rock salt KI. The lattice constant along the axis of the BNNT of the encapsulated KI crystal is found to be 3.5Å, which is less than its bulk value 3.6Å. For the direction perpendicular to the nanotube axis, the lattice constant is 3.59 Å, which is comparable to the bulk value 3.6Å.

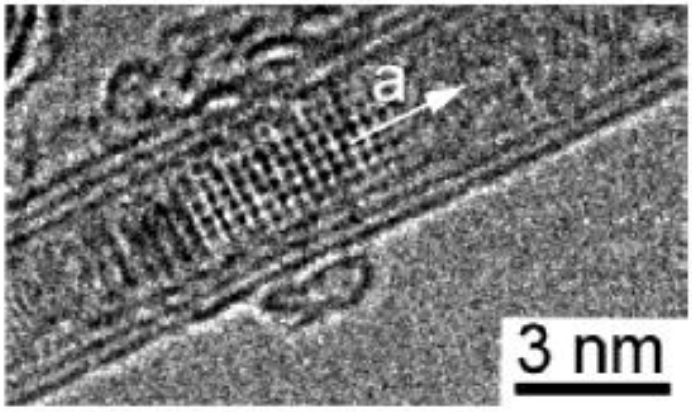

Figure 3-9 TEM image of a KCl-filled BNNT.

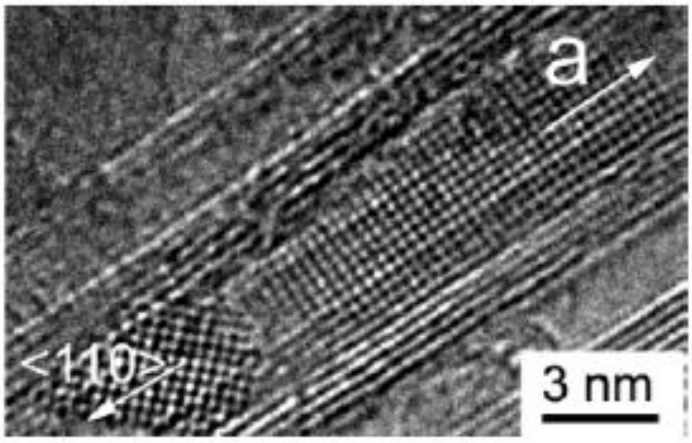

Figure 3-10 TEM image of a KBr-filled BNNT.

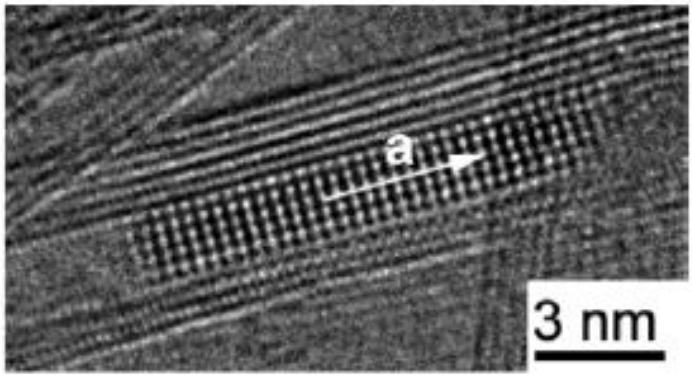

Figure 3-11 TEM image of a KI-filled BNNT.

Table 3-1 Summary for the lattice constants of various encapsulated potassium halide in BNNTs.

Bulk sample, lattice constant	Encapsulated sample, lattice constant parallel to BNNT axis	Encapsulated sample, lattice constant perpendicular to BNNT axis
KCl , 3.15Å	3.0Å (compressed, 4.8%)	3.45Å (expanded, 9.5%)
KBr, 3.3Å	3.16Å (compressed, 4.2%)	3.16Å (compressed, 4.2%)
KI, 3.6Å	3.5Å (compressed, 2.7%)	3.59Å (same)

Table 3-1 summarizes the result. In general, the lattices of the encapsulated potassium halide crystals parallel to the BNNT axis are compressed and their distortion ratio decreases as the atomic size of the halide element increases. On the other hand, the lattice of the encapsulated potassium halide crystals perpendicular to the BNNT axis can expand, compress, or remain unchanged. The dramatic changes of the lattice distortion perpendicular to the BNNT axis suggest that the confinement effect still plays an important role in the ionic crystals. Although the strong ionic bonding of potassium halides prevents severe lattice distortions or re-arrangements like the case of C_{60} encapsulated in BNNTs, the strongly compressed or expanded lattices may imply novel properties unseen in bulk materials. Actually, during the TEM imaging, Weiqiang Han observed in-situ cleaving of a KCl nanocrystal induced by electron beams [69], demonstrating a novel technique to engineer these nano-crystals inside TEM.

Chapter 4 Theory of thermal conductivity

4.1 The Boltzmann equation

The Boltzmann equation describes collision processes with a non-equilibrium distribution function *g(r, k, t)* in a phase space. In the absence of collisions *g(r, k, t)* is related by

$$g(\vec{r},\vec{k},t) = g(\vec{r} - \dot{\vec{r}}\Delta t, \vec{k} - \dot{\vec{k}}\Delta t, t - \Delta t) \tag{4.1}$$

It follows that

$$\frac{\partial g}{\partial t} = -\dot{\vec{r}}\frac{\partial g}{\partial \vec{r}} - \dot{\vec{k}}\frac{\partial g}{\partial \vec{k}} \tag{4.2}$$

Ludwig Boltzmann (1844~1906) added an additional term into Eq. (4-2) to account for collisions:

$$\frac{\partial g}{\partial t} = -\dot{\vec{r}}\frac{\partial g}{\partial \vec{r}} - \dot{\vec{k}}\frac{\partial g}{\partial \vec{k}} + \left(\frac{\partial g}{\partial t}\right)_{coll} \tag{4.3}$$

This is the Boltzmann equation. It balances the total time derivative with the rate of transfers in and out of the *g(r, k, t)* due to scattering.

However, the Boltzmann equation itself is difficult to solve. Typically the Boltzmann equation can be simplified by assuming a static distribution, so $\partial g/\partial t = 0$. Furthermore, one assumes only small deviations from equilibrium, such that

$$\left(\frac{\partial g}{\partial t}\right)_{coll} = -\frac{g(\vec{r},\vec{k}) - g^0(\vec{r},\vec{k})}{\tau} \tag{4.4}$$

where $g^0 = [\exp(E/k_BT)-1]^{-1}$. This is called the relaxation time approximation. With this approximation we can integrate both sides of Eq. (4.4) with respect to time.

$$g(\vec{r},\vec{k}) = \int_{-\infty}^{t} \frac{e^{-(t-t')/\tau}}{\tau} g^0(\vec{r}(t'),\vec{k}(t'),t')dt' \tag{4.5}$$

This can be integrated by parts to yield

$$\begin{aligned} g &= g^0 - \int_{-\infty}^{t} \frac{e^{-(t-t')/\tau}}{\tau} \frac{dg^o}{dt'} dt' \\ &= g^0 - \int_{-\infty}^{t} dt' \frac{e^{-(t-t')/\tau}}{\tau} (\dot{\vec{r}} \frac{\partial g^0}{\partial \dot{\vec{r}}} + \dot{\vec{k}} \frac{\partial g^0}{\partial \dot{\vec{k}}}) \end{aligned} \tag{4.6}$$

Assuming that the particles do not undergo acceleration under a long-time scale larger than the relaxation time, then the second term of Eq. (4.6) vanishes. We have

$$g = g^0 - \tau \dot{\vec{r}} \frac{\partial g^0}{\partial \dot{\vec{r}}} \tag{4.7}$$

from $g^0 = [\exp(E/k_BT)-1]^{-1}$, we have

$$\frac{\partial g^0}{\partial \dot{\vec{r}}} = E \frac{\nabla T}{T} \frac{\partial g^0}{\partial E} \tag{4.8}$$

so that

$$g = g^0 - \tau E \dot{\vec{r}} \cdot \frac{\nabla T}{T} \frac{\partial g^0}{\partial E} \tag{4.9}$$

Thus we can calculate the thermal current

$$\begin{aligned} j_U &= \int d\vec{k} E \vec{r} g(\vec{r}, \vec{k}, t) \\ &= -\tau \int d\vec{k} \frac{E^2}{T} \frac{\partial g^0}{\partial E} \vec{r}\vec{r} \cdot \nabla T \\ &= \kappa \nabla T \end{aligned} \tag{4.10}$$

where the integral is over the first Brillouin zone.

We can now express the thermal conductivity. For cubic crystals, the phonon velocity averages to $v^2/3$, and the integral now becomes

$$\begin{aligned} \kappa &= -\tau \frac{v^2}{3} \int d\vec{k} \frac{E^2}{T} \frac{\partial g^0}{\partial E} \\ &= \frac{1}{3} C v \ell \end{aligned} \tag{4.11}$$

where C is the heat capacity per unit volume, v is the average phonon velocity, and ℓ is the phonon mean free path.

The thermal conductivity of the conducting electrons can be obtained in a similar way. Thus we have

$$\kappa_e = \frac{1}{3} C_e v_F \ell_e \tag{4.12}$$

where C_e is the heat capacity per unit volume, v_F is the Fermi velocity, and ℓ_e is the eletron mean free path.

Thus we obtain the formula for thermal conductivity from a fundamental approach. In the derivation discussed above, we have assumed that the phonons undergo frequent collisions such that a well-defined temperature is established at each local point. Under

some conditions, these assumptions or approximations may not hold anymore. We will discuss these cases in later sessions.

4.2 N-process and U-process

The Boltzmann equation justifies the phenomenological model of Eq. (4.11) using the phonon mean free path (l). In principle, l is determined by two scattering processes, the phonon-phonon scattering and the scattering due to defects, isotope impurities, and boundaries. If the force between atoms were purely harmonic, there would be no phonon-phonon collisions. Generally, the anharmonic coupling strength increases with temperature. Thus it is predicted that l is proportional to $1/T \sim 1/T^2$ at high temperatures.

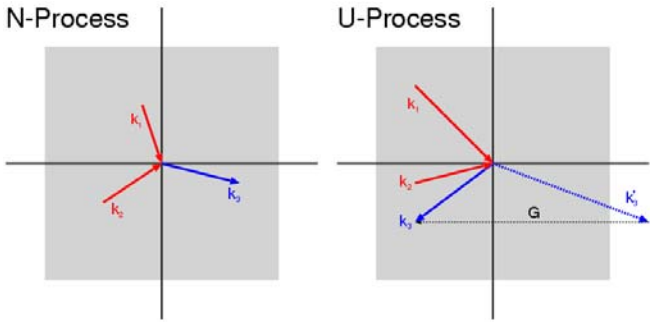

Figure 4-1 N-process and U-process

Peierls pointed out that for phonon-phonon scatterings whose resultant phonon momentum lies within the first Brillouin zone (N process), the scatterings only redistribute the phonon momentum but do not degrade the thermal conductance [70]. Only for collisions whose final momentum lies outside the first Brillouin zone will back-scattering events occur, thus reducing l. This is called as the umklapp or U process. In general, the phonon-phonon collisions can be expressed by

$$\vec{K}_1 + \vec{K}_2 = \vec{K}_3 + \vec{G} \tag{4.13}$$

where $\boldsymbol{K_i}$'s are the phonon momentum. When **G** = 0, it is called N process. When **G** is a reciprocal lattice vector, it is called U process. The difference between N process and U process can be seen in Fig. 4-1.

For U process to occur, it is necessary to have momenta of incident phonons larger than G/2. Thus U processes only happen at high temperatures when high energy phonons are excited. At low temperatures, the number of suitable phonons decreases exponentially. So the temperature dependent thermal conductivity of a material generally has a peak below which the phonon mean free path is not limited by phonon-phonon collisions.

4.3 Thermal conductivity of mesoscopic materials and the Casimir limit

At low temperature, the phonon mean free path becomes so long that the phonon-phonon collision events are rare. So the thermal transport process is similar to a hollow space filled with electromagnetic radiation. It is obvious that in this situation no localized thermal equilibrium can be established, although when a hot and a cold body are placed in such a space, heat will flow from the warmer to colder body.

H. B. G. Casimir analyzed the thermal conductivity at low temperature when the phonon mean free path is comparable to that of the specimen [71]. He noticed that under this condition, the quantity of the energy flow depends on the conditions of the crystal's boundaries. When the crystal's boundaries are like perfect mirrors, the heat flow is

independent of the length of the sample. Strictly speaking, no coefficient of heat conduction can be defined in this case. Casimir analyzed a second case where the boundaries are like rough walls so that phonons are diffusively scattered. He obtained the average phonon mean free path

$$\overline{\ell} = 1.12\sqrt{A} \tag{4.14}$$

which is known as the Casimir limit for the thermal conductivity of a sample with cross-sectional area A.

The Casimir limit puts a constraint on the upper limit of the phonon mean free path. People often refer the Casimir limit as a result from boundary scatterings. However, as emphasized earlier, the Casimir limit only applies to crystals with rough boundaries where diffusive scatterings occur. When the boundaries are polished smoothly, phonons collide with the walls elastically, the Casimir limit will not hold.

Klitsner *et al.* did a series of low temperature thermal conductivity experiments on rods of Si [72]. The phonon transport in highly polished rods of Si, with cross-sectional area A=0.5×0.5cm^2, was found to be ballistic in the temperature range of 0.05~1K. More than 95% of the phonons would scatter elastically from the polished surfaces of the Si rod. The phonon mean free path was found to be 10~15cm, corresponding to the contact spacing. After roughing the surfaces, the phonon mean free path was reduced to 0.48cm, corresponding to the Casimir limit for diffusive scattering.

Thermal conductivity of nanoscale rods of diameters 100~200nm were measured in Roukes' and Cleland's groups [73,74]. They found that the phonon mean free path reaches 3~10μm, exceeding the diameter of the rods. Deyu Li *et al.* measured the

thermal conductivity of Si nanowires (SiNWs) using the suspended test fixture similar to the ones I used [75]. They found that the thermal conductivity decreases as the diameter of the SiNWs decreases from 115nm to 22nm. They interpreted the reduction of the phonon mean free path due to the boundary scattering. However, several issues may arise before reaching this conclusion. First, the contact thermal resistance may increase as the diameters of the SiNWs decrease. Since it is difficult to evaluate the influence of the contact thermal resistance of their devices, the measured thermal conductivity value is uncertain. Second, to reduce the diameters of the SiNWs, one usually oxidizes the surface of the SiNWs then removes the SiO_2 by wet etching. It is not clear that how this oxidation-etching process affects the topography of the surface of the SiNW. If the oxidation-etching process leaves rough surfaces, the phonon mean free path of the small-diameter SiNWs will be constrained by the Casimir limit. On the other hand, the as synthesized SiNWs usually have very smooth surfaces; thereby the phonon mean free path should be much larger than their diameters.

4.4 Quantum of thermal conductance

When the phonon mean free path is much larger than the dimensions of the sample, the thermal transport enters into a ballistic phonon transport regime. From the Landauer energy flux formula

$$J_Q = \frac{\hbar^2}{2\pi k_B T^2} \sum_n \int_0^\infty d\omega \Im(\omega) \frac{\omega^2 e^{\hbar\omega/k_B T}}{(e^{\hbar\omega/k_B T} - 1)^2} \tag{4.15}$$

where J_Q is the energy flux, T is the transmission rate of phonons of frequency ω. Assuming $T = 1$, one can obtain the low temperature limit of the thermal conductance

$$\kappa = \frac{k_B^2 \pi^2}{3h} TN + \frac{k_B^2}{h} T \sum_n^N \left\{ \frac{\pi^2}{3} + \left(\frac{\hbar \omega_0}{k_B T} \right)^2 \frac{1}{1 - e^{-(\hbar\omega_0 / k_B T)}} + 2\mathrm{di}\log(e^{\hbar\omega_0 / k_B T}) \right\} \quad (4.16)$$

where N is the total number of acoustic phonon modes, dilog(x) is the dilogarithm integral,

$$\mathrm{di}\log(x) = \int_1^x \frac{\log t}{1-t} dt \,. \quad (4.17)$$

Thus Eq. (4.16) predicts a universal thermal conductance (G_0) of a single phonon mode with perfect transimissivity. On the other hand, the high energy modes show a dependence on the intrinsic properties of the materials and on the geometrical parameters of the sample through the cutoff frequencies ω_0.

When the temperature is lowered, all other optical phonons with finite cutoff frequencies vanish. Thus for a quasi-one dimensional system at low temperatures, there are four acoustic phonon modes contributing to heat transport. This prediction for the universal thermal conductance has been observed by Schwarb *et al.* [76].

One thing we have ignored above is the dependence of phonon transmissivity on the sample geometry, such as the shape of the contacts and surface roughness etc. Calculations have shown that these geometric effects will affect the temperature range where the $4G_0$ can be observed [77]. When such imperfect transmissivity of phonons is present, one can only further lower the temperature then the recovery of $4G_0$ can occur.

4.5 Theoretical and experimental overview of nanotube thermal conductivity

Many theorists have calculated the room temperature thermal conductivity (κ(290K)) of CNTs. Table 4-1 summarizes these results. It can be seen that there is a two-orders-of-magnitude discrepancy in the predicted value of κ(290K) of CNTs.

Molecular dynamics simulations suggest that the onset of the umklapp processes of a SWCNT to be around 120K like that of graphite [78-80]. However, so far no experimental data have shown a peak around 120K. The discrepancy between theory and experiment is not clear yet.

Due to their nano-size diameters, SWCNTs have been predicted to exhibit quantum thermal conductance $4G_0$ as high as 15K [81]. There is additional electronic contribution $4G_0$ if the SWCNT is a metallic quantum wire [81].

Experimentally, J. Hone *et al.* first measured κ of mats of SWCNTs [82]. However, the experimental measured value of κ is in the 0.1~1W/mK range. Although he estimated the intrinsic value κ(290K) of SWCNTs to be in 1750~5800W/mK range, his assumption is not well-justified.

Measurements on κ of mats of MWCNTs were done by various groups [41,83]. Experiments on CNT-polymer composite also showed improvements on the mechanical strength and the thermal conductivity [84]. Although these experiments did not give an absolute value of κ, these works indicated that CNTs are good thermal conductors.

Table 4-1 Summary for theoretical calculations on room temperature thermal conductivity of SWCNTs.

Reference	Room temperature value (W/mK)
N. G. Mensah *et al.*, Phys. Lett. A 329 (2004)	>55000 (only electron thermal conductivity)
J. X. Cao *et al.*, PRB 69, 073407 (2004)	9000~4500
W Zhang *et al.*, Nanotechnology 15, 936 (2004)	8000~1000 (wall thickness=3.4Å, depends on chirality)
S Berber *et al.*, PRL 84, 4613 (2000)	6600 (wall thickness=3.4Å)
J. Che *et al.*, Nanotechnology 11, 65 (2000)	2800 (1A thick (10, 10) SWCNT) (~823 if wall thickness=3.4Å)
A. Cummings *et al.*, PRB 70, 115405 (2004)	2000 (wall thickness=3.4Å)
M. A. Osman *et al.*, Nanotechnology 12, 21 (2001)	2000
M. Grujicic *et al.*, J of Material Science 40, 1943 (2005)	1600
E. G. Noya *et al.*, PRB 70, 115416 (2004)	1500 (wall thickness=3.4Å)
G. Zhang *et al.*, J Chem Phys. 123 114714 (2005)	800 (wall thickness=1.44Å) (~1940 if wall thickness=3.4Å)
S Maruyama, Physica B 323, 193 (2002)	500 (wall thickness=3.4Å)

The first thermal conductivity measurement on individual MWCNTs was done by P. Kim *et al.* using devices made by the Majumdar group [85]. κ(290K) was determined to be more than 3000W/mK. The diameter of the MWCNT investigated was determined to be 14±2nm using SEM imaging. The uncertainty in measuring the diameter of their MWCNT was believed to cause the greatest error in their results.

T. Y. Choi *et al.* measured the κ of individual MWCNTs using the 3ω method. κ(290K) was determined to be 650~830W/mK [86]. However, they determined the outer and the inner diameters of the investigated MWCNT by judging the contrast of the SEM image, which again introduced large errors.

M. Fujii *et al.* adapted a similar method as I did in measuring the thermal conductivity of MWCNTs [87]. They picked up a MWCNT using a manipulator then examined it under TEM. Then they put the MWCNT on a suspended micro-membrane and measured the thermal conductivity change before and after depositing the MWCNT on the membrane. The highest κ(290K) was determined to be 2000W/mK. They also found a diameter dependent κ(290K) relation.

E. Pop *et al.* employed indirect methods to measure κ by analyzing the nonlinear I-V curve of a suspended CNT [88]. They obtained κ(300K) = 3500W/mK for a 1.7nm diameter SWCNT. This self-heating-self-sensing approach was similar to the 3ω method, but it involved more complicated analyses. They determined the onset of umklapp process occurring at ~400K.

H. Y. Chiu *et al.* employed an indirect method by analyzing the breakdown resistance of CNTs at high current bias [89]. They compared the breakdown I-V curves of CNTs on substrates and suspended CNTs. They found that the suspended CNTs showed a characteristic difference. For CNTs' lengths less than 500nm, they found that the breakdown power became length-independent. They interpreted their results as signatures of ballistic phonon transport and the power dissipation of a CNT was limited by quantum thermal conductance of the MWCNT. However, adapting the quantum thermal transport formula in their analysis had ignored phonon-phonon scatterings at high temperatures, which is not a reasonable assumption.

Chapter 5 Thermal conductivity of B-C-N and BN nanotube mats

5.1 Experimental methods

There are many methods to measure the thermal conductivity of a bulk material. The absolute method employs direct measurements of the power delivered to the sample, and the temperature across the specimen. Usually, a resistive heater is attached to the end of a specimen and two pairs of thermocouples are attached to the sample to measure the temperature difference. However, the absolute method involves tedious calibration procedures because the heat loss through the thermocouples and the heater wires, as well as the radiation loss to the environment need to be determined to high accuracy. For small samples, the radiation loss from the heater can be very large. Furthermore, to reduce the heat loss from the wires connected to the heater, it is required to use some resistive fine wires. But the fine wires introduce uncertainties to the heater resistance. To accurately determine the resistance of the heater, a four-wire configuration is needed. But the two additional wires introduce more uncertainties due to heat loss. How to balance the experimental accuracy and uncertainty is a delicate issue for the absolute method.

A dynamical approach known as the 3ω method has become popular in recent years due to its superior efficiency in measuring thermal conductivity of thin films [90]. The 3ω method is based on the idea of self-heating and self-sensing. An ac current with frequency ω is applied to a suspended conducting sample. Due to joule heating ($P=I^2R$), the power dissipation fluctuates at a frequency of 2ω. If the sample resistance changes as a simple function of temperature, then there is a corresponding resistance fluctuation at a frequency of 2ω. Due to Ohm's law ($V=I(\omega)R(2\omega)$), the temperature difference across the sample can be detected by a lock-in amplifier with reference frequency at 3ω. However, the 3ω method requires the sample to be conducting, which is not suitable for BNNTs. Besides, it also requires the sample resistance to be sensitive to temperature. Moreover, the 3ω method involves complicated analysis of the experimental results. In order to choose a proper working frequency, quantities like thermal diffusive length and relaxation time need to be estimated in advance.

A comparative method is chosen to measure the thermal conductivity of B-C-N nanotube and BNNT mats. The method requires a heater/sample/reference material to be connected in series, so the heat flux is the same through the reference material and the sample. The temperatures across the reference material and the sample are simultaneously measured. The thermal conductance (K) of the sample is then:

$$K_{sample} = K_{ref} \frac{\Delta T_{ref}}{\Delta T_{sample}} \tag{5.1}$$

where ΔT_{ref}, ΔT_{sample} are temperature differences across the reference and the sample, respectively. The method has advantages that once the thermal conductance of the reference material is known, the thermal conductance of the sample can be measured very easily. Besides, the heat loss due to the wires connecting to the heater will not affect the measurement. The largest error is due to the heat loss through the thermocouples, but it can be largely eliminated by choosing constantan rod as the reference material. Thus the number of the wires contributing to the heat loss is reduced.

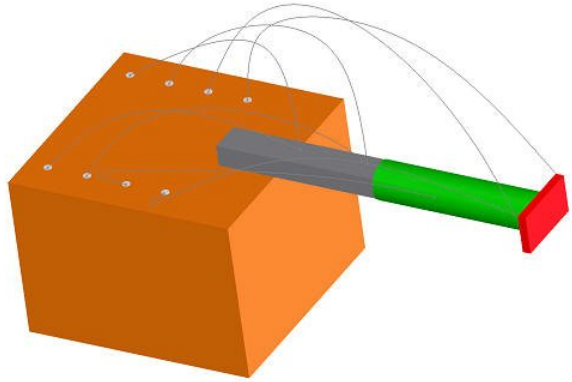

Figure 5-1 Schematic experimental setup for meausuring thermal conductivity of BNNT mats.

The experimental setup is shown in Fig. 5-1. A silicon chip resistor ~2KΩ was attached to the end of the sample. Because the sample needed to be removed after the measurement, I used GE varnish to glue together the heater/sample/reference assembly. The reference was mounted on the heat bath using stycast, which is known to have good thermal conductivity. I used 0.5mil type E (Constantan/Chromel) thermocouples to measure the temperature difference across the sample. The thermocouples should be as long as possible to eliminate the heat loss, but they should not be too long to have thermal contacts to the shield or heat bath. The constantan rod was 20mil in diameter and 2cm

long. Two 0.5 mil Chromel wires were attached to it using silver paint. Mounting the two pairs of thermocouples on the sample was the most difficult part. The thermocouples were first spark-bonded, then a layer of silver epoxy was applied to the junction. This gave good electrical and thermal contact. Then the thermocouples were glued on the sample surface using GE varnish. GE varnish could be removed when transforming the B-C-N nanotube mats into BNNT mats. It took some time to learn how to mount the thermocouples nicely on the sample surface. Since the thermocouples were long and twisted, the tension tended to drive the junction away from the sample surface before the GE varnish dried. I usually bent the thermocouple slightly above the desired location with a manipulator then quickly applied the GE varnish and lowered the manipulator until the junction attached to the sample firmly. Ideally, the area of the junction should be as small as possible to improve temperature resolution. But since the thermocouple only had sensitivity ~0.1K and the temperature across the sample was ~1K, a junction area within 1/10 of the sample size was acceptable.

The heat bath was made of a copper block with a temperature sensor attached near the reference material. Another temperature sensor was attached near the bath heater so that the temperature controller could control the bath temperature without time delay. The radiation shield also had a heater and a temperature sensor on it. During the measurement, the temperature of the heat bath and the radiation shield should be kept as close as possible to minimize the radiation loss. In some measurements I employed two constantan rods: one before, one after the sample to estimate the heat loss through radiation and the thermocouples. Two Keithley 182 nanovoltmeters were used to

measure the temperature difference across the sample. Another Keithley 181 nanovoltmeter was used to measure the temperature difference across the reference. A good temperature control on the heat bath was necessary because when the temperature fluctuated, the steady state condition no longer held and it usually led to a jump in the $\kappa(T)$ curve. The whole sample space was pumped below 5×10^{-6} torr throughout the measurement.

The thermal conductivity of the constantan reference rod can be found in literature [91]. I also measured the thermal conductivity of a copper rod, but found that copper itself is not a good reference material. Because the impurity level of copper greatly affects its low temperature thermal conductivity, and it is also very sensitive to the annealing conditions. In the literature, the reported thermal conductivity data of copper also varies from one reference to another due to above reasons [92].

5.2 B-C-N and BN nanotube samples

The B-C-N nanotube and BNNT mats samples were made by Weiqiang Han. B-C-N nanotubes were synthesized by a substitution reaction using MWCNTs as a template. B_2O_3 powder was placed in a crucible covered with CNTs. The crucible was held in a flowing nitrogen atmosphere at 1600°C for 30mins. The mats of B-C-N nanotubes were made by first pressing the samples, followed by annealing at 150°C in air. B-C-N nanotubes were transformed into BNNTs by a subsequent oxidation treatment at 650°C. The microstructure of the nanotubes was characterized by high-resolution transmission electron microscopy. B-C-N nanotubes or BNNTs made by this method are

predominantly multi-walled with an average diameter 6~8nm [60]. Electron energy loss spectroscopy (EELS) shows that the carbon concentration is very low after transforming the B-C-N nanotubes into BNNTs. This result demonstrates that the BNNTs synthesized by this method are free of carbon.

Since the synthesized B-C-N nanotubes are based on the substitution reaction, there are several possible structures. As shown in Fig. 5-2, the first possible structure some of the carbon atoms of a CNT are replaced by boron or nitrogen atoms. For the second possibility some of the fragments of a CNT are substituted by a BNNT. For the third possibility the carbon layers and BN layers are separated along the radial direction like a coaxial cable.

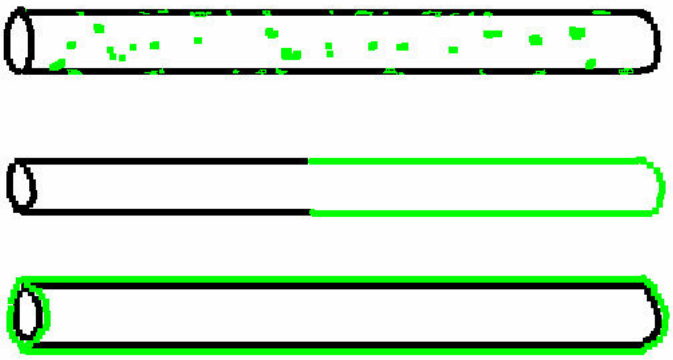

Figure 5-2 Three possible BCN nanotube structures

There are several reasons that made us to believe that the B-C-N nanotubes made by this method are highly phase separated along the radial direction like a coaxial cable.

If the first possibility is true, I should see a lot of defects on the BNNTs after they are converted from B-C-N nanotubes. But the TEM images do not show defective structures for these BNNTs. So the first possibility is excluded.

If the second possibility is true, since the carbon fragments will be removed after oxidation, the length of the BNNTs should be much shorter than the original MWCNTs. But actually the TEM images show that the length of the BNNTs is roughly the same as that of the original MWCNTs. Thus it excludes the second possibility.

Recent Raman and electron energy loss spectroscopy studies indicated that B-C-N nanotubes have strong phase separation between BN layers and carbon layers [93]. This result favors the third possibility.

The coaxial-cable-like structure of the B-C-N nanotubes enables us to estimate the intrinsic thermal conductivity of BNNTs more precisely than other nanotube mats measurements.

5.3 Results

The whole measurement process was as follows. First, I measured $\kappa(T)$ of mats of B-C-N nanotubes. Next, to estimate the carbon concentration in each sample, I used thermogravimetric analysis (TGA) to monitor the weight loss while heating the sample in oxygen at 650°C for ~30mins, as shown in Fig. 5-3. This process had been demonstrated to completely remove the CNTs and transform the B-C-N nanotubes to pure BNNTs. I found that this heating process did not affect the macroscopic geometry of the sample after burning. Also note that the oxidation of BNNTs occurs at 800°C as shown in Fig.

5-3. Finally, converted samples were mounted back on the thermal conductivity probe with the same thermocouple locations to minimize the geometrical uncertainties. *κ(T)* of the mats of BNNTs was then measured.

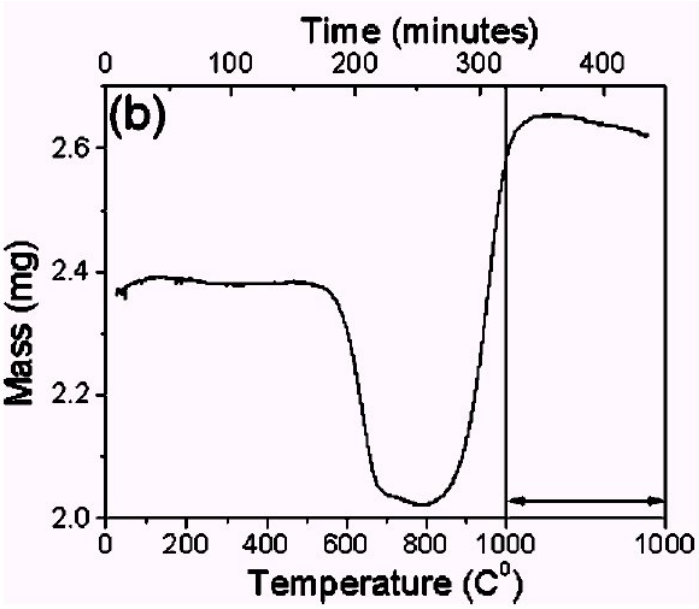

Figure 5-3 The B-C-N nanotube burning curve

Figures 5-4(a) and (b) show *κ(T)* of two samples before (B-C-N) and after (BN) the oxidation treatment. Both *κ(T)*'s of B-C-N nanotubes and BNNTs show increasing thermal conductivity with increasing temperature. Note that the value *κ(T)* shown here is the measured thermal conductivity without any density correction adapted in Ref. [82] and Ref. [41]. A small slope change can be seen at ~100K for BNNTs. The umklapp processes for hexagonal BN occurs at $T_U \sim$ 100K [56], which indicates that the slope change of *κ(T)* of BNNTs may be due to the umklapp processes in the mats. Since each nanotube has different chirality, the non-uniformity of the unit cell from one nanotube to another is expected to lead to a wide distribution of T_U in the mats. This would result in a

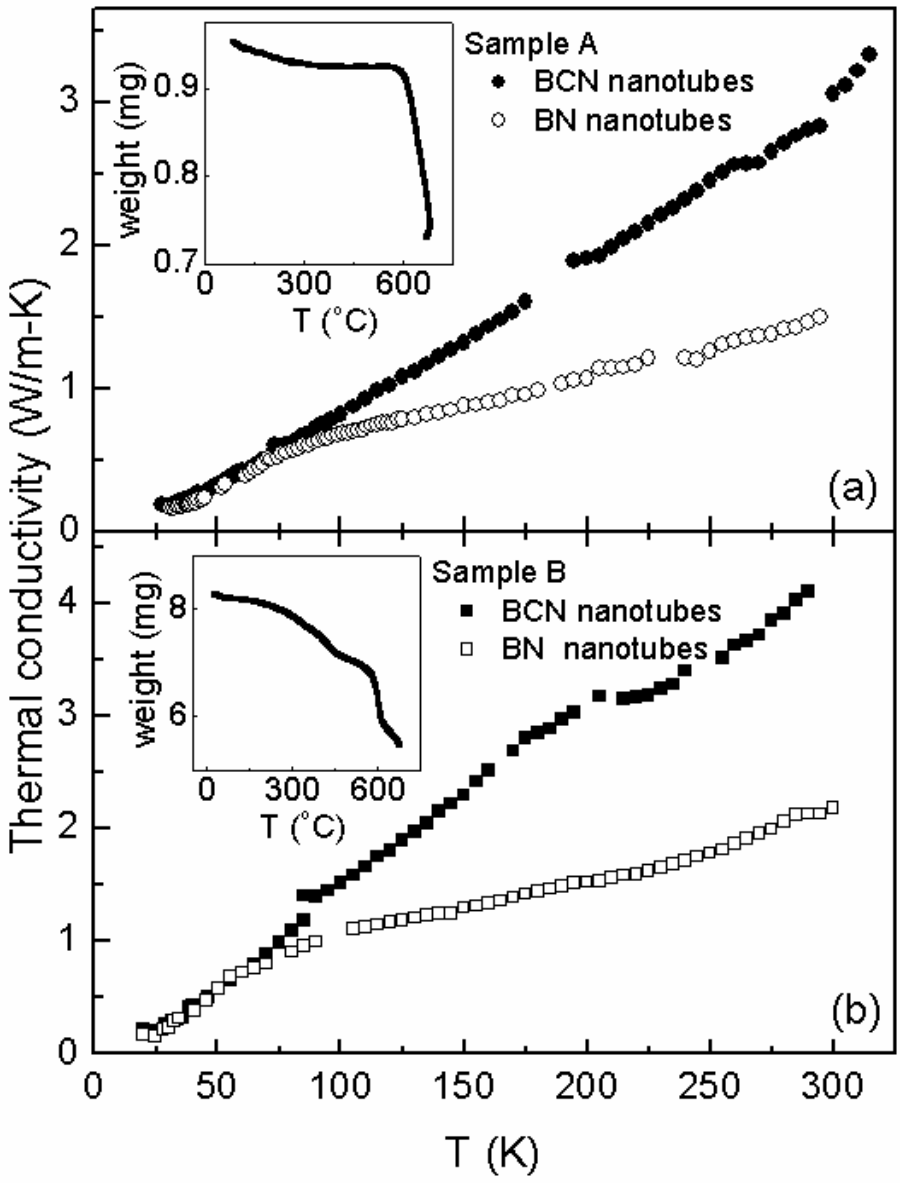

Figure 5-4 Thermal conductivity vs. temperature for two different samples of nanotubes (a) before (solid symbols, B-C-N) and (b) after (open symbols, BN) the oxidation treatment. Insets show the corresponding weight vs. temperature for each sample during the oxidation treatment. The weight ratio of carbon to BN is 0.30 and 0.50 in (a) and (b), respectively.

somewhat smeared umklapp signature in the *κ(T)* data. Similar observations have been reported for *κ(T)* of mats of CNTs [41,82].

The insets of Fig. 5-4(a) and (b) show the weight vs. temperature monitored by TGA. Samples of Fig. 5-4(a) and (b) have a carbon to BN weight ratio 0.30 and 0.50, respectively. Since the difference between the molecular weight of C_2 and BN is small, the weight ratio can be approximated to the number ratio of carbon layers to BN layers in each B-C-N nanotube.

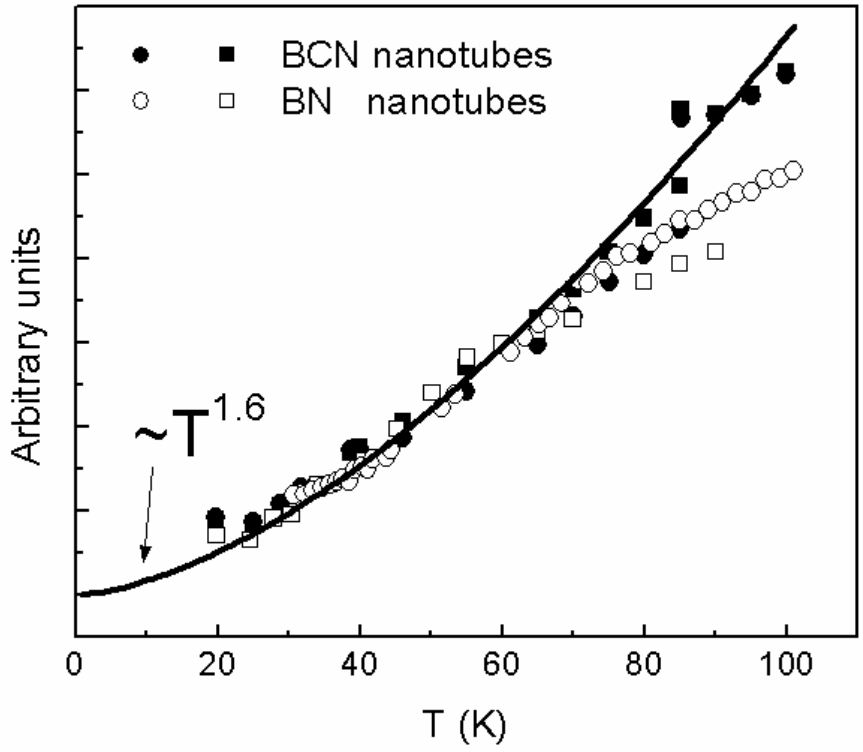

Figure 5-5 Low temperature behavior of *κ(T)* for B-C-N and BN nanotubes shown in Fig. 1. All the curves are normalized and can be fitted to a $T^{1.6}$ curve (solid line) below 70K.

Figure 5-5 shows the low temperature behavior of $\kappa(T)$ of B-C-N nanotubes and BNNTs. All the curves are normalized and can be fitted to a $T^{1.6}$ dependent curve for T < 70K. Since at low temperature $\kappa(T)$ is dominated by the heat capacity, the fact that the $\kappa(T)$ deviates from a linear temperature dependent behavior reflects the intrinsic dimensionality of most large diameter nanotubes. Similar dimensionality effects on the low temperature $\kappa(T)$ have been observed for SWCNTs and MWCNTs [41,82].

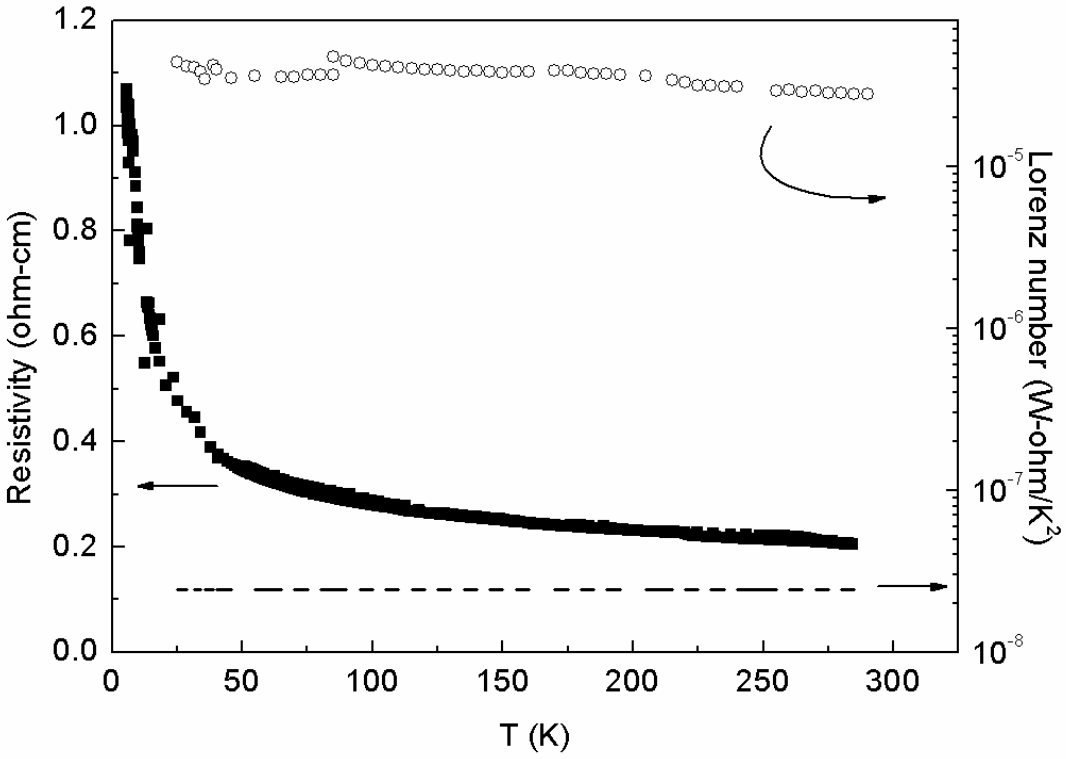

Figure 5-6 Temperature dependent resistivity of sample A (solid squares) and its corresponding Lorenz number (open circles). The Lorenz number derived from the free electron gas is also shown for comparison (dash lines).

Figure 5-6 shows the temperature dependent electrical resistivity of sample A and its corresponding Lorenz number $L = \kappa\sigma/T$. The Lorenz number gives a good estimation of the electronic contribution to the total thermal conductivity. Comparing with the value derived from the free election gas ($L_0 = 2.45\times10^{-8}$ W-ohm/K^2), the measured L is three orders of magnitude larger than L_0. Therefore, the thermal conductivity of B-C-N nanotubes is dominated by phonons for temperature below 300K. This result is also consistent with the experiment on SWCNT mats [94].

Of prime interest is the magnitude of the intrinsic thermal conductivity of BNNTs. Although previous experimental results on $\kappa(T)$ of mats of CNTs reflect the intrinsic dimensionality of nanotubes at low temperature, the traditional experimental methods only give a lower limit of the magnitude of the intrinsic $\kappa(T)$ of a single nanotube. For example, the uncorrected $\kappa($290K$)$ of SWCNT mats is only 0.7W/mK which is believed to be lower than the intrinsic value by a factor of 2500~8300 [82]. Besides, even if the measured $\kappa(T)$'s are corrected for the theoretical density of a close-packed bundle, the density correction factor in the reported $\kappa(T)$'s of mats are highly uncertain due to the difficulty in determining the actual microscopic sample geometry. For example, the corrected $\kappa($290K$)$ of MWCNT mats is only 25W/mK [41], while that of magnetically aligned SWCNT films is 250W/mK. However, these values are still one to two orders of magnitudes smaller than that of an isolated MWCNT measured by a micro-fabricated device (3000W/mK) [85]. Moreover, the electrical conductivity assumption used in Ref. [82] does not apply for insulating BNNTs. In the following paragraphs, I will use a novel analysis method to constrain the value of $\kappa(T)$ of an individual, multi-walled BNNT.

To estimate $\kappa(T)$ of a single BN nanotube, I employ an analysis method that necessitates the following justifiable assumptions:

(1). For a single B-C-N nanotube, the BN layers and carbon layers have parallel contributions to the total thermal conductance.

(2). Except for the carbon layers being removed from each B-C-N nanotube, the microscopic sample geometry does not change after the oxidation treatment.

The first assumption can be justified by the highly anisotropic thermal conductivity of graphite or hexagonal BN (c-axis vs. a-b plane). The weak van der Waals force implies that the intra-tube or inter-tube interactions have negligible contribution to the total thermal conductivity of B-C-N nanotubes in the axial direction. The second assumption relies on the structure of the outermost layer of B-C-N nanotubes. If the outermost layer is a BN layer, I expect that the microscopic geometry will not change after the oxidation treatment. If the outermost layer contains a carbon layer, the inter-tube interaction becomes weaker after the oxidation treatment (in which case the following analysis will underestimate the thermal conductivity of a BNNT).

The following analysis is based on the inequality:

$$\frac{A+m}{B+m} < \frac{A}{B} \quad if \ A > B, \ m > 0 \tag{5.2}$$

Since the measured thermal conductivity not only has contributions from nanotubes in the axial direction but also is limited by junctions across nanotubes, I adapt Matthiessen's rule for thermal conductance:

$$\frac{1}{\lambda_{mats}} = \frac{1}{K_{tube}} + \frac{1}{K_{jun}} \tag{5.3}$$

where λ_{mats} is the measured thermal conductance from the mats, K_{tube} and K_{jun} represent the sum of the thermal conductance from a single nanotube in the axial direction and across the nanotube junctions, respectively. Because the thermal conductance of a B-C-N nanotube is larger than that of its BN layers, Eqs. (5.2) and (5.3) give an upper limit of the thermal conductivity of BNNTs:

$$r \equiv \frac{\lambda_{BCN}}{\lambda_{BN}} = \frac{1/\lambda_{BN}}{1/\lambda_{BCN}} = \frac{1/K_{BN} + 1/K_{jun}}{1/K_{BCN} + 1/K_{jun}} < \frac{1/K_{BN}}{1/K_{BCN}} = \frac{K_{BCN}}{K_{BN}} = \frac{K_{BN} + K_C}{K_{BN}} = \frac{\kappa_{BN} + x\kappa_C}{\kappa_{BN}}$$

$$\Rightarrow \kappa_{BN} < \frac{x\kappa_C}{r-1} \tag{5.4}$$

where the subscripts of λ's and K's denote the thermal conductance contribution from B-C-N nanotubes, BNNTs, and CNTs, respectively. The subscripts of κ's are the thermal conductivity of BNNTs and CNTs. x denotes the number ratio of carbon layers to BN layers in each B-C-N nanotube. Since my nanotubes have large diameters, the ratio of the cross sectional area of carbon to BN layers in each B-C-N nanotube is approximately x. Similarly, Eqs. (5.2) and (5.3) also constrain the lower limit of κ_{BN}:

$$\frac{\lambda_{BCN}}{\lambda_C} = \frac{\lambda_{BCN}}{\lambda_{BCN} - \lambda_{BN}} \equiv \frac{r}{r-1} = \frac{1/\lambda_C}{1/\lambda_{BCN}} = \frac{1/K_C + 1/K_{jun}}{1/K_{BCN} + 1/K_{jun}} < \frac{1/K_C}{1/K_{BCN}} = \frac{K_{BCN}}{K_C} = \frac{\kappa_{BN} + x\kappa_C}{x\kappa_C}$$

$$\Rightarrow \kappa_{BN} > (\frac{rx}{r-1} - 1)\kappa_C \tag{5.5}$$

I emphasize that κ_{BN} and κ_C represent the ensemble-averaged thermal conductivity of an individual multi-walled nanotube, not the mats of the BNNT and CNT, respectively.

From Eqs. (5.4) and (5.5), I determine κ_{BN} at 290K to be $0<\kappa_{BN}<0.32\kappa_C$ and $0.04\kappa_C<\kappa_{BN}<0.54\kappa_C$ for samples A and B, respectively. A self-consistent constraint further narrows the window down to $0.04\kappa_C<\kappa_{BN}<0.32\kappa_C$. Since MWCNTs have been

shown to exhibit very high thermal conductivity (~3000W/mK at 290K), my result suggests that κ(290K) of an individual nanotube also lies in the range of 120W/mK ~ 960W/mK. Thus $\kappa(T)$ of an individual BNNT is one to two orders of magnitudes larger than that of the mat samples.

The total thermal conductivity of a nanotube can be written as $\kappa(T)=\sum Cv\ell$, where C, v, and ℓ are respectively the specific heat, group velocity, and phonon mean-free-path, and the sum is over all phonon states. Since currently there are no available data for heat capacity of BNNTs, I assume the ratio of heat capacity of hexagonal BN to graphite to be the same as that of BNNTs to CNTs. Choosing v = 10km/s estimated by theory [38,58], we have ℓ = 40 ~ 320nm for BNNTs, which is comparable to ℓ ~ 500nm for an isolated MWCNT, and is only a fraction of the average length (~2μm) of the BNNTs.

My results suggest that although κ(290K) of BNNTs is lower than that of CNTs, it is still higher than that of most other nano-scaled structures. For example, Si or Si/Ge nanowires exhibit lower thermal conductivity than their bulk values [95,96]. In these nanowires, suppressions of the phonon transport from boundary scattering, or alloy scattering overwhelm the enhancement due to reduced dimensionality. My results suggest that the tubular structure is the crucial factor for enhancing thermal conductivity of nano-scaled structures.

There are several reasons why BNNTs exhibit lower thermal conductivity than CNTs. First, theoretical calculations suggest a softer phonon mode in all branches of phonon dispersion curves for BNNTs than for CNTs [58]. Second, calculations also suggest the bulk modulus to be lower for BNNTs than for CNTs. Third, since the natural

abundance of boron is 19.9% ^{10}B and 80.1% ^{11}B, in contrast with that of carbon (98.9% ^{12}C, 1.1% ^{13}C), the effect of isotope disorder is much more severe for BNNTs than for CNTs. Theoretical calculations have suggested a larger enhancement factor of thermal conductivity (κ(isotopically pure)/κ(natural abundance)) for cubic BN (125%) than that of diamond (23%) [97]. Because the disorder-induced localization effect is more pronounced in one dimension, it is expected that such an enhancement factor to be much higher for BNNTs. Therefore, BNNTs can be as good thermal conductors as CNTs if made isotopically pure.

Chapter 6 Experimental methods of measuring thermal conductivity of individual nanotubes

6.1 Device

Microfabricated thermal devices were first developed by Li Shi and later by Deyu Li in the Majumdar group in the Mechanical Engineering department of UC Berkeley. As shown in figure 6-1, the device has two adjacent 14μm × 25μm silicon nitride (SiN_x) membranes suspended with five 0.5μm-thick, 420μm-long and 2μm-wide silicon nitride beams. A 30nm-thick and 300nm-wide platinum resistance thermometer coil is patterned on each membrane. Four of the Pt electrodes on each membrane are used for four-wire resistance measurements and one for electrical resistance or thermopower measurements. The gap between the two membranes varies from 2.5μm to 5μm. Nanowire or nanotube samples are put on top of the electrodes for thermal transport measurement. Further details of the microfabricated thermal device can be found in Ref. [98].

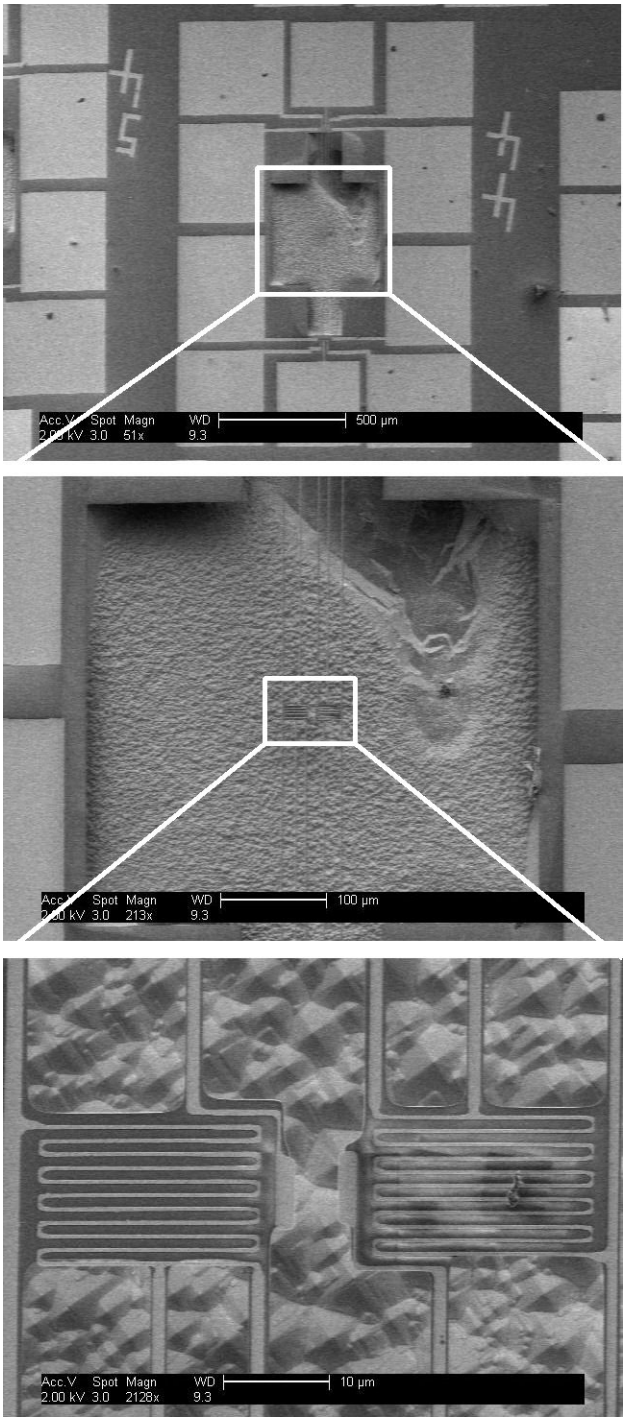

Figure 6-1 SEM images of the thermal device. From top to bottom: low magnification to high magnification.

Adam Fennimore and I further improved the thermal device by making it TEM transparent, thus it gave us the ability to characterize the structure of the measured nanotube. The procedures for making TEM-transparent thermal device are as follows.

The idea is to make a hole just beneath the sample so that it can be observed in a TEM. The suspended structure has exposed Si beneath it and a 0.5μm-thick SiN_x membrane on the back side of the chip. To remove the SiN_x membrane, one can use the reactive ion etching (RIE). Since it is not necessary to remove all of the SiN_x on the back side, I simply scratched the back side of the device using a diamond scratch. Then the devices were cleaved to fit the sample holder of the TEM. Later the devices were put into the tetramethylammonium hydroxide (TMAH, ~10%, 85°C) solution and etched for ~2.5 to 3 hours. To remove the residues of TMAH, the devices were rinsed with water. The suspended structures are usually strong enough and do not collapse. After etching, it is easy to see a hole just beneath the sample location.

6.2 Sample preparation and manipulation

Another challenge in measuring thermal conductivity of nano-scale materials was to put the nano-scale materials at the desired position. Andrei Afanasiev and I had tried many different approaches. One common method employed putting the nanotubes in isopropanol then dispersed them on the device. This method had been adapted for measuring thermal conductivity of Si nanowires and Si/Ge superlattice nanowires in the Majumdar group [95,96]. But considering the limited number of devices and low successful rate, this method was not suitable for nanotubes. Andrei Afanasiev also tried

to apply a voltage across the electrodes to align the nanotubes. But it always ended up with nanotube bundles instead of a single nanotube deposited across the gap. As shown in Fig. 6-2(a) and (b), the solution deposition method is basically a random process that always produces samples containing bundles of nanotubes and is not suitable for my measurement.

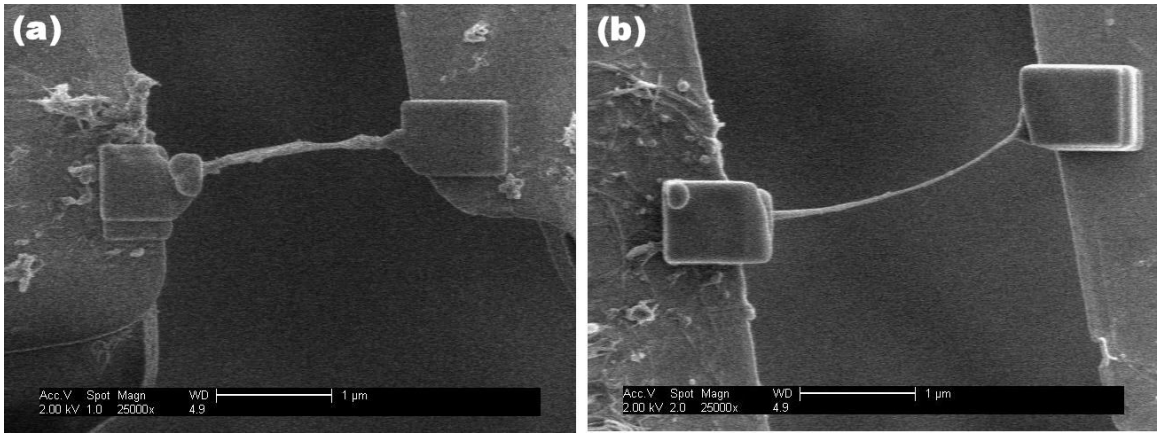

Figure 6-2 BNNT devices made by solution deposition method—the results usually contain bundles of nanotubes.

Another method employed a sharp tip to pick up the sample and put it on the desired location. Philip Kim had used this method to prepare his MWCNT samples [98]. He employed a probe station and a high-resolution dark-field optical microscope to place MWCNTs across the gap. However, this process was very tedious and difficult to control.

In the lab, I employed a pizeo-driven manipulator to prepare the samples in-situ inside the SEM of the Zettl group. A pizeo-driven manipulator made by *Attocube Systems* was assembled by Tom Yuzvinsky to manipulate nanostructure materials. The manipulation of nanotubes using *Attocube* involved several procedures, described in the following.

Sharp tungsten tips are crucial for manipulating nanotubes. They could be prepared by using the same method as making STM tips. I found a method that can repeatedly make very sharp tips. 2N NaOH solution, 10mil tungsten wire were used for etching. Generally, a biased voltage of 5V and a termination current of 10mA were good to make very sharp tips. However, the tip end might start to become blunt after the first few tips were made. So it is necessary to look at the shape of the tip under an optical microscope after each etching. If the tip started to become blunt, then reduce the voltage by 0.1~0.2V. Then the tip would become sharp again. When finished, the tip was dipped into hot water (~80°C) to remove the residue NaOH crystals sticking to the tip.

BNNTs were prepared by David Okawa and co-workers using magnesium oxide and boron CVD synthesis methods. Since the minimum distance of the gap of the thermal device is ~2.5μm, the length of the nanotube is critical to my experiments. Thanks to David Okawa's efforts, many multiwalled BNNTs with lengths exceeding 5μm are now available. Nanotube samples for *Attocube* manipulation were prepared by dispersing the nanotube-isopropanol solution on a hot Si chip. The evaporation of isopropanol drove the nanotube to the edges of the Si chip. When the solution dried, many nanotubes could be found hanging on the edge of the Si chip. These were the best locations to pick up a nanotube.

Another method to pick up a nanotube employed TEM grids obtained from Ted Pella, Inc. These TEM grids were made of thin and porous metallic films. Nanotubes were dispersed on them using the solution deposition method. Once a good nanotube was located, the tungsten tip can approach it and break the underlying porous films if

necessary (shown in Fig. 6-3). This method is especially useful for arc-grown CNTs, for which long nanotubes were not as common as BNNTs.

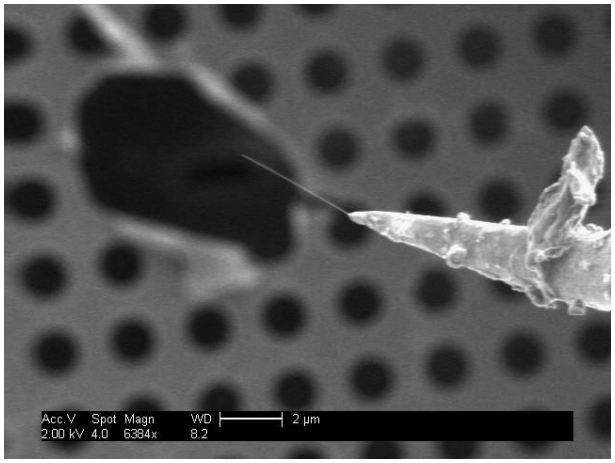

Figure 6-3 a CNT picked up by a tungsten tip. The underlying image shows the TEM grid described in (3).

After touching the nanotube with the tungsten tip, trimethyl cyclopentadienyl platinum ($C_9H_{16}Pt$) was deposited on the joint to strengthen the bonding. Then the nanotube was moved to the desired location ("2" in Fig. 6-4). After depositing the nanotube on the device, one end of the nanotube was anchored to one side of the electrode by depositing $C_9H_{16}Pt$ on it ("3" in Fig. 6-4). Then the nanotube was released by cutting it with a focused electron beam. Finally, the other end of the nanotube was anchored to the other side of the electrode by depositing $C_9H_{16}Pt$ on it ("4" Fig. 6-4).

The nanotube was then transferred to a TEM stage, where its structure could be determined. Figure 6-5(a) shows a SEM image and the corresponding low resolution TEM image of a BNNT (shown in the inset of Fig. 6-5(a)). Due to vibrations of the suspended nanotube, a high resolution image can usually be taken only at the edge of the nanotube where it is strongly anchored. But this is where the $C_9H_{16}Pt$ contamination is most serious. For TEM imaging, finding a good spot to look at can be time-consuming.

Figures 6-5(b) and (c) show the high resolution TEM image of a BNNT and its diffraction pattern. Since I tend to select the longest nanotubes during the *Attocube* manipulation, the nanotubes prepared on the devices are usually thick (30nm~40nm) and long (>5μm).

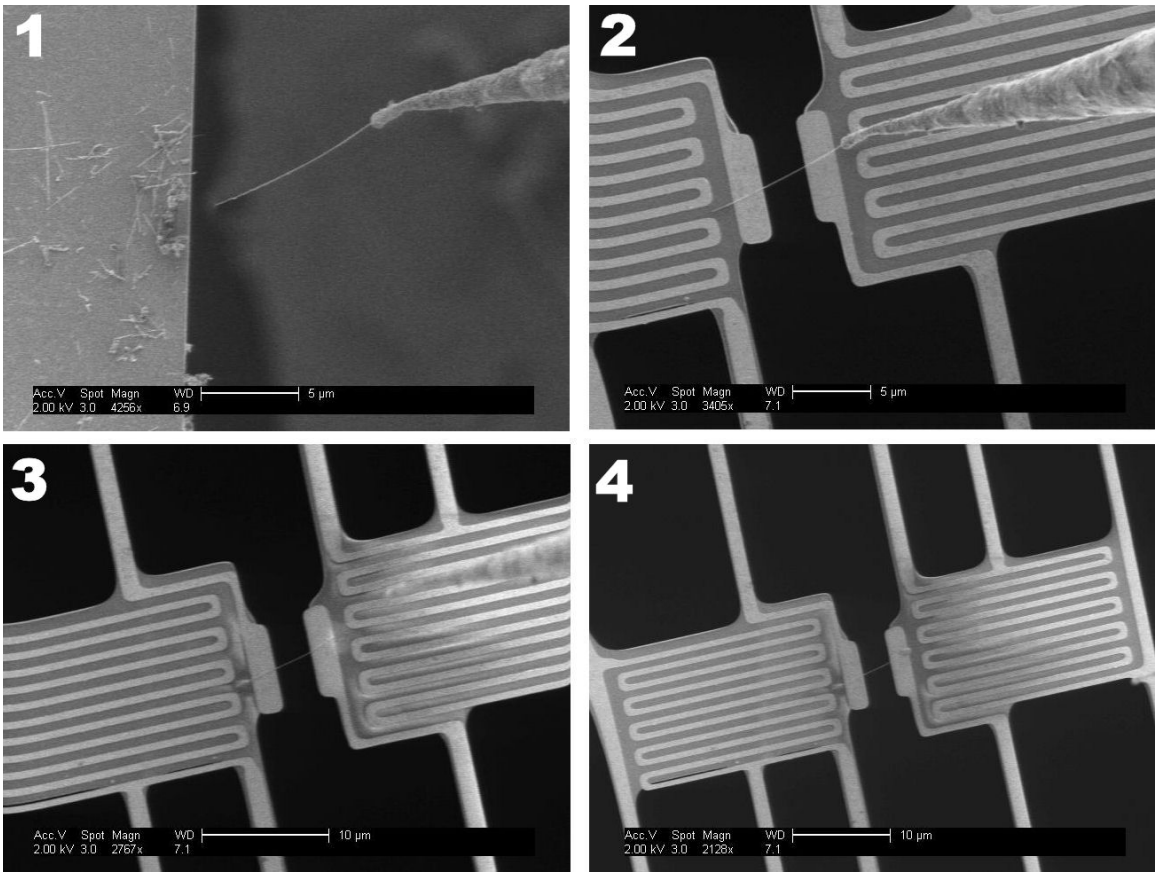

Figure 6-4 The procedures of using Attocube manipulator for preparing a BNNT device. 1. Pick up a BNNT from the edge of a Si chip. 2. Move to the thermal device. 3. Deposit $C_9H_{16}Pt$ so that the BNNT is anchored to one of the electrodes. 4. Cut the BNNT using focused electron beam and deposit $C_9H_{16}Pt$ on the other side of the BNNT then remove the tungsten tip.

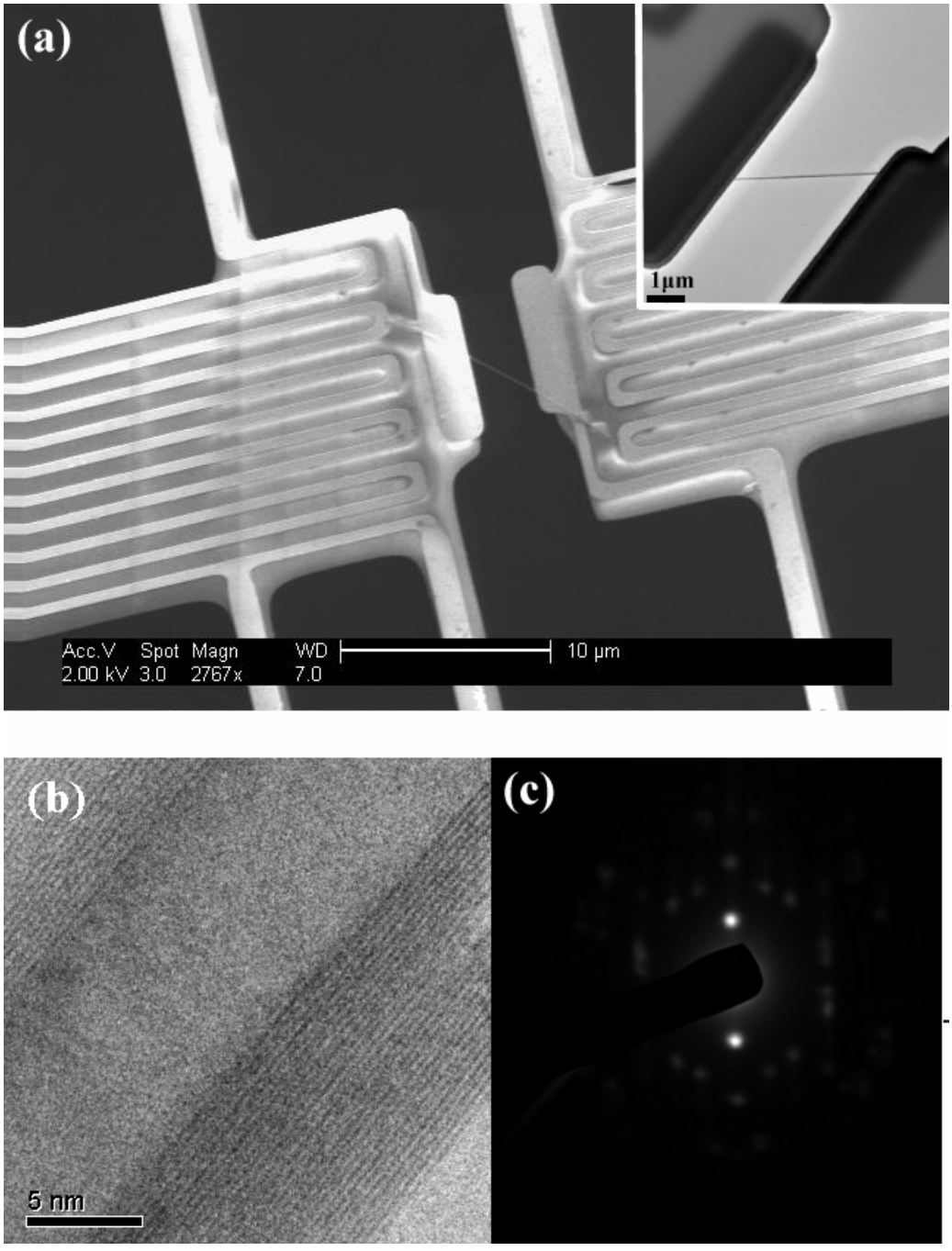

Figure 6-5(a). An SEM image of the microfabricated test fixture with a BNNT on it (scale bar = 10µm). The inset shows the corresponding TEM image of the same device (scale bar = 1µm). (b). A high-resolution TEM image of the BNNT (scale bar = 5nm). (c). The corresponding electron diffraction pattern of the BNNT.

6.3 Measurement scheme

For κ(T) measurements, the bath temperature was controlled by a Lakeshore 340 temperature controller. The sample was mounted inside a high vacuum home-made probe. After the system reached a steady state, a known power (P) was slowly ramped on the heater pad. The resistance changes of the heater and sensor pads were simultaneously measured. The schematic diagram of the measurement is shown in Fig. 6-6. The ramping current generates Joule heat on the heater. Part of the heat raises the temperature on the heater, while the other part of the heat flows through the sample and raises the temperature on the sensor. Under equilibrium condition, the total heat generated will eventually dissipate to the environment. Thus the part of the heat flowing through the beams of the heater is

$$Q_h = K_h \Delta T_h \tag{6.1}$$

where Q_h is the heat flowing through the beams of the heater to the environment, K_h is the total thermal conductance of the beams connected to the heater, and ΔT_h is the temperature difference between the heater pad and the environment.

The other part of the heat flowing through the sample eventually dissipates to the environment via the beams of the sensor;

$$Q_s = K_{sample}(\Delta T_h - \Delta T_s) = K_s \Delta T_s \tag{6.2}$$

where Q_s is the heat flowing through the beams on the sensor to the environment, K_h is the total thermal conductance of the beams connected to the sensor, ΔT_s is the

temperature difference between the heater pad and the environment, and K_{sample} is the thermal conductance of the sample.

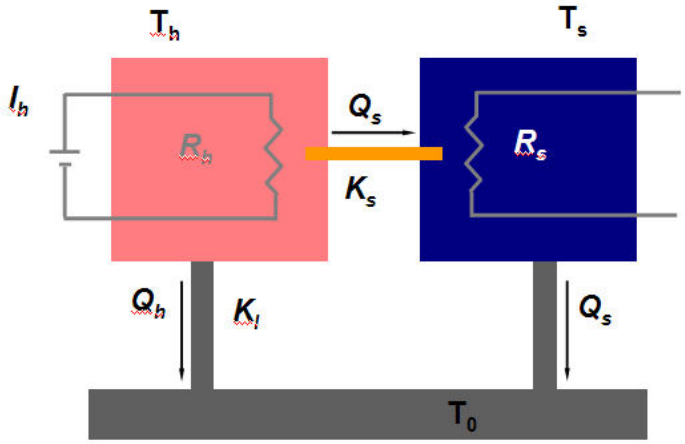

Figure 6-6 Schematic diagram of heat flow of the thermal device.

From conservation of energy, we have

$$P = Q_h + Q_s = K_h \Delta T_h + K_s \Delta T_s \tag{6.3}$$

Assuming that the heater and the sensor pads are symmetric, ie. K_h=K_s, the heat that flows through the sample is

$$Q_{sample} = Q_s = P \frac{\Delta T_s}{\Delta T_h + \Delta T_s} \tag{6.4}$$

Thus the thermal conductance of the sample can be determined to be

$$K_{sample} = \frac{P}{\Delta T_h - \Delta T_s} \left(\frac{\Delta T_s}{\Delta T_h + \Delta T_s} \right) \tag{6.5}$$

It is important to note the resistance used for calculating the power $P = I^2R$ should be the total resistance on the heating side, i.e. the summation of the resistance of the heater pad and the beams. The linear resistance vs. temperature (R vs. T) relation of the Pt film

resistors (Fig. 6-7) enables us to measure the temperature changes of the heater and sensor pads. The thermal conductivity κ can then be evaluated by incorporating the nanotube length and the annular area between inner and outer nanotube radius, as determined from TEM imaging.

6.4 Measurement sensitivity

The sensitivity of the measurement affects the determination of ΔT_h, ΔT_s, and the P in Eq. (6.5). I now discuss them as follows.

Voltage meter sensitivity: I use two HP34401A multimeters to measure the voltage drop on the heater and sensor. Generally, the voltage fluctuation is ±50nV.

Current source sensitivity: I use Keithley 263 and Keithley 220 current source to supply dc current to the heater and sensor. In the source range of 100μA, the accuracy is ~1nA.

R vs. T slope. It is used when converting resistance changes of the heater and sensor into temperature changes. In general, the error introduced by the R vs. T slope is less than 1%. However, as shown in Fig. 6-7, the linear R vs. T relation breaks down for T < 20K. At ~15K, the resistance saturates due to impurity or vacancy scattering. Thus the device only works for T > 15K.

The temperature resolution. The bath temperature is controlled by a Lakeshore 340 temperature controller. If the system's bath temperature is not stable, it gives jumps in the $\kappa(T)$ curve. Although it takes long time to gain the experience for tuning the PID parameters, once it is set, the temperature fluctuation is less than 10mK for T > 60K and less than 5mK for T < 60K.

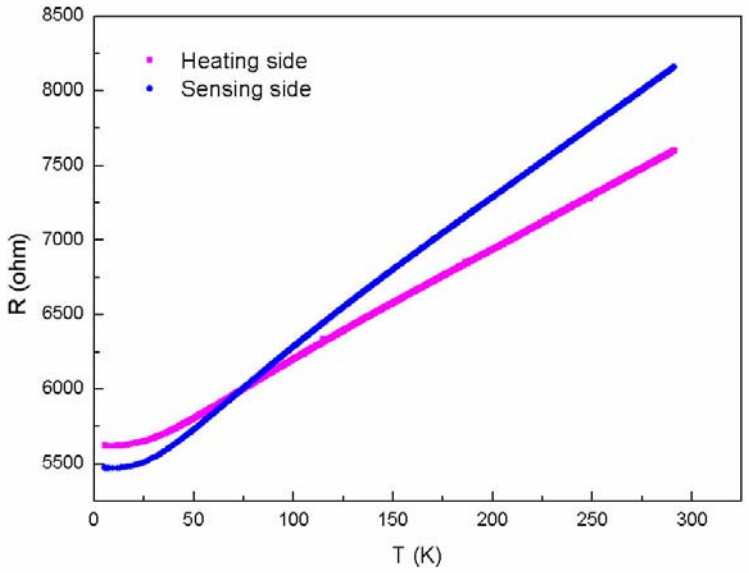

Figure 6-7 Temperature dependence resistance of Pt film electrodes on the sensor and heater

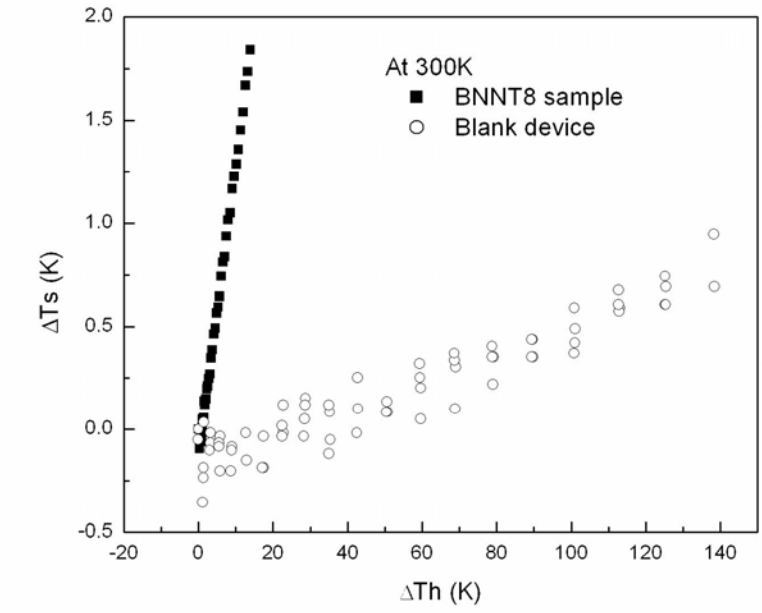

Figure 6-8 ΔT_h vs. ΔT_s of a blank device and a device with a BNNT on it.

A blank device (with no nanotube present) is also used to determine the background heat leakage. Figure 6-8 shows the relation of the ΔT_h vs. ΔT_s of a blank device and a device with a BNNT on it. The background gives an equivalent thermal conductance 2.8×10^{-12}W/K at room temperature, which is slightly larger than Li Shi's estimate [98]. However, as I will discuss below, the errors due to radiation loss at room temperature are in the 10^{-10} W/K range. Thus for thermal conductance of the sample below 10^{-10}W/K, a more complex analysis is needed to precisely determine the experimental result.

6.5 Measurement errors

Several factors introduce errors to the measurement.

Air convection. One measurement error is due to heat loss via air convection. The heat loss due to air convection can give an equivalent thermal conductance K_{air}. It follows that $K_{air} = \kappa_{air}A_{eq}/D_{eq}$, where κ_{air} is the thermal conductivity of the residual air molecules in the evacuated cryostat, A_{eq} is the equivalent surface area of the membrane, and D_{eq} is the equivalent distance between the heater and sensor. For a vacuum pressure less than 10^{-5} torr, the mean free path of air molecules is more than 1m and is much larger than D_{eq}. Under such condition, the heat loss due to air convection follows $\kappa_{air}=C_{air}vD_{eq}/3$, so

$$K_{air} = \frac{CvA_{eq}}{3} \tag{6.6}$$

where C_{air} is the heat capacity of air molecules, v is the velocity of air molecules. From Eq. (6.6), it can be estimated the effective thermal conductance due to air convection is less than 10^{-12}W/K at 300K, well below the measurement sensitivity.

Experimentally, I have measured the thermal conductance due to air convection by varying the vacuum pressure. No apparent heat loss via air convection is observed when the vacuum pressure is below 10^{-4} torr. Since the vacuum pressure is always kept below 5×10^{-6} torr, the systematic error due to air convection is negligible.

Radiation loss. The heat loss due to radiation can be estimated as

$$P_{rad} = 4\varepsilon\sigma A_{eq}(T_h^4 - T_s^4) \tag{6.7}$$

where $\sigma = 5.7\times10^{-8}$ W/m^{2}K^4, ε is the object's emissivity, and A_{eq} is the equivalent surface area between the heater and sensor. Li Shi gave an estimate of A_{eq} to be 12μm^2. It will give an equivalent thermal conductance less than $K_{rad} \sim 7\times10^{-11}$W/K at 300K. The error due to radiation becomes larger when measuring samples of low thermal conductance. Because a large heating power is always needed to obtain a detectable signal on the sensor, K_{rad} is larger than 7×10^{-11}W/K at 300K.

Temperature distribution along the heater beam. Because the temperature distribution is not uniform throughout the heater beams, strictly speaking, Eq. (6.5) only holds for small ΔT_h. For a typical sample with 10^{-8}W/K and $\Delta T_h \sim 10$K, the error in using Eq. (6.5) is ~13%.

Asymmetry. The error due to asymmetry of the heater and sensor was overlooked in earlier experiments using the same devices. In fact, the error due to the asymmetry is

large and can not be neglected. When deriving Eq. (6.5), I have assumed that the heater and sensor are symmetric, ie. $K_h = K_s$. In practice, they are not perfectly symmetric, so I need to introduce an asymmetric factor ε, so that $K_h = K_s(1+\varepsilon)$. The asymmetry will results in an asymmetry of temperature changes when switching the heater and sensor sides. It follows that

$$\varepsilon = \frac{\Delta T_s^{'} - \Delta T_s}{\Delta T_s} \tag{6.8}$$

where ΔT_s is the temperature change on the sensor when applying currents on the heater, as defined earlier. After switching the role of heater and sensor, $\Delta T_s^{'}$ is the temperature change on the new "sensor" when the heating current flows on the old "sensor". So the asymmetry of the temperature changes on the sensors can be used for measuring the asymmetry of K_h and K_s. I find ε to be around 10%, so there can be a 10% error in determining the sample thermal conductance.

Sample geometry. In previous experiment, Phillip Kim *et al.* used SEM imaging to determine the diameter of the nanotube to be 14±2nm [85]. But considering the resolution of SEM and the additional charging effect when imaging a CNT, it is actually difficult to achieve such a high accuracy. For example, figure 6-9 shows two SEM images obtained by Dr. Marky Llaguno in the Majumdar's group using a Joel SEM in Berkeley's Microlab. Although there are several CNTs bridging across the electrode, they are barely visible. I took the TEM image of the same device and found that they are MWCNTs with diameters of 20nm. Thus using SEM images to determine the diameter of a MWCNT can cause large errors. Another experiment even used an SEM image to

estimate the inner diameter of a CNT without considering that the electron beam size is much larger than that [86]. I believe that these methods all introduced very large errors in determining the geometrical factors of nanotubes. Making the device TEM accessible greatly reduces the error due to sample geometry. The resolution of a TEM is better than 1Å so that error due to geometrical factors becomes negligible.

Contact thermal resistance. It was recognized in previous experiments that the contribution of the contact thermal resistance is difficult to evaluate. A common approach is minimizing its contribution by annealing the contacts. But the value of the contact thermal resistance is still unknown. I will show a better method to estimate the contact resistance in chapter 12. Generally, for a nanotube with thermal conductance in the 10^{-8}W/K range, the contact thermal resistance contribution is less than 7% of the total thermal resistance.

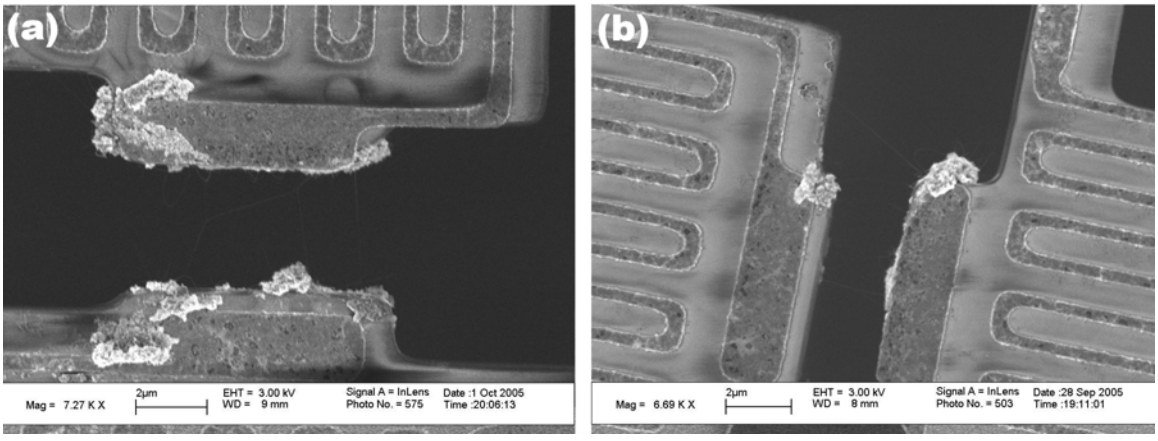

Figure 6-9(a) and (b) SEM images of two as-grown CNT devices made by Marky Llaguno using a Joel SEM in the Microlab at UC Berkeley.

6.6 AC method

In the earlier section, I introduced a dc-method to measure the thermal conductivity of individual nanotubes. In principle, an ac-method will also work for such measurements. Basically, a function generator with frequency ω is used to supply current to the heater. Due to Joule heating $P=I^2R$, the temperature will fluctuate at a frequency of 2ω. Correspondingly, if a dc-current is supplied to the sensor, its resistance will fluctuate at a frequency of 2ω. So the resistance change at the sensor can be determined by a lock-in amplifier locking at the frequency of 2ω.

This method is reminiscent of the 3ω method commonly used for measuring thermal conductivity of thin films. But it has several advantages over the 3ω method. In practice, a function generator sourcing a signal of $\sin\omega t$ also generates higher harmonics, 2ω, 3ω, etc. Although one can use low-pass filters to reduce these unwanted signals, they become an annoying source of error when the detection level is much lower than the output voltage. Actually, people who use the 3ω method always build a Wheaston bridge to balance out the unwanted signals. The method I used here separates the heating and sensing channel, thus eliminating the problem. In addition, the sensing signal level of the lock-in amplifier scales with the dc current of the sensor. Thus it is easy to increase the detection level without over-heating the heater.

The thermal conductance of the sample can be obtained using Eq. (6.5):

$$K_{sample} = \frac{P}{\Delta T_h - \Delta T_s}\left(\frac{\Delta T_s}{\Delta T_h + \Delta T_s}\right)$$

But now ΔT_h and ΔT_s are obtained by employing lock-in amplifiers to lock frequencies of ω at the heater and 2ω at the sensor.

Figure 6-11 shows the results of $\kappa(T)$ of a BNNT obtained by employing dc and ac methods. The overlap of the two curves demonstrates that both methods give consistent results.

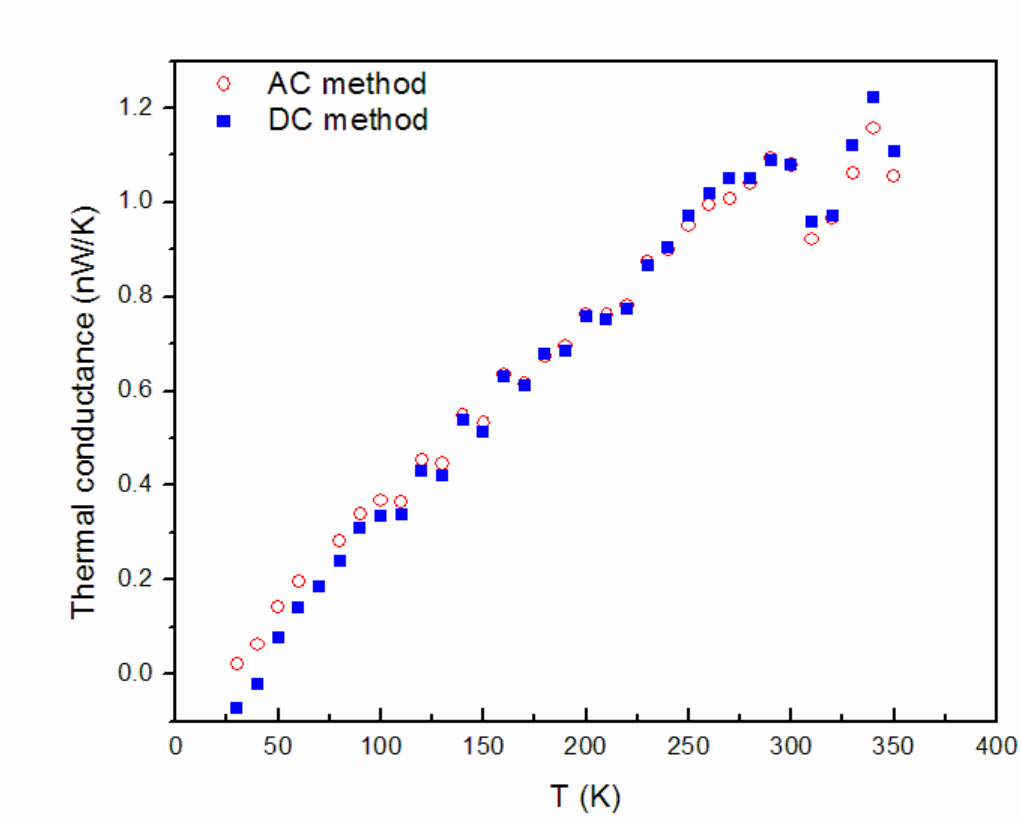

Figure 6-10 Thermal conductance of a BNNT measured by DC (solid squares) and AC (open circles) method.

6.7 Improvements

The thermal devices that I used in this thesis were made by Deyu Li in the Majumdar group. Fabrication of the thermal device involves a lot of procedures, including repeated patterning, aligning, photo-lithography, thin-film deposition, and etching. So when designing a new thermal device, it is desired to simplify the fabrication procedures and at the same time improve its flexibility and sensitivity. In principle, the simplest thermal device can be made by a single suspended beam. One only needs to compare the heat loss before and after connecting the sample to the device, and the sample thermal conductance can be extracted by a self-heating-self-sensing method. In fact, researchers have used this method to construct a scanning thermal microscope that can measure the temperature profile of a diamond's surface [99].

Renkun Chen in the Majumdar group and I designed a new device that not only greatly simplified the fabrication procedure but also improved the sensitivity of the device. Figure 6-11 shows our design. It consists of two suspended beams; one is a heater and the other one is a sensor. There is a large pad at the center part of the beam for connecting samples. The beam is made by 200nm thick, 800μm long SiN_x film. Because of the reduction of the total beam number and the thickness of SiN_x, the sensitivity is improved by a factor of ~6, reaching ~10^{-11} W/K at room temperature. The device can be TEM-transparent and is also suitable for bending/telescoping experiments which I will describe in later chapters. The thin film resistors can be made from other metals/alloys so that the device has the ability to measure thermal conductivity of a material below 15K.

The small gap between the center pads and the large gap between the beams also make sample preparation (like solution-deposition of SiNWs on the device) much easier.

One of the disadvantages of the new device is that it has no independent beam for measuring thermopower of a sample. Another disadvantage is that for conductive samples, one needs to be cautious so that no current flows through the sample when applying current to the heater. It can be solved by connecting a large resistor at the sensor. With a higher sensitivity thermal device, we will be able to approach the quantum limit of thermal conductance of nano-scale materials.

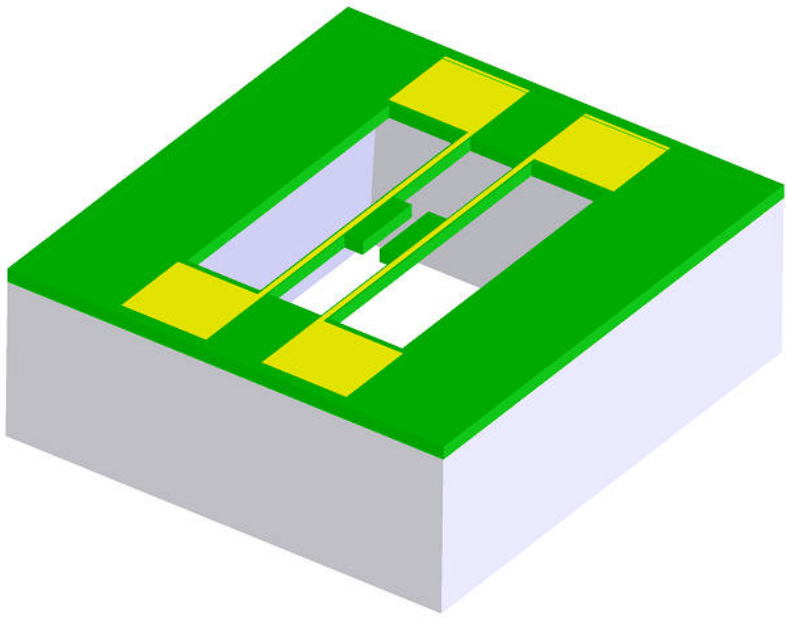

Figure 6-11 An improved design of the thermal device (not to scale).

Chapter 7 Thermal transport measurements on individual nanotubes

7.1 Temperature dependence and structures of boron nitride nanotubes

The behavior of $\kappa(T)$ of nanotubes is of fundamental interest. Theoretical calculations on CNTs have suggested that the onset of umklapp processes (T_U), which denote the occurrence of phonon-phonon back-scatterings, should appear at 100~400K [39,78,79,100]. Experimentally, J. Hone *et al.* studied the $\kappa(T)$ of mats of SWCNTs and found that $\kappa(T)$ increases almost linearly with increasing temperature up to 350K [82]. Similar results were observed for mats of MWCNTs. P. Kim *et al.* studied $\kappa(T)$ of an individual MWCNT and found that $\kappa(T)$ of an isolated *bundle* of CNTs increases monotonically with increasing temperature while $\kappa(T)$ of the individual MWCNT shows a peak at 350K [85]. The Dai group used an indirect method based on fitting the

nonlinear I-V curve of a CNT and extracted the $\kappa(T)$ at high temperatures [88]. They found that $T_U \sim 400K$ for a SWCNT.

For BNNTs, theoretical calculations suggest that their T_U should be similar to that of CNTs, ie. varying from 120K to 400K [59,101]. However, although κ for hexagonal BN shows a peak at 120K, my measurements on mats of B-C-N nanotubes and BNNTs only display a change in slope at 120K. The discrepancies between theoretical predictions and experimental results are still not clear. Here I will describe experimental results on $\kappa(T)$ of individual multiwall BNNTs.

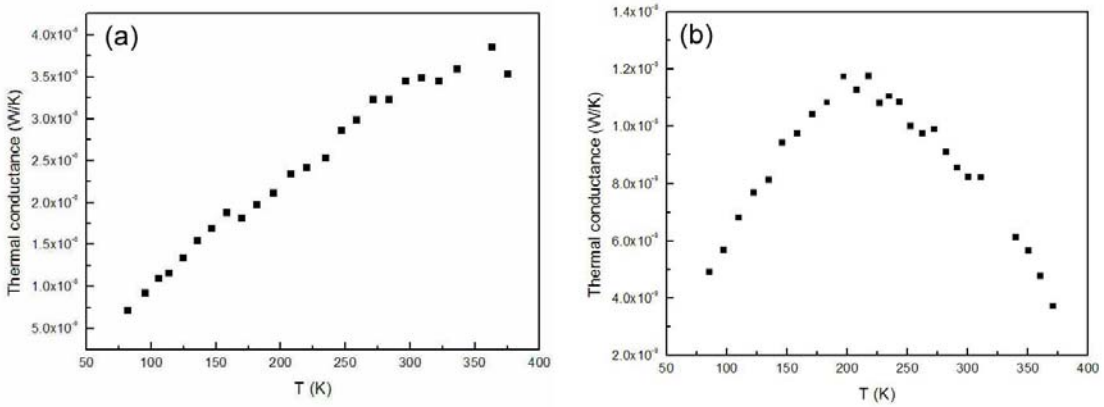

Figure 7-1 Temperature dependent thermal conductance of two BNNTs showing two distinct behaviors. (a) shows monotonic increasing thermal conductance with increasing temperature. (b) displays a peak indicating the onset of umklapp processes.

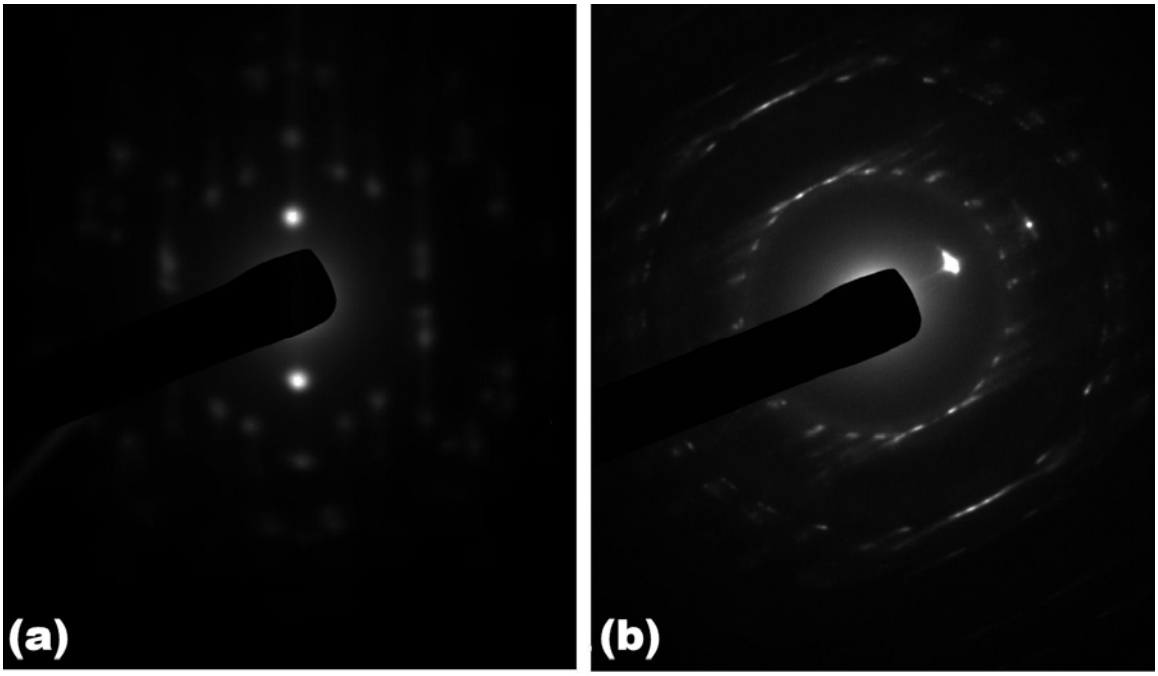

Figure 7-2 Representative diffraction patterns of BNNTs. One of them shows zigzag structure (a). The other one shows a mixed structures of armchair and zigzag (b).

Two distinct temperature dependencies of $\kappa(T)$ are observed for over 20 individual BNNT samples. As shown in Fig. 7-1(a), the first kind of $\kappa(T)$ behavior shows a monotonic increase of thermal conductivity with increasing temperature. In contrast, the second kind of $\kappa(T)$ curve displays a peak at 200K (Fig. 7-1(b)), suggesting the onset of umklapp processes. However, eighteen samples show monotonic increase in $\kappa(T)$ while only two of them display a peak. For CVD-synthesized BNNTs, it has been shown that 80% of the samples exhibit zigzag structures and only 20% of them show mixed structures [102]. From the population point of view, it is suggestive that there might be a correlation between the behavior of $\kappa(T)$ and BNNT structures. However, after

comparing the diffraction patterns of each BNNT with their $\kappa(T)$, no clear correlations are established. Indeed, some of the BNNTs whose $\kappa(T)$ increases monotonically exhibit zigzag structures. However, some of them also display diffraction patterns of mixed structures. So the effort to try to correlate $\kappa(T)$ behavior of BNNTs with their diffraction patterns is not successful.

Although the correlation between BNNT structure and $\kappa(T)$ behavior is not established, the observation of a peak on some $\kappa(T)$ curves demonstrates the presence of umklapp process in BNNTs. Notably, the peak in $\kappa(T)$ occurs at T_U~200K, which is higher than that of hexagonal BN. For $\kappa(T)$ displaying monotonically increasing, their T_U's are probably higher than 350K. The wide distribution of the T_U's may be due to structural differences in the nanotubes. More detailed studies are needed to establish the correlation between BNNT structure and $\kappa(T)$ behavior.

7.2 Thermopower of carbon nanotubes

The thermopower of CNT mats has been investigated by former Zettl group members [75,103,104]. One of the most important discoveries is that the thermopower of CNTs is sensitive to the presence of oxygen [75,103]. When measuring the thermopower of as-prepared CNTs, the thermopower showed positive values. After baking the sample in vacuum, the thermopower became negative. Thermopower measurements of individual MWCNTs were first carried out by P. Kim *et al.* [105]. At that time, they were not aware of the oxygen-absorption effect and their thermopower showed positive values.

Although some of the MWCNT samples did show negative thermopower values at room temperature, temperature dependence of thermopower was successfully measured on only one MWCNT device (shown in Fig. 7-3). The MWCNT has an outer diameter of 9.6nm and an inner diameter of 7.2nm. At room temperature, the thermopower remained positive after pumping in vacuum for a long time. It is not clear why continuous pumping did not change the thermopower value. It is possible that the coating of $C_9H_{16}Pt$ molecules prohibits the desorption of oxygen molecules or that $C_9H_{16}Pt$ functionalizes the surface and thus effectively dope the MWCNT, keeping the thermopower value positive. Notably, the value of the thermopower is low, in the range of μV/K, which is comparable to the typical thermopower of a metal.

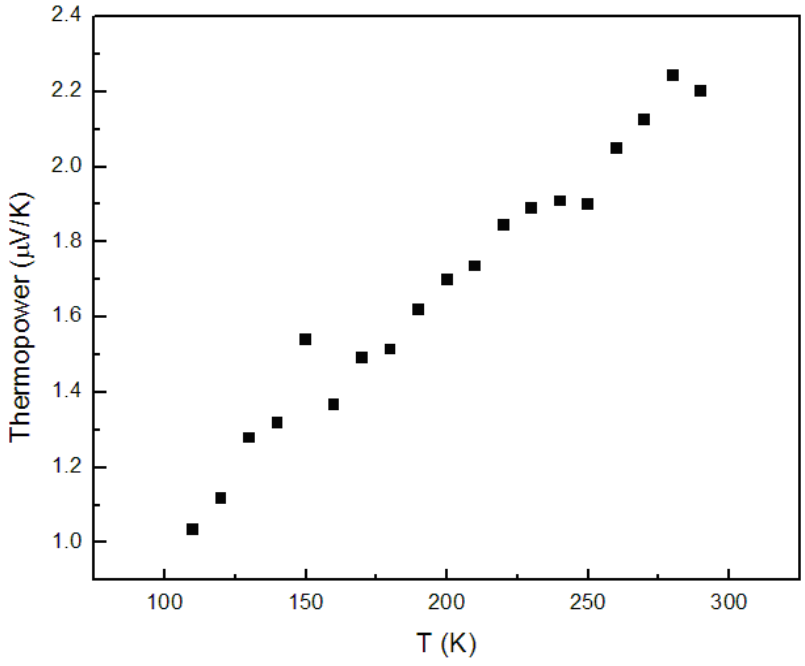

Figure 7-3 Temperature dependence of thermopower of individual carbon nanotube.

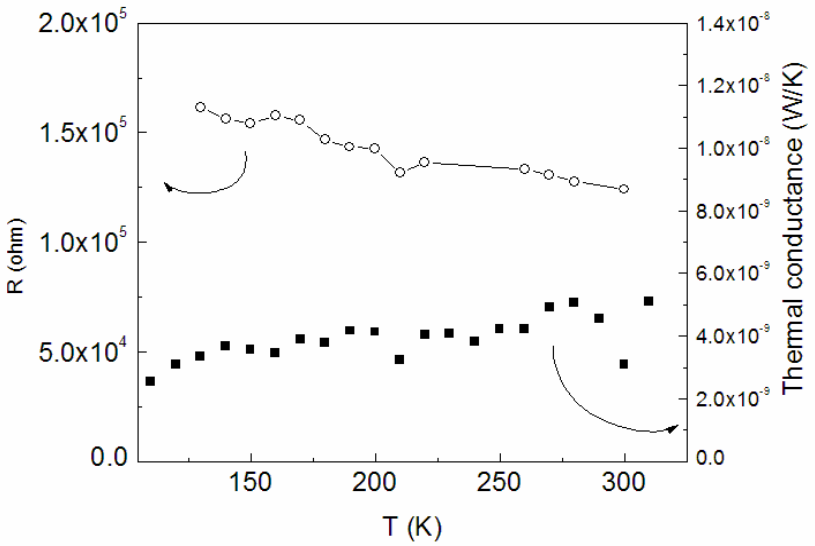

Figure 7-4 Temperature dependence of resistance and thermal conductance of the MWCNT device shown in Fig. 7-3.

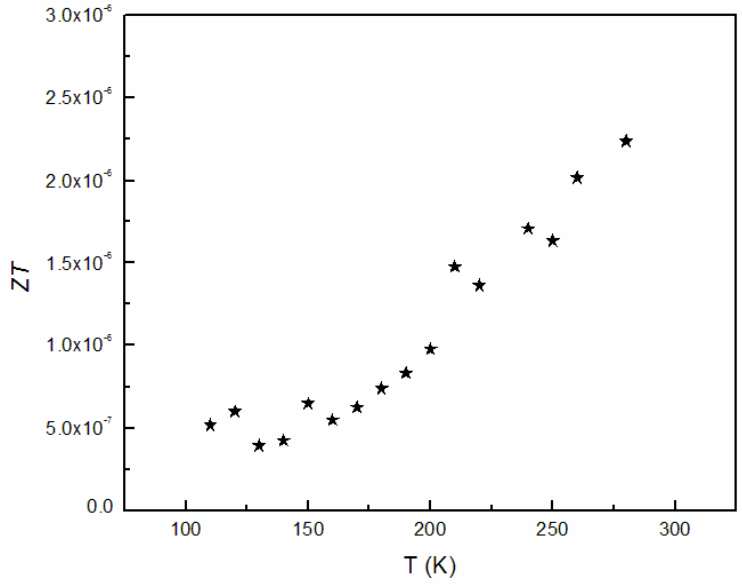

Figure 7-5 Figure of merit (*ZT*) of the MWCNT obtained from Fig. 7-3 and Fig. 7-4.

It is interesting to see whether MWCNTs can be used as thermoelectric refrigerators. To evaluate the possibility, it is important to determine the figure of merit (*ZT*), defined as:

$$ZT = \frac{S^2 T}{\rho\kappa} = \frac{S^2 T}{RK} \tag{7.1}$$

where S is the thermopower measured in μV/K, ρ is the electrical resistivity, R is the resistance. A material exhibiting $ZT > 2$ will be of commercial interest, $ZT > 3$ will have efficiency competing with that of an ordinary refrigerator. Figure 7-4 shows the temperature dependence of resistance and thermal conductance of the MWCNT. The corresponding *ZT* behavior is plotted in Fig. 7-5. The *ZT* of the MWCNT is very small. The result is consistent with Li Shi *et al.*'s earlier report [98].

Chapter 8 Isotope effects on the thermal conductivity of boron-nitride nanotubes

8.1 Phonon scattering from point defects

A phenomenological model on the effect of point defect scattering on the thermal conductivity of materials, sometimes refers to as Klemens-Callaway model, can be derived from a perturbative approach on the Hamiltonian for lattice vibrations of a crystal:

$$H = \sum_{j=1}^{N} \frac{\hat{p}_j^2}{2M} + \frac{1}{2} \sum_{jl} \sum_{\alpha\beta} \hat{u}_{j\alpha} \Phi_{\alpha\beta}(R_j - R_k) u_{k\beta}^{\dagger} + \sum_j \sum_l \frac{\Delta M_l}{M} \frac{p_j^2}{2M} \tag{8.1}$$

with local atomic mass M, Φ the interactions between atoms, and ΔM is the mass deficit associated with the lattice atoms of mass M. The scattering due to the last term causes phonons to transit from an initial state to a final state. According to Fermi's golden rule:

$$\Gamma_{i \to f} = \frac{2\pi}{\hbar} \left| \langle f | \Delta \hat{H} | i \rangle \right|^2 \delta(E_f - E_i) \tag{8.2}$$

The transition rate for phonon scattering then can be evaluated as:

$$\Gamma_{i\to f} = \frac{\pi\hbar\Delta M_l^2}{6N^2M^2}\omega_{qn}^2 \times V\int d\omega_{q'n'} D(\omega_{q'n'})\left(\frac{1}{e^{\beta\hbar\omega_{q'n'}}-1}+1\right)\delta(E_f - E_i) = \frac{\pi V\Delta M_l^2}{6N^2M^2}\omega_{qn}^2\frac{D(\omega_{qn})}{1-e^{\beta\hbar\omega_{qn}}} \tag{8.3}$$

At low temperatures, we can use the Debye form for the density of states

$$D(\omega) = \frac{3}{2\pi^2 v^3}\omega^2 \tag{8.4}$$

and summing over all scattering sites, with fractional density c_i. The phonon relaxation time can be determined to be

$$\frac{1}{\tau} = \Gamma = \frac{c_i a^3\omega^4}{4\pi v^3}\frac{1}{1-e^{-\beta\hbar\omega}}\left(\frac{\Delta M}{M}\right)^2 \tag{8.5}$$

At very low temperatures $k_BT<<\hbar\omega$, the phonon relaxation time approaches:

$$\frac{1}{\tau} = \frac{c_i a^3\omega^4}{4\pi v^3}\left(\frac{\Delta M}{M}\right)^2 \tag{8.6}$$

As expected, the ω^4 is similar to the Rayleigh scattering of light where the wavelength is much larger than the scattering center.

As can be seen in the derivation, Klemens-Callaway model only applies for low temperature when phonon-phonon scatterings are negligible. At high temperatures, the phonon transport becomes complicated and many of the approximations do not hold anymore. However, the proportionality of the scattering rate to $(\Delta M/M)^2$ still holds even at high temperatures. Thus the Klemens-Callaway model is still useful for analyzing experimental data at high temperatures.

8.2 Isotope effect on boron-nitride nanotubes

Isotope effect on the κ of materials is of fundamental interest. Table 8-1 summarizes the isotope effect on the κ(290K) of various materials. The κ isotope effect, large in bulk diamond [106], silicon [107], and germanium [108], remains unexplored for low-dimensional systems. Boron has larger natural isotopic disorder (19.9% ^{10}B and 80.1% ^{11}B) than does carbon (98.9% ^{12}C and 1.1% ^{13}C), suggesting that an enhancement of κ due to isotope-enrichment could be large in BNNTs.

Table 8-1 Isotope effect on the room temperature thermal conductivity of various materials.

Material	**Nature isotope abundance**	**Thermal conductivity enhancement factor at room temperature**
Diamond	(98.9% ^{12}C, 1.1% ^{13}C)	35%
Germanium	(20.52% ^{70}Ge, 27.43% ^{71}Ge, 7.76% ^{72}Ge, 36.54% ^{74}Ge, 7.76% ^{76}Ge)	30%
GaAs	(60.2% ^{69}Ga, 39.8% ^{71}Ga)	5%
Si	(92.2% ^{28}Si, 4.7% ^{29}Si, 3.1% ^{30}Si)	10%
BNNT	(18.98% ^{10}B, 81.02% ^{11}B)	**50% (this work)**
Cubic BN	(18.98% ^{10}B, 81.02% ^{11}B)	125% (theory)

Controlled isotope concentration of multiwall BNNTs were synthesized by David Okawa. BNNT samples have typical outer diameter 30~40nm and length ~10μm. Isotopic percentages were controlled using commercially available boron isotopes (99.56% ^{11}B, Cambridge Isotope Laboratories, Inc.)[i]. CNTs with diameters ranging from 10nm to 33nm were prepared by Henry Garcia using conventional arc methods.

Fig. 8-1 shows κ(T) for an isotopically impure (natural abundance) BNNT, an isotopically pure ^{11}BN nanotube, and a CNT, all with similar outer diameters. For all materials, κ increases with increasing temperature with no sign of saturation up to 300~350K. Isotopic enrichment is seen to have a dramatic effect on the thermal conductivity of BNNTs, with an enhancement of approximately 50% throughout the measured temperature range. Furthermore, the overlap of the data sets for the isotopically enriched BNNT and CNT is striking; it reveals similarities of the intrinsic phonon dispersion relations, and demonstrates that the thermal conductivity of an isotopically pure BNNT is virtually identical to that of a CNT. These results are consistent with theoretical calculations that suggest similar phonon dispersion relations between hexagonal BN and graphene.

[i] The isotope disorder of nitrogen is much smaller (<0.4%) and can be neglected here.

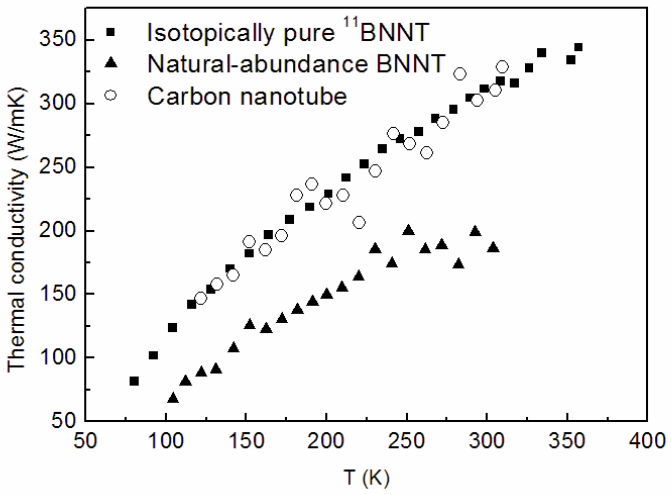

Figure 8-1 The κ(T) of a CNT (open circle), a BNNT (solid triangle) and an isotopically pure BNNT (solid square) with similar outer diameters.

8.3 Diameter dependence

Previous experiments on CNTs suggest that the thermal conductivity may depend strongly on nanotube outer diameter. To verify this effect for CNTs and to investigate it for BNNTs, I have systematically measured κ(290K) for BNNTs and CNTs with different diameters. As shown in Fig. 8-2, for BNNTs in the range 30nm~40nm κ increases with decreasing outer diameter. A similar diameter-dependence is also observed for CNTs, measured over the broader diameter range 33nm to 10nm. For large outer diameter (d_{out} ~ 35nm) CNTs κ ~ 300W/mK, while for small outer diameter (d_{out} ~ 10nm) CNTs κ ~ 1100W/mK. My observed diameter-dependence of κ is qualitatively similar to, though less pronounced, that reported in Ref. [87]. The origin of this diameter dependence is unclear. It has been suggested that, since in conventional thermal

conductivity experiments heat is injected from the contacts into the nanotube via the outermost shell and the coupling is much weaker along the c-axis than in the a-b plane of graphite or hexagonal BN, it is possible that the outermost shell dominates the thermal transport. However, when plotting the thermal *conductance* data with respect to $2\pi d_{out}$, I do not observe a clear correlation between them, making such a non-uniform heat flow explanation unlikely. Alternatively, theoretical studies have suggested that inter-layer phonon scattering can significantly reduce the thermal conductivity of graphite, and similar inter-shell scattering mechanisms might be expected for multiwall nanotubes. From TEM imaging I find that nanotubes with d_{out} ~10nm generally have ~10 shells, while nanotubes with d_{out} ~ 30~40nm generally have 60~90 shells. Thus the increasing shell number with increasing d_{out} supports the inter-shell scattering picture.

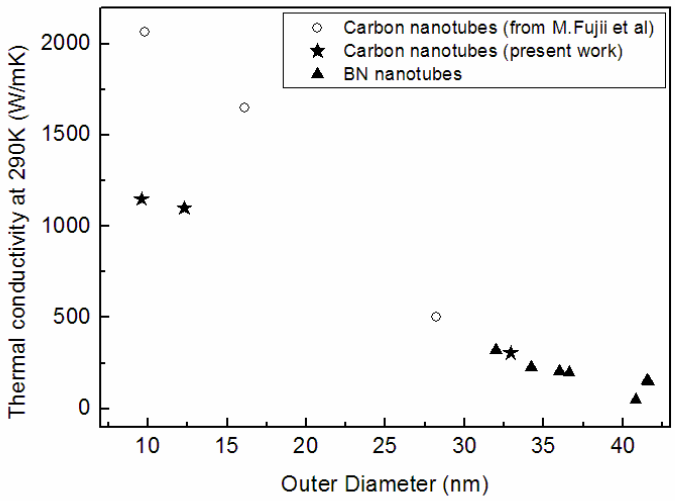

Figure 8-2 The κ(290K) vs. outer diameter of various BNNTs (solid triangles) and CNTs (solid stars). Data from Ref. [87] are also shown for comparison (open circles).

8.4 Discussion

The thermal conductivity can be used to estimate the phonon mean free path using the expression $\kappa(T)=\sum Cv\ell$, where C, v, and ℓ are respectively the specific heat, group velocity, and phonon mean-free-path, and the sum is over all phonon states. Since currently there are no available data for heat capacity of BNNTs, I assume the ratio of heat capacity of hexagonal BN to graphite to be the same as that of BNNTs to CNTs. Choosing v = 10km/s estimated by theory and following the diameter-dependence of κ in Fig. 8-2, I estimate that the room temperature phonon mean-free path would reach 200nm for isotopically pure BNNTs with diameter 10nm, comparable to ℓ = 500nm determined from previous experiments on an isolated CNT with a similar diameter.

The isotope enhancement factor of 50% for BNNTs, though dramatic, is smaller than might be anticipated from simple models. First, natural abundance boron has significantly greater isotopic disorder (19.9%) than natural abundance carbon (1.1%), yet the isotope enhancement experimentally observed for diamond is also 50%. Indeed, theoretical work has predicted that for cubic BN crystals, the isotopic enhancement should be 125%. Second, the one-dimensional structure of nanotubes should further increase the isotope enhancement factor by promoting phonon localization due to isotope scattering. Third, it has been suggested that the isotope effect can change the phonon scattering time (τ) by

$$\frac{1}{\tau}=\frac{c_i a^3 \omega^4}{4\pi v^3}\left(\frac{\Delta M}{M}\right)^2 \tag{8.7}$$

where ω is the frequency, v is the average sound velocity, ΔM is the mass deficit associated with the lattice atoms of mass M and atomic spacing a. Since ^{11}B is lighter than ^{12}C, the isotope enhancement factor of BNNTs may be expected to be larger than that of CNTs.

On the other hand, the observed strong diameter-dependence of κ may strongly influence the isotope enhancement factor. For large-diameter nanotubes with many walls, for which inter-shell phonon scattering dominates the phonon transport, isotopic disorder effects play only a secondary role and hence the isotope enhancement factor would be severely depressed. Only for small-diameter nanotubes with few walls, would the phonon mean-free-path be limited by isotope or impurity scattering along the nanotube axis. Thus, the isotope enhancement factor of 50% here observed for large-diameter BNNTs may well represent only a lower limit for BNNTs in general.

Chapter 9 Robust phonon transports in nanotubes

9.1 Robust against electron irradiation

The electrical current distribution of a MWCNT has been an interesting subject. Collins *et al.* used electrical breakdown method to remove the walls of sections of a MWCNT and found that each wall contributes equal amounts of current [109]. Tom Yuzvinsky *et al.* used a similar method with additional in-situ TEM imaging and concluded that current uniformly distributes across the entire cross section [110]. On the other hand, several experiments observed the Aharonov-Bohm effect in MWCNTs and demonstrated that the current only flows in the outer wall [111,112]. The origin of the controversy is still not clear, but it may suggest some interesting unknown phenomena. In contrast with electrical transport, so far no experiment has investigated the heat distribution of a multiwall nanotube. Previous thermal transport measurements of individual MWCNTs and BNNTs revealed an unusual diameter-dependence of thermal conductivity, suggesting that inter-wall scatterings limit the phonon mean free path [87]. However, they do not give information of how the heat flow is distributed along the radial direction of the nanotubes. To unravel the heat distribution of a multiwall

nanotube, here I experimentally measure the thermal conductivity change of a BNNT while cutting it using an electron beam.

Figure 9-1(a) and (b) show low-magnification TEM images of a BNNT (Sample 1) and a BNNT bundle (Sample 2) spanning the gap of the electrodes. The inset of Fig. 9-1(a) and (b) show the corresponding SEM images. In-situ thermal conductance measurement was done every two minutes while using the line-scan mode of the SEM to cut the BNNT. Precision cutting of MWCNTs using an electron beam has been demonstrated by Tom Yuzvinsky *et al.* [113]. Generally, they found that the cutting time does not necessarily increase with increasing electron acceleration voltage, but a higher current density definitely shortens the cutting time. Here I use an acceleration voltage of 2KV with beam currents 128pA and 615pA to cut Sample 1 and Sample 2, respectively.

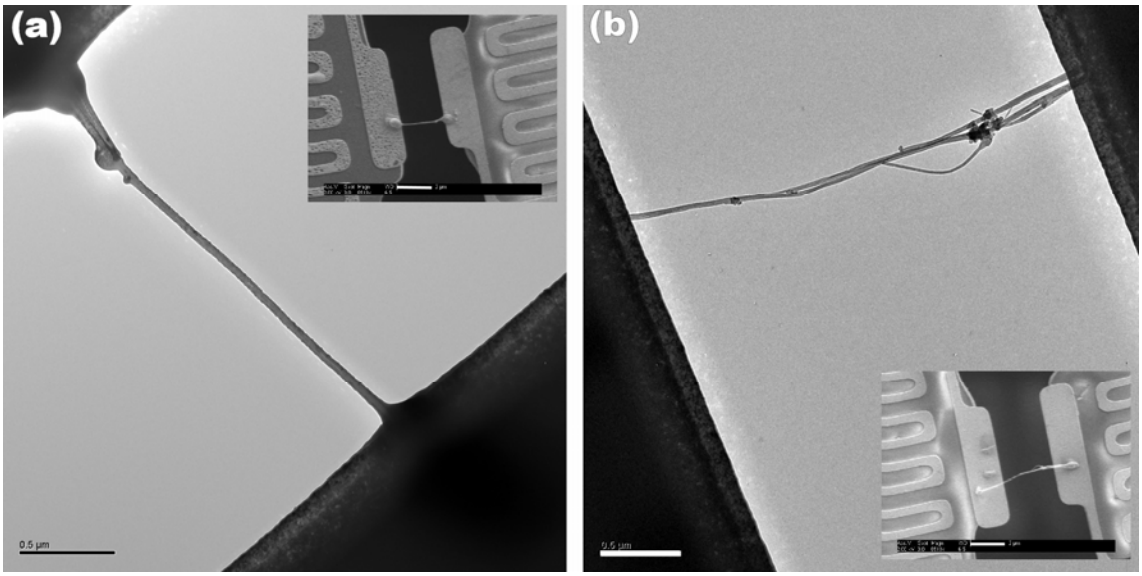

Figure 9-1 Low-magnification TEM images of two BNNTs on thermal devices (scale bar = 0.5μm). Insets show the corresponding SEM images (scale bar = 2μm).

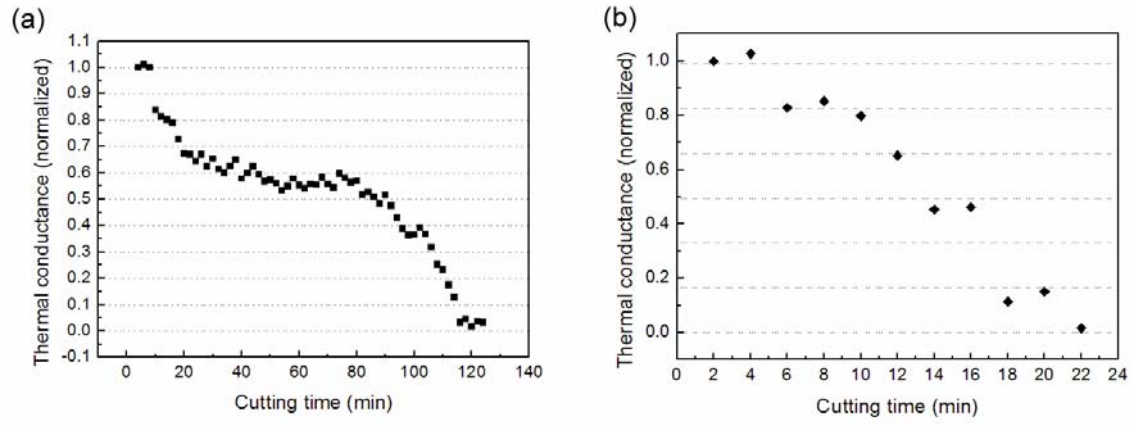

Figure 9-2. Thermal conductance vs. cutting time for Sample 1 and Sample 2.

The results of thermal conductance vs. cutting time of Sample 1 and Sample 2 are shown in Fig. 9-2(a) and (b), respectively. Surprisingly, despite that the electron beam constantly irradiates the BNNTs, the thermal conductance decreases step by step rather than continuously. Notably, the number of the steps does not equal to the number of walls of the BNNT. For example, Sample 1 has 68 walls but only six steps are observed in Fig. 9-2(a). For Sample 1, despite the initial drop, its thermal conductance remains nearly constant for a long time then shows step-like decrease. For sample 2, a larger beam current was used, thus the cutting time is much shorter than that of sample 1.

More interestingly, the thermal conductance change in each step is nearly the same for each case. Each step in Fig. 9-2(a) and (b) represents a decrease of thermal conductance of 4.7×10^{-8} W/K and 3×10^{-9} W/K, respectively. The result is similar to the electrical breakdown experiments in MWCNTs. However, unlike previous experiments on MWCNTs in which large sections of walls were burnt out, here the irradiation area is much smaller and localized. It is important to note that the thermal conductance

measurement resolution is much higher than the magnitude of each step so the results are not due to experimental artifacts.

Fig. 9-3 shows the results of the finite element analyses of a model simulating the cutting process. As expected, even if a large anisotropy of thermal conductance is introduced to the model, the thermal conductance still decreases continuously. Thus the thermal conductance of a continuous media will not show a step-like decrease if there is no corresponding step-like changes in the sample geometry.

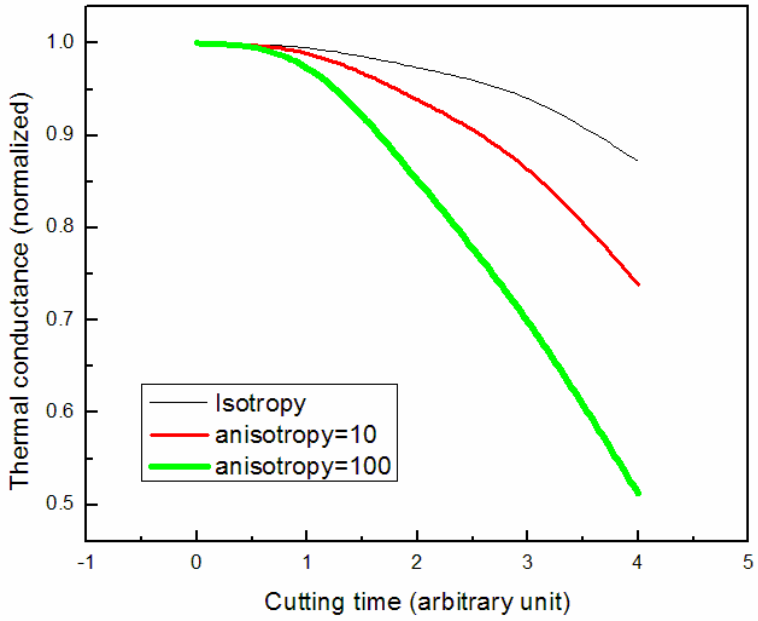

Figure 9-3. Results from finite element simulation of the cutting process. Different thermal conductivity anisotropy ratios (defined as the ratio of the thermal conductivity along the nanotube axis to that of the radial direction) are introduced. As expected, no step-like decrease can be observed in this continuum model.

To get more insight to the structural change of BNNTs under electron beam irradiation, I have done in-situ TEM imaging of BNNTs under 100KV electron beam irradiation. Figure 9-4(a) to (d) show a series of structural changes of a BNNT under intense electron beam irradiation. The walls of the BNNT were straight and regular at the beginning (Fig. 9-4(a)). After focusing the electron beam and irradiating the BNNT for 10mins, the outer and inner walls were damaged and became wavy (Fig 9-4(b)). After additional 5mins of irradiation, ~6 outer-walls were destroyed and an end cap was formed. Interestingly, end caps always form at the ends of 6~11 wall-structures, as shown in Fig. 9-4(c). Onion-like and fullerene-like structures were also observed after an extended period irradiation (Fig. 9-4(d)).

Since the formation of the end caps opens a gap and thus blocks the heat flow, it explains the sudden decrease of the thermal conductance. Besides, the fact that the end caps always form at 6~11 wall-structures also explain the number of steps in Fig. 9-2(a) and (b). For example, Sample 1 has 68 walls and thus there are (68/11)~6 steps in Fig. 9-2(a). The good agreement between the steps of thermal conductance and observed structural change suggests that the heat flow is uniformly distributed across the entire cross section. Furthermore, it is interesting to note that although the walls of the BNNT become wavy after irradiation, they do not affect the total thermal conductance. Thus the thermal conductance of BNNTs is not affected by the wavy structures induced by electron beam irradiation. We will see more clearly in the next section that the thermal conductance can endure severe structural distortion when bending the nanotubes.

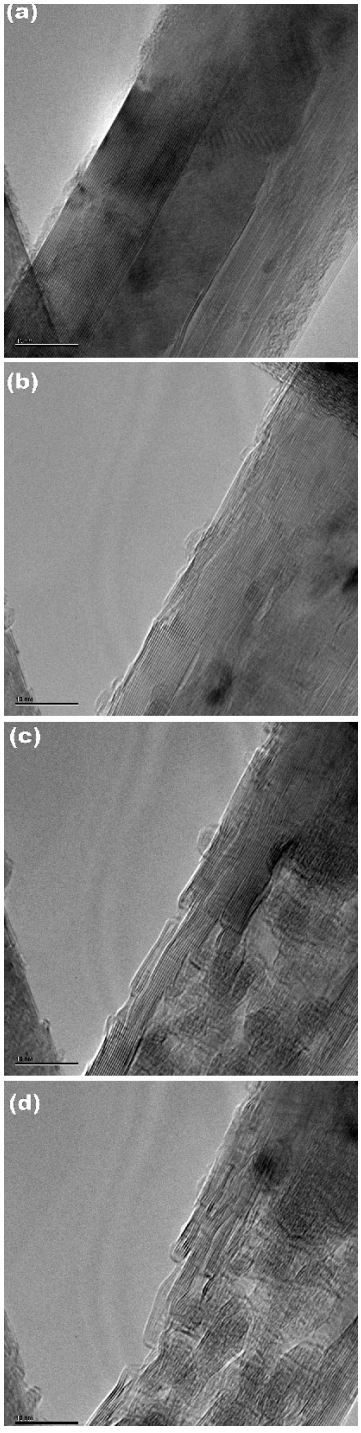

Figure 9-4. A time sequence of TEM images of a BNNT under intense electron beam irradiation.

In summary, I have observed step-like decrease of the thermal conductance of BNNTs when irradiating them with intense electron beams. TEM imaging of BNNTs under electron irradiation suggests that the formation of end caps containing 6~11 walls is responsible for the observed uniform step-like changes of thermal conductance. The results suggest that the heat flow is uniformly distributed across the entire cross section of the BNNT. Furthermore, the thermal conductance of BNNTs is insensitive to the wavy structures induced by electron beam irradiation. Electron beam induced structural defects are very common for ordinary materials and especially for biological samples. BNNTs are robust phonon waveguides which are insensitive to low-density electron irradiation so they can be an ideal protection layer for sensitive chemicals or biological molecules.

9.2 Robust against structural deformation

For in-situ bending vs. electrical/thermal measurement, a sharpened tungsten tip mounted on a pizeo-driven manipulator inside an SEM was used to push one of the resistance/thermopower beams near the end of the suspended device (shown in the Fig. 9-5). This would bend the nanotube but also minimize the heat loss through the tungsten tip. I have found that the heat loss through the tungsten tip is negligible. The resistance and thermopower can be measured simultaneously, with careful subtraction of the contribution of the Pt films. All the measurements were done at room temperature.

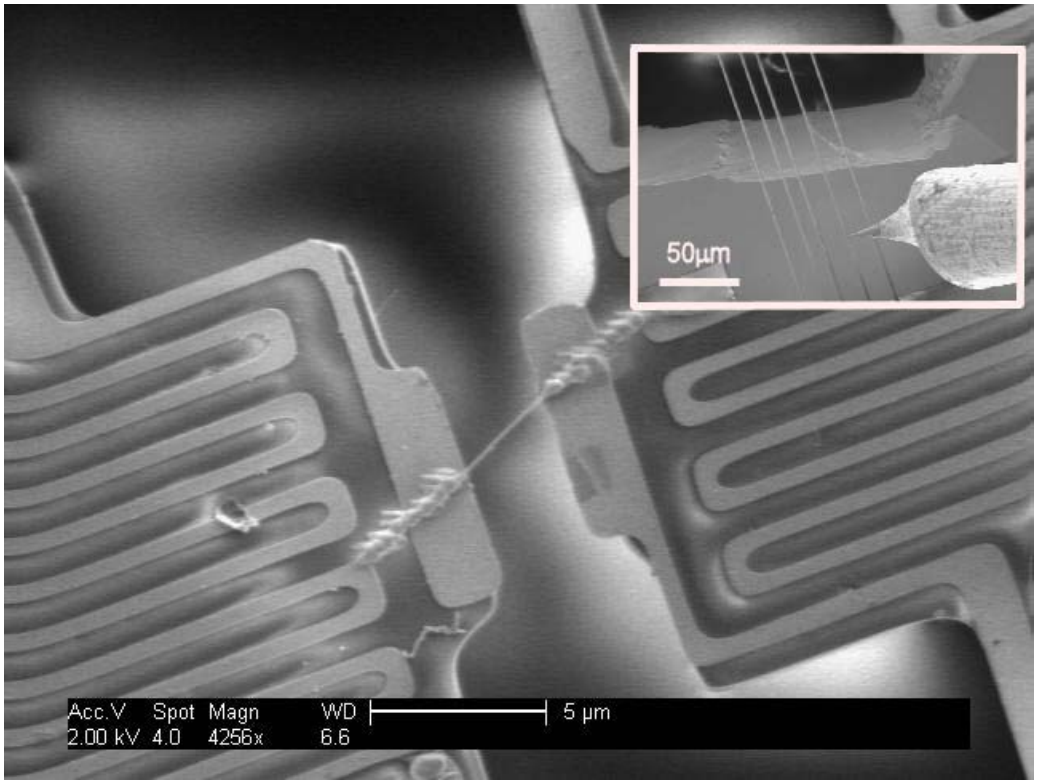

Figure 9-5 An SEM image of the microfabricated test fixture with a BNNT bonded with $C_9H_{16}Pt$ on the electrodes (scale bar = 5µm). The inset shows the experimental configuration when using the manipulator to push the device without affecting the heat profile (scale bar = 50µm).

The upper part of Fig. 9-6 shows a series of representative SEM images with two cyclic bendings of CNT sample 1. The corresponding changes of the electrical resistance, thermopower, and thermal conductivity are shown in the lower part of Fig. 9-6. Their values are normalized to the initial quantities of 44KΩ, -42µV/K, and 1050W/mK, respectively. The resistance shows a cyclic 20% modulation against deformation. It reaches maximum when the bending angle is largest, indicating a band-gap opening under deformation. Since the total conductance of a multiwall CNT is dominated by the

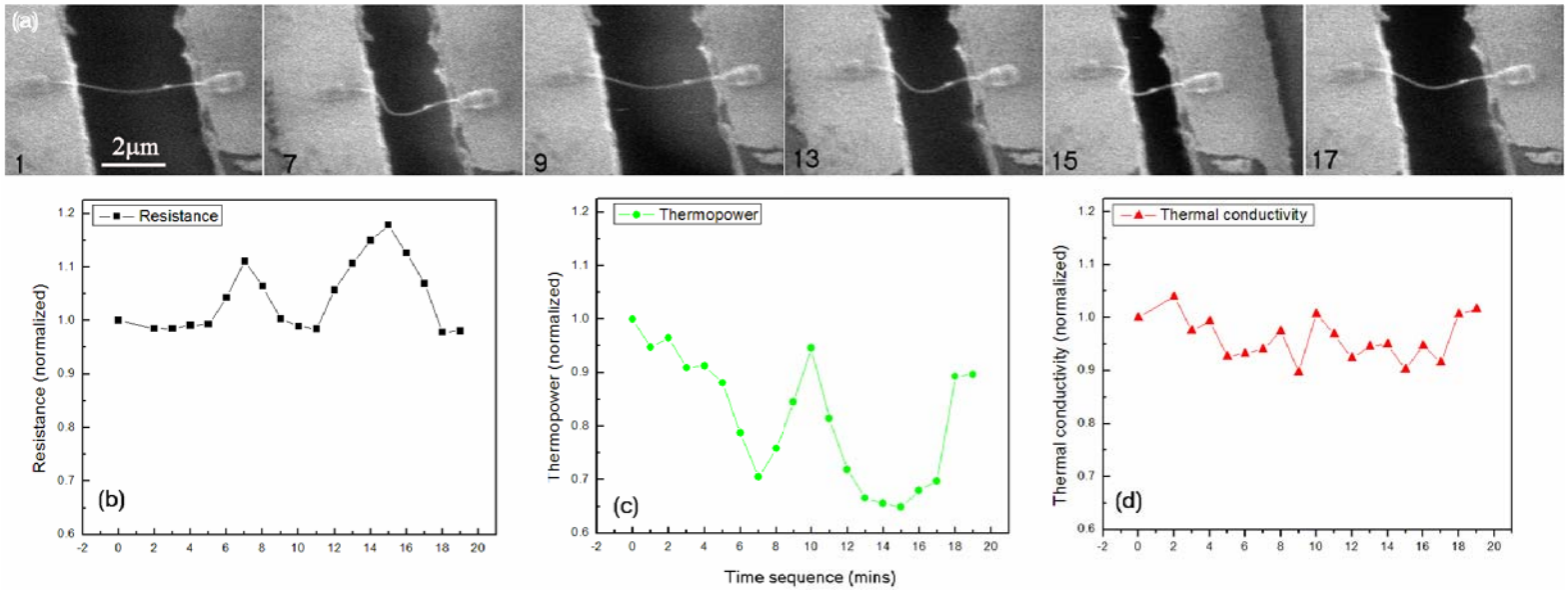

Figure 9-6(a) A series of representative SEM images of CNT sample 1 undergoing two cyclic bendings. The number in each frame denotes the time sequence number (scale bar = 2μm). (b) shows the resistance change, (c) shows the thermopower change, and (d) shows the thermal conductivity change with respect to time sequence.

metallic channels, Fig. 9-6(b) indicates that there is a metal to semiconducting transition when bending metallic tubes. The result is consistent with previous experiments [114]. It is also consistent with theoretical preditions that suggest a band-gap opening when bending metallic CNTs [115].

The total thermopower (S) of a multiwall CNT can be expressed by a two band model

$$S = \frac{G_{metal} S_{metal}}{G_{metal} + G_{semi}} + \frac{G_{semi} S_{semi}}{G_{metal} + G_{semi}} \tag{9.1}$$

where the G's are conductance of the metallic and semiconducting channels, respectively. And

$$\begin{aligned} S_{metal} &= \frac{-\pi^2 k_B^2 T}{3|e|} \frac{1}{G_{metal}} \frac{dG_{metal}}{dE}\bigg|_{E_F} \\ S_{semi} &= \frac{-k_B (c-1)}{|e|(c+1)} \left(\frac{E_G}{2k_B T} + 2 \right) \end{aligned} \tag{9.2}$$

where E_F is the Fermi energy, and c denotes the mobility ratio of electron bands to hole bands. For metallic channels we have nearly electron-hole symmetry, thus the first term in Eq. (9.1) vanishes [104]. So the total thermopower of a multiwall CNT is dominated by the semiconducting channels. As Eq. (9.2) suggests, a band-gap-closing will decrease the value of $|S_{semi}|$. Thus Fig. 9-6(c) indicates that there is a semiconducting to metal transition when bending a semiconducting CNT, which agrees with the theoretical predictions [115-117]. Previous experiments have shown that the thermopower of CNTs is sensitive to oxygen absorption, molecular collisions and gate voltages [75,104,118,119]; here I show that it is also sensitive to mechanical deformation.

In contrast, although the thermal conductivity curve shows a 10% fluctuation in Fig. 9-6(d), there is no clear correlation between the thermal conductivity and the bending angles. It is especially dramatic at the two extremes where the bending angles (determined by the projective images) are larger than 90° and 130°, respectively. Since the nanotubes generally move out of the projection plane (as clearly seen in the 15th frame of Fig. 9-6(a) and also in the 13th frame of Fig. 9-7) and the height difference between the heater and sensor is smaller than 100nm, the real bending angles should be larger than the projective angles. The thermal conductivity fluctuation may be due to perturbations in the contacts under large strain. Applying the Wiedemann-Franz law to Fig. 9-6(d), I can estimate that the electronic contribution to the total thermal conductivity is less than 1%. The result is consistent with previous theoretical and experimental results [78,82,120].

Although it has been shown that CNTs are remarkably flexible and resilient [29], the robustness of the thermal conductivity against deformation is still surprising. A ripple-like structure has been observed when bending a multiwall CNT [121]. Generally, the "wavelength" of the ripple is ~10nm for a radius of curvature of~400nm and it decreases as the bending angle increases. With a radius of curvature of ~260nm as in the 15th frame in Fig. 9-6(a), one would expect that these ripples would scatter phonons efficiently because the phonon mean free path (~200nm) is much longer than the wavelength of the ripple. Thus it is surprising that the thermal conductivity of the CNT remains unperturbed when the bending angle is larger than 130°.

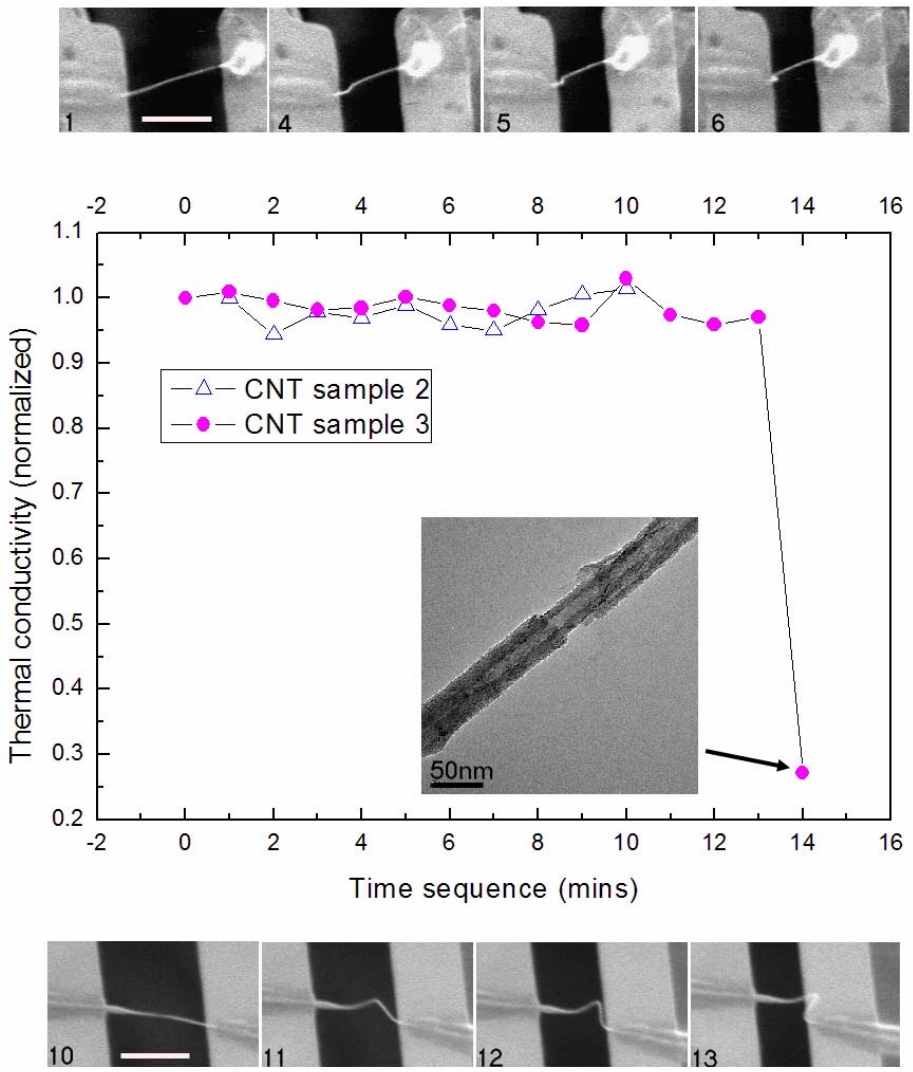

Figure 9-6 Upper part: a series of representative SEM images of CNT sample 2 undergoing one cycle of bending (scale bar = 2μm). Lower part: a series of representative SEM images of CNT sample 3 undergoing the third cycle of bending (scale bar = 2μm). The number in each frame denotes the time sequence in each sample, respectively. Middle panel: The thermal conductivity change of CNT sample 2 (open triangles) and CNT sample 3 (solid circles). The inset of the middle panel shows the TEM image after the defect was created in CNT sample 3 (scale bar = 50nm)

Figure 9-7 shows two CNTs under cyclic deformation. The thermal conductivity is normalized to the initial values of 290W/mK and 305W/mK for CNT samples 2 and 3, respectively. At the extremes, the CNTs are bent at angles larger than 125° and 140°, respectively. Unlike Fig. 9-6, here the two CNTs are buckled locally so their radii of curvature are smaller (~70nm and ~90nm, for CNT samples 2 and 3, respectively). Remarkably, the thermal conductivity remains unchanged when the radius of curvature is comparable to their phonon mean free path (~50nm). As shown in the last data point of CNT sample 3, the thermal conductivity starts to decrease only when some permanent defects are created by suddenly releasing the device under strain. The TEM image in the inset of Fig. 9-7 clearly displays such defects.

To investigate whether this unique property is universal, I have extended my study to BNNTs. BNNTs are known to have comparable Young's modulus, phonon dispersion relation and thermal conductivity as those of CNTs, but because of their large band gap, their thermal properties are purely phononic. I have also found that, like CNTs, the thermal conductivity of BNNTs does not change until permanent defects are created.

Although I can qualitatively explain the observed correlation of the resistance and thermopower of CNTs under deformation, it is difficult to understand the robustness of the thermal conductivity of CNTs and BNNTs from a traditional point of view. In reality, most materials under strain will create defects or dislocations and thus reduce their thermal conductivity. So it is surprising that CNTs or BNNTs do not create permanent defects when bending the nanotubes at angles larger than 140°. More surprisingly, their phonon mean free path exceeds the wavelength created by the ensuing ripple-structures.

The unusual robustness of nanotubes makes one wonder what would happen to the phonon transport when the nanotubes are extremely deformed. Theoretically, even if no defects or dislocations are present; the thermal conductivity of an object will start to decrease when its radius of curvature is smaller than the phonon mean free path. Thus the phonon mean free path sets an ultimate limit to the minimum radius of curvature beyond which the thermal conductivity starts to decrease. The robustness of phonon transports of CNTs or BNNTs does not violate, though it is close to, this ultimate limit. For an ordinary electromagnetic waveguide, a slight deformation will create mismatching of modes, thus results in a significant power loss. For an optical fiber, the minimum radius of curvature for bending is set by the relative refraction index, and is usually much larger than the wavelength of light. Here I show that nanotubes can be bent to a radius of curvature comparable to the phonon mean free path without losing its high thermal conductivity properties. Therefore, nanotubes not only can be sensitive nanoelectromechanical devices, but also extremely good and robust broad-band phonon waveguides.

Chapter 10 Tuning the thermal conductance of nanotubes

10.1 Introduction and experimental procedures

Unlike electrical resistivity which can vary by more than 10^{12} from insulators to metals, thermal conductivity varies by less than 10^{4} from the best thermal conductors to the best thermal insulators. In addition, unlike typical field-effect transistors which can change on-off resistances by more than 10^{6}, no devices have been shown to exhibit tunable thermal conductance. This lack of variability and tunability of phonon transport in materials is the main obstacle for heat management and further processing of phonons as information carriers.

Multiwall carbon nanotubes (MWCNTs) comprise concentric cylindrical shells or layers of strongly sp^2-bonded carbon atoms, whereas the interlayer interaction is predominantly van der Waals [21]. The large disparity between the strength of the sp^2 bonding and the van der Waals interactions has enabled people to construct various nanoelectromechanical devices based on MWCNTs. For example, Cumings and Zettl built linear bearings and rheostats by telescopically extending the MWCNTs [34,122]. The friction force was determined to be less than 10^{-14} N per atom. Fennimore *et al*.

made rotational actuators based on MWCNTs [36]. Jensen *et al.* demonstrated tunable resonators based on telescoping MWCNTs. Theoretical calculations have suggested that these telescoping properties can be used as giga-Hertz linear oscillators [37]. Here I demonstrate that the thermal conductance of a MWCNT can also be controllably and reversibly tuned by sliding the outer shells with respect to the inner cores. The thermal conductivity shows a ten-fold decrease after extending the length of a MWCNT by 190nm. Thus I have made MWCNTs as nano-scale thermal rheostats.

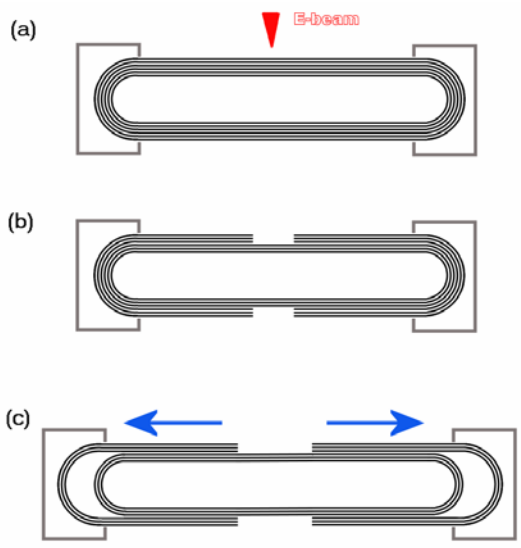

Figure 10-1 Schematic diagram of experimental procedures. (a) the outermost layers of a MWCNT were anchored to the electrodes and then the middle section of the MWCNT was partially cut using the electron beam of an SEM. (b) the outer-layers of the MWCNT were removed under electron beam irradiation. (c) a manipulator was used to pull the suspended electrodes so that the released outer-layers slide away from each other.

Figure 10-1 shows the schematic diagram of the experimental procedures. In Fig. 10-1(a), the outermost layers of a MWCNT were anchored to the electrodes and then the middle section of the MWCNT was partially cut using the electron beam of an SEM. Previous experiments have shown that the presence of H_2O molecules facilitate the

cutting time [113]. But to avoid contamination, I did not introduce H_2O molecules and the chamber vacuum was taken below 5×10^{-6} mbar before turning on the electron beam. Under electron beam irradiation, parts of the outer-layers of the MWCNT were removed as shown in Fig. 10-1(b). Thus the released outer-layer sections were weakly bonded to the inner cores via van der Waals interactions. In Fig. 10-1(c), I use a manipulator to pull the suspended electrodes so that the released outer-layers slide away from each other, effectively increasing the length of the MWCNT. The position of the manipulator was carefully chosen so that it would not perturb the heat profile of the thermal conductivity test fixture.

From TEM imaging, the MWCNT investigated has outer diameter = 9.6nm, inner diameter = 7.2nm and length = 2.73μm. The upper part of Fig. 10-2 shows a series of representative SEM images of a MWCNT undergoing the cyclic sliding processes. The increasing length of the visible thin section of the MWCNT suggests that the outer-layers slide against the inner cores and also excludes the presence of the axial strain in the MWCNT. The thermal conductivity of the original MWCNT was measured to be 1100W/mK. After electron beam irradiation, the thermal conductivity reduces to 380W/mK, equivalent to $K = 4.4\times10^{-9}$ W/K. The lower panel of Fig. 10-2 shows the measured K at different time frames. K is normalized to its initial value of 4.4×10^{-9}W/K. Notably, the minimum of K is only 15% of the initial value. Furthermore, the sliding process is fully reversible, as shown in Fig. 10-2, K returns to its initial value after the MWCNT is restored to its original shape. I do, however, observe hysteresis behavior after a few cycles of the sliding process. TEM imaging shows a thin layer of amorphous

material coating the surface of the MWCNT, possibly causing the hysteresis. Ideally, as it has been demonstrated in previous experiments [34], the sliding motion can go many cycles without wearing. Thus the performance of the MWCNT thermal device can be improved if operated in a cleaner environment.

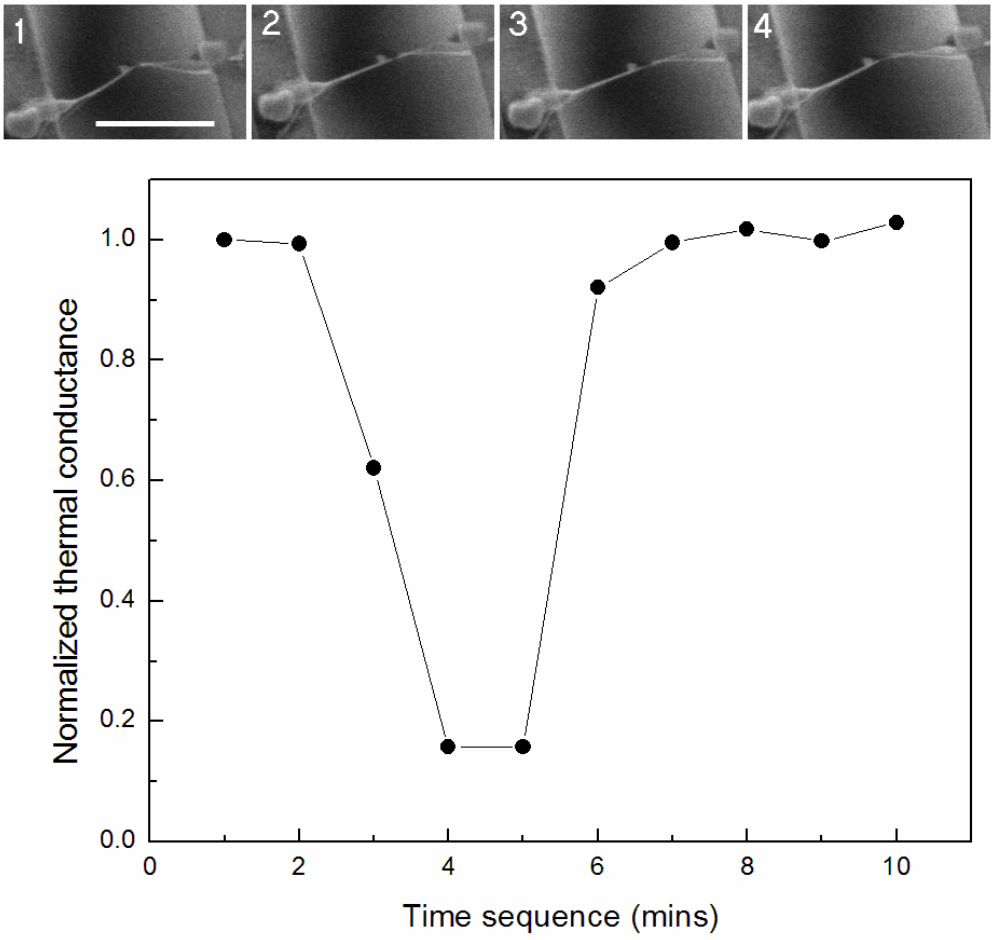

Figure 10-2 Upper part: a series of representative SEM images of the MWCNT undergoing cyclic sliding processes. The number in each frame denotes the time sequence number (scale bar = 2μm). Lower panel: the thermal conductance vs. time during sliding. The thermal conductance is normalized to the initial value of 4.4×10^{-9}W/K.

10.2 Analysis and Discussions

Figure 10-3 shows the normalized thermal resistance ($1/K$) with respect to the distance between the electrodes. At the beginning, increasing the distance between the electrodes only straightens the MWCNT but does not affect its thermal resistance. This is consistent with the experimental results in chapter 9 showing that MWCNTs can sustain high thermal conductivity at very large bending angles. Notably, when the outer shells of the MWCNT start to slide with respect to the inner core, the thermal resistance increases dramatically. Due to the limited data points available, I can not constrain a specific fitting curve here. For comparison purposes, previous electrical resistance measurements on telescopically extended MWCNTs have found an exponential form for the electrical resistance behavior

$$R(x) = R_0 \exp(2x/l_e) \tag{10.1}$$

where x is the sliding distance, l_e = 1000~1500nm is the electronic localization length [122]. If I adapt the same formula to fit the data in Fig. 10-3, I find that the phononic localization length l_{ph} = 87nm, which is much shorter than l_e. The result suggests that for MWCNTs K is more sensitive to telescopic modulation than the electrical resistance.

The change of K does not scale with the extended length of the MWCNT, so the observed phenomenon is not like stretching a rubber band. Besides, a thermal diffusive model based on the geometry of the investigated MWCNT predicts that K only decreases

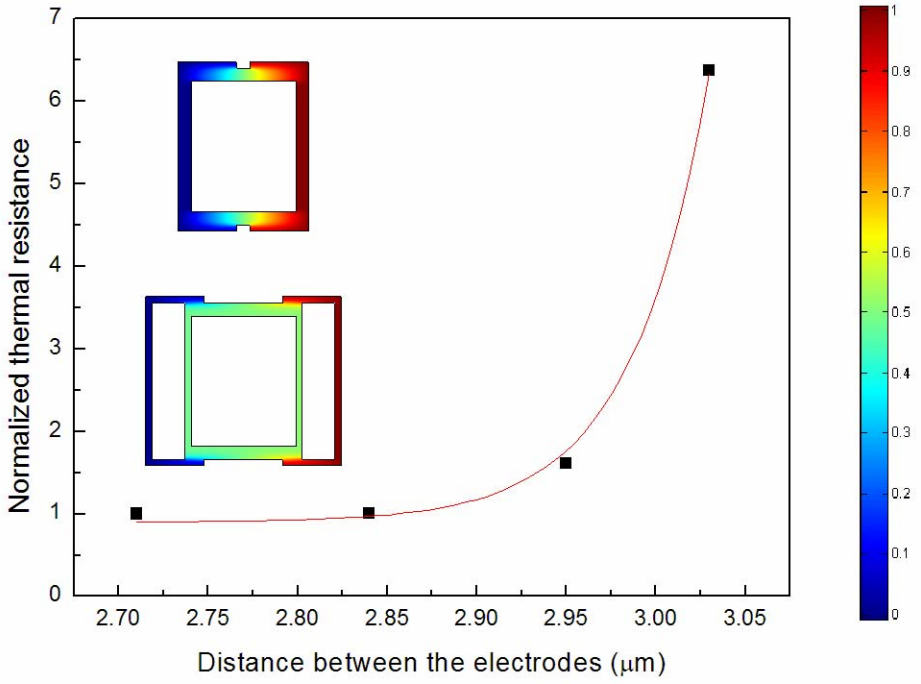

Figure 10-3 (Color) The normalized thermal resistance (1/*K*) vs. the distance between the electrodes during sliding. The curve is fit using Eq. (10.1). Insets: the two-dimensional projection of the temperature profiles of an effective model before (upper inset) and after (lower inset) sliding. The model has the same outer to inner diameter ratio as that of the MWCNT investigated, but has a much shorter length. The simulation of the lower inset gives a reduction of thermal conductance of 84% from its original configuration (upper inset).

by 23% after extending by 190nm, which is much smaller than the observed value (85%). To quantitatively understand the origin of the large change of *K*, I have built an effective model based on the finite element analysis method. As shown in the insets of Fig. 10-3, the two-dimensional projection of the model has the same outer to inner diameter ratio as the investigated MWCNT, but its length is much shorter than that of the MWCNT.

Based on the results of the thermal conductivity of graphite, an anisotropic factor of 100 is introduced into the model [38]. In the lower inset of Fig. 10-3, I find that the model can give a decrease in K of 84% after sliding, which quantitatively agrees with the observed value.

The effective model has the following implications. First, as shown in the insets of Fig. 10-3, the most resistive part of the extended MWCNT occurs at the overlap between the outer shell and inner core, where a large phonon scattering angle is needed to transfer heat. Second, the phonon transport in the rest of the MWCNT is nearly ballistic, as evidenced by the large contrast between the length of the model and that of the MWCNT. In fact, I can estimate the phonon mean free path in the rest part of the MWCNT to be 370nm from the model. Third, if no anisotropy is assumed, the model can only give a decrease of K of 67% in the lower inset of Fig. 10-3, thus the large anisotropy of the thermal conductivity between the axial and the radial directions also plays an important role.

In summary, I have controllably and reversibly tuned the thermal conductance of a MWCNT by sliding the outer shells with respect to their inner cores. The thermal conductance of the MWCNT decreases by 85% after extending the length by 190nm. An effective thermal diffusive model suggests that the phonon transport of the telescopically extended MWCNT is limited by the region where the outer shells and inner cores overlap, while it is nearly ballistic in the rest of the MWCNT.

Chapter 11 A thermal rectifier and evidence for solitons

11.1 Introduction and experimental procedures

Solitons are non-perturbative results of non-linear systems. They are localized, particle-like entities that can collide with each other without changing shape. The soliton phenomena were first discovered by John Scott Russell in 1834 when he observed a solitary water wave propagating along Edinburgh's Union Canal without decay [123]. Later solitons were found in many physical phenomena ranging from optical fibers to tsunami waves [124,125]. While significant effort has been devoted to the search for solitons in the electronic transport of one-dimensional conductors, evidence of solitons in thermal conduction has remained elusive [126]. In Chapter 9, the considerable robustness of the thermal conductivity of nanotubes under severe deformation has suggested the existence of solitons in nanotubes. Here I present evidence for solitons in the thermal transport of carbon nanotubes (CNTs) and boron-nitride nanotubes (BNNTs). The idea is based not on a specific soliton model, but on a general asymmetric result of solitons' solutions when propagating in a one-dimensional inhomogeneous media. Solitons are the only wave phenomena that can give asymmetric thermal conductivity in such a system.

The making of a thermal rectifier in a nanotube with an inhomogeneous mass distribution gives the strongest evidence for solitons in nanotubes.

Nanotubes are nearly one-dimensional materials whose structure can be viewed as a cylindrically rolled graphene or BN sheet. The electronic contribution to the total thermal conductivity of CNTs has been shown to be less than 1% [120]. On the other hand, BNNTs are wide band gap insulators, so the thermal transport is exclusively due to lattice contributions. This makes BNNTs ideal materials for investigating one-dimensional heat transfer phenomena.

Figure 11-1(a) shows an SEM image of a multiwall CNT connected to the electrodes and Fig. 11-1(b) shows the corresponding low magnification transmission electron microscopy (TEM) image. A symmetrical measurement performed by switching the heater and senor was conducted before engineering the nanotube. Although the heater and senor were made to be symmetric, a small asymmetry (<10%) was observed. The asymmetry may be due to the fabrication process of the test fixture, the wire bonding, or even the intrinsic properties of the nanotube. The background asymmetry was normalized to one so I could compare the net thermal rectification effect before and after I engineered the nanotube. $C_9H_{16}Pt$ was then deposited on one side of the nanotube, as shown in the TEM image in Fig. 11-1(c). After asymmetrically coating $C_9H_{16}Pt$ onto the nanotube, the thermal conductance of the nanotube was again tested in both directions. The thermal rectification of the nanotube is defined as follows:

$$Rectification = \frac{K_{LR} - K_{RL}}{K_{LR}} \times 100\% \tag{11.1}$$

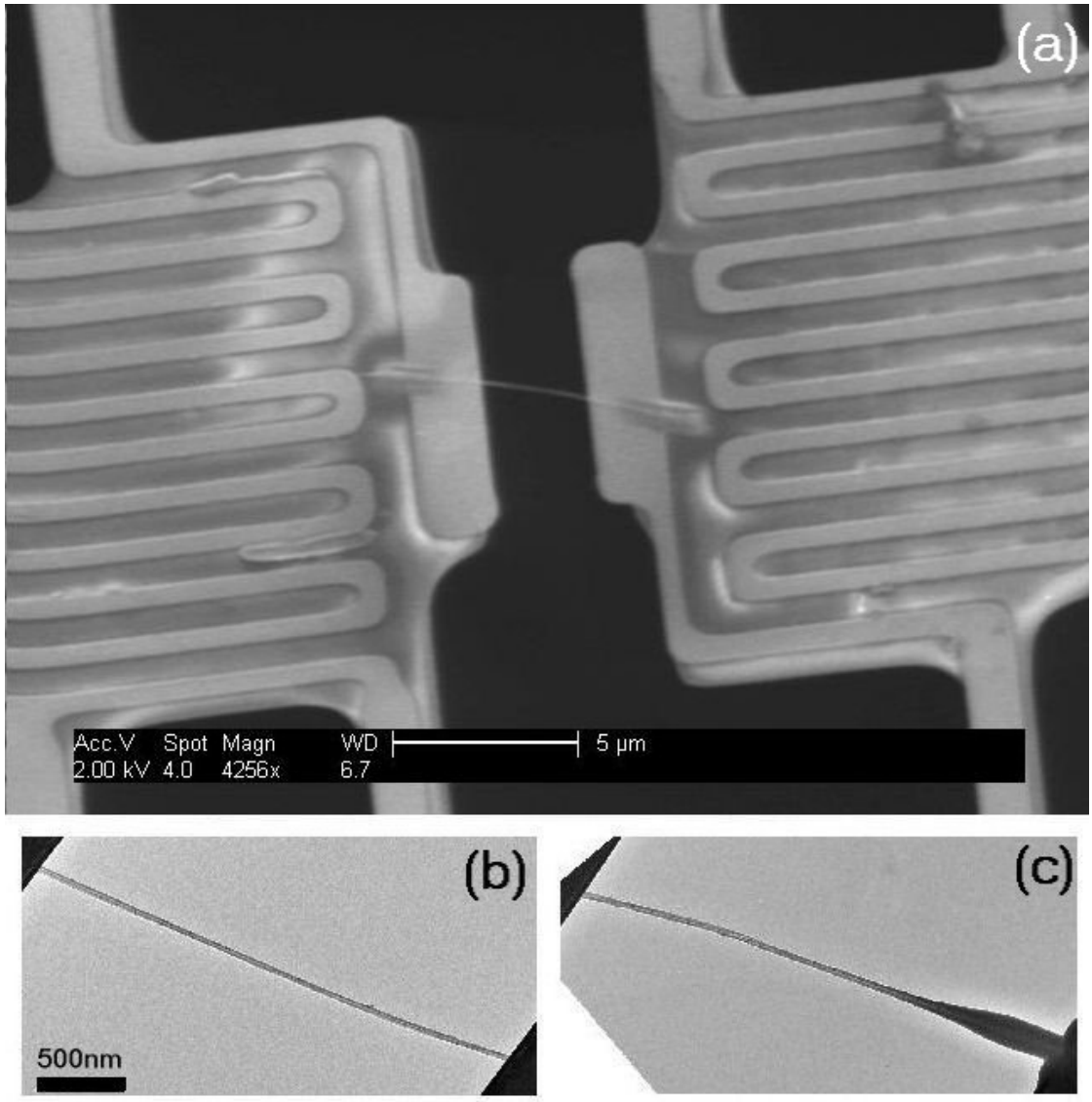

Figure 11-1 (a) The SEM image of a CNT connected to the electrodes (scale bar = 5μm). (b) The corresponding low magnification TEM image of (a). (c) The TEM image of the same CNT after depositing $C_9H_{16}Pt$.

where K_{LR} and K_{RL} are the thermal conductance of the nanotube when heat flows from left to right and right to left, respectively.

Figure 11-2 shows the structure of $C_9H_{16}Pt$ molecule. Irradiating electron beams on $C_9H_{16}Pt$ molecules transforms them from gas form to solid polymers. Thus depositing $C_9H_{16}Pt$ on a nanotube has two effects on the thermal conductance. As shown in Fig. 11-3(a), when the bonding between $C_9H_{16}Pt$ molecules is strong, the total conductance will increase due to parallel contributions from the nanotube and the $C_9H_{16}Pt$ molecules. On the other hand, when the bonding between $C_9H_{16}Pt$ is weak, it locally increases the effective mass of the nanotube as shown in Fig. 11-3(b). The former case can be excluded by measuring the thermal conductivity of $C_9H_{16}Pt$ bridging across the electrodes. The thermal conductivity of $C_9H_{16}Pt$ is less than 1% of that of nanotubes and can thus be neglected here. Thus the low thermal conductivity and weak bonding of $C_9H_{16}Pt$ molecules ensure that the mass effects dominate. Furthermore, the molecular weight of $C_9H_{16}Pt$ (~319 g/mole) is much larger than that of $(C\text{-}C)_5$ or $(BN)_5$ (~120 g/mole) of similar sizes, suggesting that depositing $C_9H_{16}Pt$ can efficiently change the mass distribution of a nanotube.

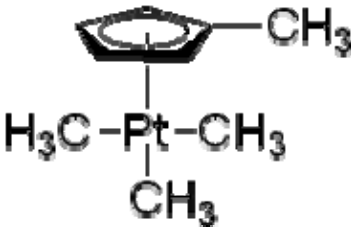

Figure 11-2 The structure of Trimethyl(methylcyclopentadienyl)platinum(IV) (or named Trimethyl [(1,2,3,4,5-ETA.)-1 Methyl-2, 4-Cyclopentadien-1-yl] Platinum)

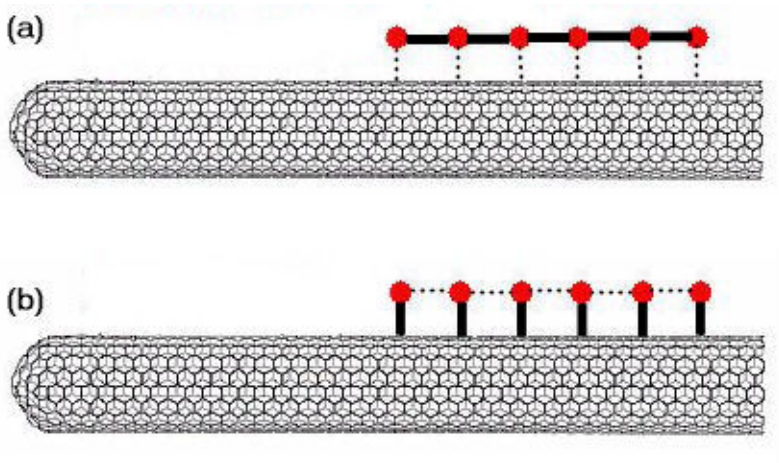

Figure 11-3 A schematic description of the effect of depositing $C_9H_{16}Pt$ on nanotubes. (a) When the bonding between $C_9H_{16}Pt$ is strong, depositing $C_9H_{16}Pt$ contributes an additional thermal conductance. (b) When the bonding between $C_9H_{16}Pt$ is weak, depositing $C_9H_{16}Pt$ changes the effective mass of the nanotube.

Figure 11-4(a) to (c) show three BNNTs deposited with $C_9H_{16}Pt$. At room temperature, the rectifications are measured to be 7%, 4%, and -3% (the minus sign is due to the definition from Eq. (11.1)), respectively. The CNT in Fig. 11-1(c) shows rectification of -2%. The arrows in Fig. 11-4 denote the direction of heat flow in which a higher thermal conductance is observed. All the results show consistently that a higher thermal conductance is observed when heat flows from a heavy region (more $C_9H_{16}Pt$ is deposited) to a light region (less $C_9H_{16}Pt$ is deposited). The observed rectification effect is larger than the measurement uncertainties (~1%). Since for BNNTs, electrons do not contribute to the thermal transport, here it is clearly demonstrated that the observed rectification effects are due to lattice contributions. I have found that depositing more

$C_9H_{16}Pt$ does not necessarily increase the rectification effect, which is possibly due to stronger interconnection between $C_9H_{16}Pt$ molecules. When the interconnection of $C_9H_{16}Pt$ molecules becomes strong, the effect of deposition shifts from Fig. 11-3(b) to Fig. 11-3(a), thus reduces the rectification effect due to mass inhomogeneity.

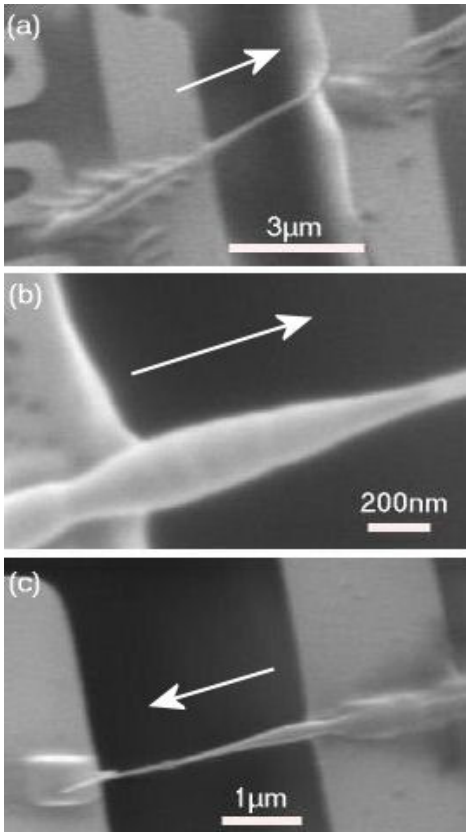

Figure 11-4 (a) to (c) SEM images of three different BNNTs after depositing $C_9H_{16}Pt$. The rectification measured is 7%, 4%, -3% (see Eq. (11.1) for the definition of rectification)). The arrows in each figure denote the direction of heat flow where the thermal conductance is higher than that of the opposite direction.

11.2 Evidence for solitons

Now I attempt to describe my results in light of various established models. It is worthy to note that although asymmetric results such as light waves propagating across

media of different refraction indexes are very common in two or three dimensions, there is no corresponding asymmetry in one-dimensional systems. In one dimension, the reflectivity (R) and the reflection coefficient (r) of a wave propagating across different media follows

$$R = r^2 = \left(\frac{k_i - k_t}{k_i + k_t} \right)^2 \tag{11.2}$$

where k_i and k_t are the wave numbers of incident waves and transmitted waves, respectively. The square in Eq. (11.2) makes the reflectivity the same irrespective of the direction of incident waves. Since phonons are quanta of waves, the above result demonstrates that no thermal rectification can be observed for ordinary wave transport.

An asymmetric result will show in a collision process involving two particles of different masses. As the elementary kinetic theory shows, for an incident particle of mass m_1 and incident velocity v_i colliding with another particle of mass m_2 will result in a final velocity (V_f):

$$V_f = \frac{m_1 - m_2}{m_1 + m_2} v_i \tag{11.3}$$

The incident particle will reflect back if $m_2 > m_1$, and continue forward if $m_2 < m_1$. However, for ordinary thermal conductors no mass transfer is involved, so the above case does not apply in my experiment.

Nonlinear perturbative effects such as umklapp processes only decrease the total thermal conductance of the nanotube. But no thermal rectification effect can be expected.

An asymmetric geometrical shape of a sample can introduce asymmetric boundary scatterings of phonons. Thus the thermal conductance can be reduced in one direction while increased in another direction. In this scenario, thermal conductance is higher when heat flows from a narrow region to a wide region. However, the phonon rectification observed in my experiments displays an opposite directionality. As shown in Fig. 11-4(a) to (c), the thermal conductance is higher when heat flows from a wide (heavy) region to a narrow (light) region. Therefore, the effect due to asymmetric shape is excluded. Qualitatively, the sp^2 bonds in nanotubes are much stronger than the bonds between $C_9H_{16}Pt$ molecules, so the phonons should be mainly confined within the nanotubes and thus one would not expect the phonons to feel a significant geometrical asymmetry or see the resulting thermal rectification.

Finally, I turn to soliton models. Calculating the reflection and transmission coefficients of a soliton propagating across a discontinuous media is not a trivial problem. For the limited models that analytical or numerical results can be obtained, the asymmetry of the heat flow is a general feature. For example, T. Iizuka and M. Wadati obtained the reflection amplitude for Korteweg-de Veries (KdV) equation [127]:

$$r = \begin{cases} 0 & \left(\nu = \sqrt{\dfrac{m_2}{m_1}} \le 1\right) \text{ no soliton} \\ \left(\sqrt{2\dfrac{\nu-1}{\nu+1}+\dfrac{1}{4}}-\dfrac{1}{2}\right)^2 & \left(\nu = \sqrt{\dfrac{m_2}{m_1}} > 1\right) \text{ one soliton} \end{cases} \tag{11.4}$$

where m_1 and m_2 are the mass of lattice of incident and transmitted waves, respectively. The most significant result of Eq. (11.4) is the asymmetry with respect to $m_2/m_1 = 1$. It

gives a direction of the thermal rectification consistent with my results. If I use Eq. (11.4) to analyze the result, it gives *rectification* > 7% when $m_2/m_1 > 2$, which lies within the molecular weight ratio of $C_9H_{16}Pt$ to $(C\text{-}C)_5$ or $(BN)_5$. However, currently I only know the solitons contribute > 7% to the total thermal conductance, and it is not clear whether the KdV model can apply for nanotubes. Other models, such as nonlinear Schrödinger equation [127], sine-Gordon model [128] or ϕ^4 model [129] also give asymmetric results though they are more complicated. Quantitative results can only be compared after a soliton model for nanotubes is established. Therefore, I emphasize that the strongest evidence for the existence of the solitons in nanotubes is due to the observed asymmetry, which is not possible in other linear or non-linear perturbative systems.

Theoretical works have suggested stable solitons in nanotubes [130,131]. Studies on the soliton-defect interactions suggest that heat energy can be localized on a few bonds of defects. Thus solitons can explain the "self-healing" effect when biasing carbon nanotubes at high currents [110,132]. In addition, in Chapter 10 I have shown that the thermal conductivity of nanotubes remains unperturbed even when the wavelength of the "wiggle" structures induced by deforming a nanotube is much smaller than the phonon mean free path. More surprisingly, the robustness of thermal transport of nanotubes approaches the ultimate limit in which the bending radius of curvature is comparable to the phonon mean free path. All these findings have challenged current understandings of the thermal transport of nanotubes. Since solitons can propagate at a constant velocity without being degraded by lattice perturbation, it naturally explains the robustness of thermal transport. Among these supports, the strongest evidence comes from the

observed rectification effect, which is due to a fundamental asymmetry of solitons' solutions.

A unique by-product of the result is the invention of a thermal rectifier. What are the potential applications of thermal rectifiers? They can be used for nanoscale devices to macroscopic objects where the thermal insulation is needed in one direction while remains good thermal contacts to the environment in another direction. For example, ultra-sensitive nanoscale bolometers or calorimeters require the heat energy be confined in the sensing area so that large signals can be obtained; while they also need the devices to have good thermal contacts to the base temperature such that good sensitivity can be maintained [133-135]. Low energy buildings need to reduce the heat loss in winter or power consumption in summer [136,137]. More importantly, with the invention of thermal rectifiers, phonons should no longer be considered as unwanted by-products of electronics. Phonons, like electrons, are information carriers, and should be processed accordingly. In the past, people have relied on semiconductor or superconductor devices to read out thermal signals. Now it is possible to process the thermal signals in advance and convert them into electronic signals later. The invention of a thermal rectifier will pave the way for the field of phononics.

Chapter 12 Breakdown of Fourier's law in one-dimensional thermal conductors

12.1 Background and experimental results

In analogy to Ohms' law for electrical conductors, Fourier's law is an empirical rule of heat transfer. Although Fourier's law is well-established for ordinary thermal conductors, efforts for providing a rigorous theoretical ground have failed [138]. Since Peierls tried to explain Fourier's law based on kinetic gas models, the presence of anomalous heat conduction in one-dimension has been a puzzle [70]. Recently, this subject has attracted renewed interests due to progress in simulation power. Although it has been proven that Fourier's law is violated for harmonic chains and integrable systems [139], the criteria when Fourier's law holds is poorly understood [138]. Contradictory results have appeared in different models in the past decade. Theoretically, the criteria for Fourier's law have changed from impurities effects to local temperature gradients [140,141]; from on-site external potentials to momentum conservation [142,143]; from anharmonicity to the onset of chaos etc [75,144]. The violation of Fourier's law seems to

be commonplace in these models; while the criteria for Fourier's law remains a mystery [145]. Recently it is argued that for momentum-conserving systems, Fourier's law is violated and the thermal conductivity (κ) diverges with the size of the system (L) as $\kappa \sim L^{0.33}$ [143]. However, existing numerical results do not support a universal constant [75]. Despite these theoretical works, no experimental data are available for comparison. The lack of experimental data is mainly due to elaborate fabrication processes required to measure the κ for one-dimensional materials, with the ability to physically vary the size of the investigated object being even more difficult. Here I present a method that can effectively change the length of a nanotube while measuring its κ. Thus I can experimentally check the validity of Fourier's law in one-dimensional materials.

Boron-nitride nanotubes (BNNTs) are nearly one-dimensional materials with excellent mechanical and thermal properties. Due to their wide band gap, the thermal conductance of BNNTs is exclusively due to lattice contributions. This property makes BNNTs ideal materials for investigating one-dimensional thermal transport.

Figure 12-1(a) shows the device with two "walls" of $C_9H_{16}Pt$ deposited on it. A BNNT was anchored to the electrodes using $C_9H_{16}Pt$ deposition. The height of the $C_9H_{16}Pt$ "wall" ensured that the BNNT was suspended, as shown in Fig. 12-1(b). I then measured the thermal conductance of the BNNT. This process was repeated by a series of depositions, thus the suspended segment of the BNNT was reduced, as shown in Fig. 12-2(a) (Sample 1). Figure 12-2(b) shows another BNNT device with four depositions (Sample 2).

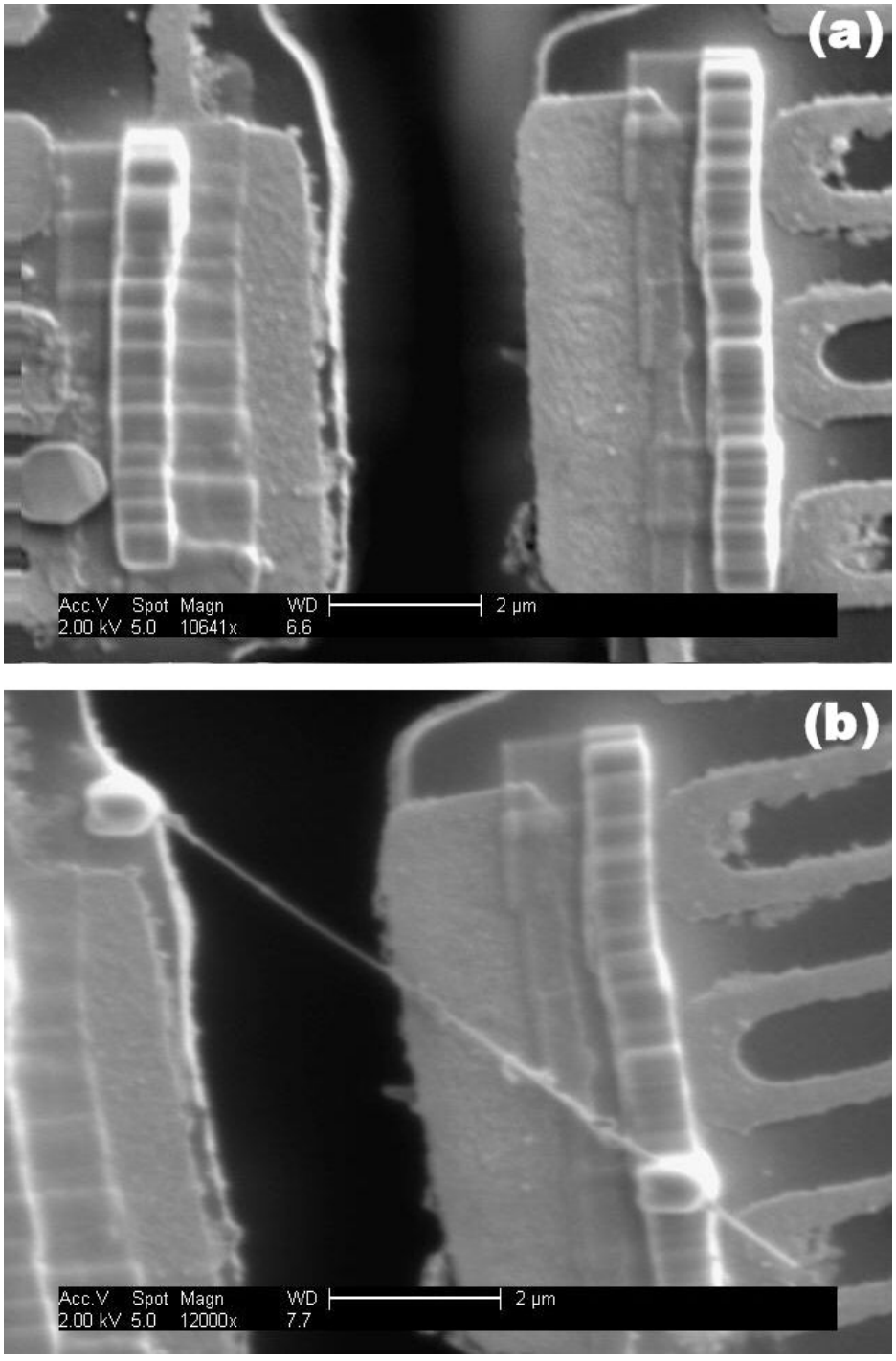

Figure 12-1 (a) A blank device with two "walls" of $C_9H_{16}Pt$ deposited on the electrodes. (b) The same device with a BNNT (Sample 1) connected to it (scale bar = 2μm).

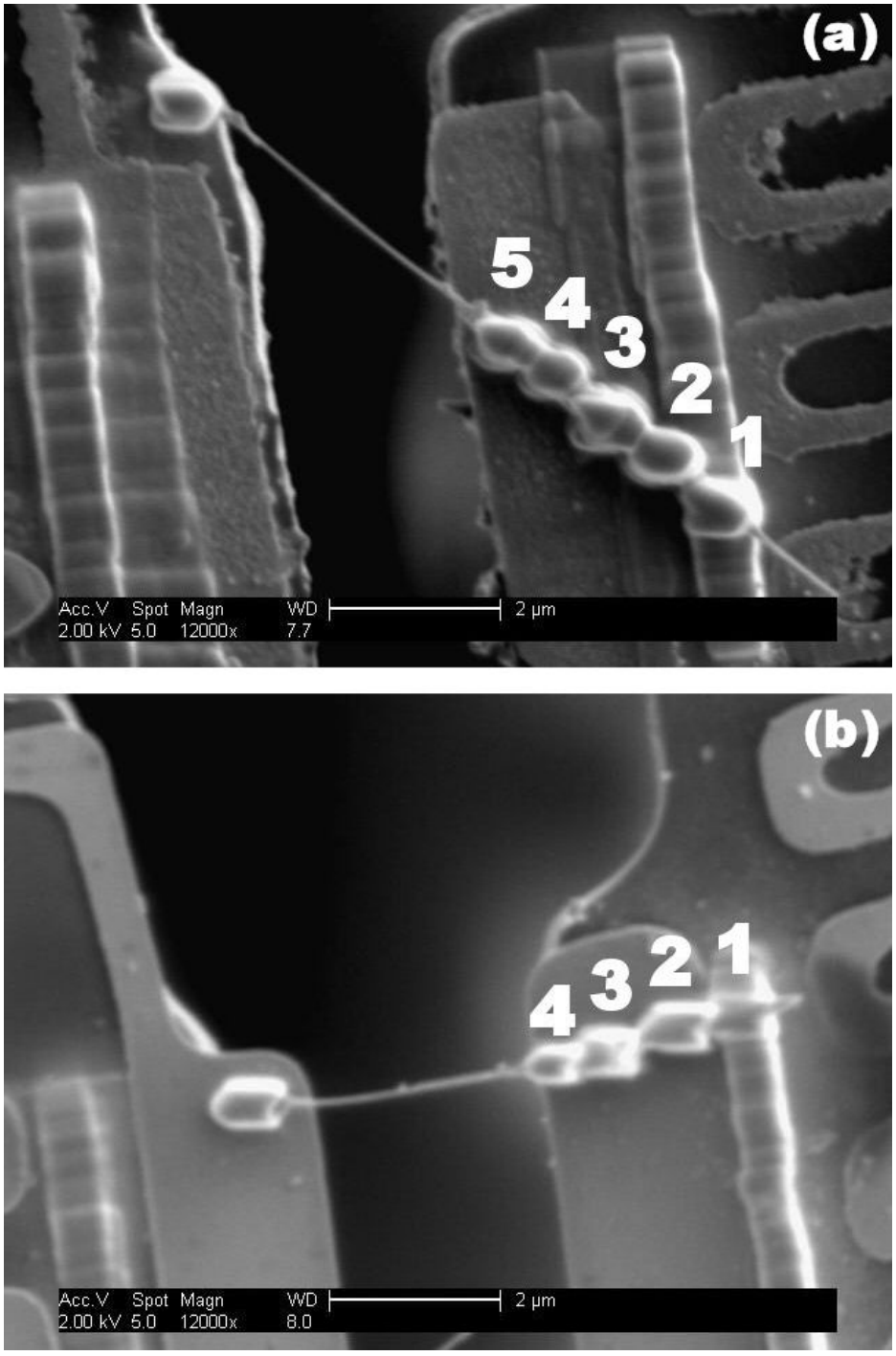

Figure 12-2 (a) Sample 1, a BNNT with five sequential depositions of $C_9H_{16}Pt$. (b) Sample 2, a BNNT with four sequential $C_9H_{16}Pt$ depositions (scale bar = 2µm).

As shown in the inset of Fig. 12-3(a), I model the thermal *resistance* of the nanotube to be equivalent to a series of resistors R_s connected to each other, with contact resistance R_c(n) (n = sequence number) representing each $C_9H_{16}Pt$ deposition connected parallelly to the whole circuit (Model A). Since the deposition condition was kept the same, I assume that each R_c(n) can be normalized by their size and obtain the same contact resistance per unit length (R_c). I also modify Fourier's law by introducing an exponent β so that $\kappa \sim L^{\beta}$. A computer program is employed to analyze the result. For a given β, the program searches the parameter space spanned by R_s and R_c to find the minimum deviation to the experimental value. The deviation (σ) is defined as follows:

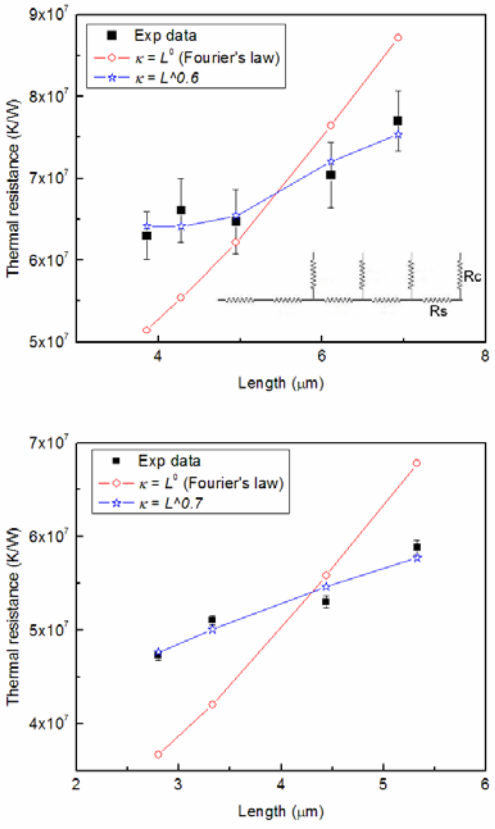

Figure 12-3 Inset: the circuit Model A for data analysis. (a) Thermal conductance vs. length between contacts for Sample 1. (b) Thermal conductance vs. length between contacts for Sample 2. The experimental results are shown in solid squares with error bars. The analyzed results are shown in open circles (β=0) and open stars (β=0.6 and 0.7 for Sample 1 and Sample 2, respectively).

$$\sigma = \left(\sum_{n=1}^{m} (R_{meas}(n) - R_{cal}(n))^2 \right) / \left(R_{meas}(1) \right)^2 \qquad (12.1)$$

where m = 5 and 4 for Sample 1 and Sample 2, respectively. $R_{mea}(n)$ and $R_{cal}(n)$ are the measured thermal resistance and the calculated result at each sequence, respectively.

Figure 12-3(a) and (b) shows the results of Sample 1 and Sample 2. It is clear that the largest deviation occurs when I adapt Fourier's law (β=0) in my fitting. Surprisingly, the best fit occurs when β=0.6~0.7, which is close to the result of ballistic transport (β=1). From the best fit, I find that the thermal conductance of the BNNTs are 1.3×10^{-8}W/K and 1.7×10^{-8}W/K at the first sequence of Sample 1 and Sample 2, respectively. The R_c contributes less than 7% and 3% to the total resistance of Sample 1 and Sample 2, respectively. Figure 12-4 shows the variation of σ with respect to β. Apparently, σ's of both samples show the largest deviation to Fourier's law (β=0). The samples show consistently that best fit occurs at β=0.6~0.7, which indicates the exponent is universal for BNNTs.

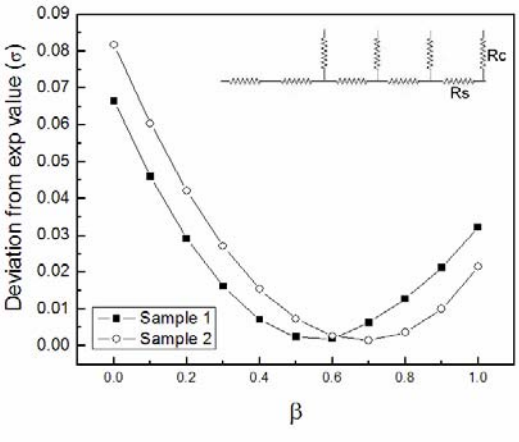

Figure 12-4 Calculated deviation (σ) with respected to β for the results of Sample 1 (solid square) and Sample 2 (open circle) using Model A (shown in the inset).

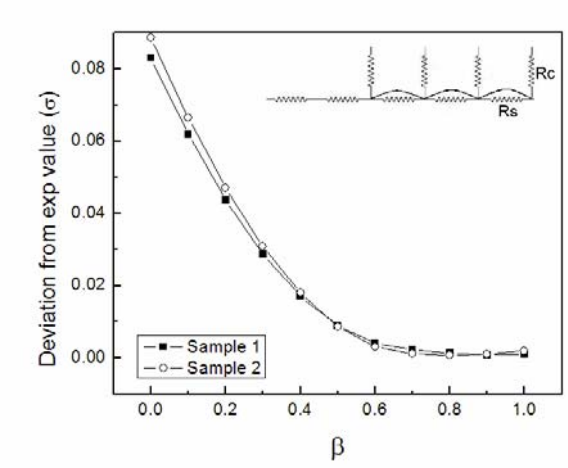

Figure 12-5 Calculated deviation (σ) with respect to β for the results of Sample 1 (solid circles) and Sample 2 (open triangles) using Model B (shown in the inset). Model B assumes that the resistors are shorted to each other under the contacts.

One may ask the fidelity of Model A to the real system. I understand the difficulty in modeling the resistor network beneath the contacts. For Model A, I assumed that there are potential drops between each contact. However, since the contacts are large and act like a heat bath, the potential drop in the nanotube can be smaller than expected in Model A. So I have tried an extreme model where the potential drop between the contacts is zero (Model B). As shown in the inset of Fig. 12-5, Model B assumes that the resistors under the contacts are shorted to each other. Figure 12-5 shows the variation of σ with respect to β. Surprisingly, the minimums of σ occurs at β=0.8~0.9, and the maximum of σ occurs at β=0. Thus both models consistently suggest that Fourier's law is violated. Furthermore, my results do not support recent theoretical suggestions that β=0.33 for momentum-conserving one-dimensional chains [143]. Both models show better fits at larger β indicating that κ diverges with increasing L much faster than expected.

12.2 Discussions

Theoretically, it was once thought that the introduction of disorder could make Fourier's law hold in one-dimensional systems, but it was later found that disorder only yields a finite temperature gradient in a sample but still leads to a divergence of κ with β=0.5 [146]. In my samples, the natural-abundance boron has large isotopic disorder (19.9%^{10}B and 80.1% ^{11}B) and thus should have dramatic effects on κ. Indeed, I have shown in Chapter 8 that the isotope enhancement of κ to be over 50% by measuring κ of isotopically pure ^{11}BNNT. However, it is worthy to note that although isotopic disorder dramatically affects the value of κ, it does not change the divergence of κ in favor of Fourier's law.

Ballistic phonon transport can lead to β=1. To check whether the observed heat transport is ballistic, I adapt the traditional formula to estimate the phonon mean free path,

$$\kappa = \sum C v \ell \tag{12.2}$$

where C, v, and ℓ are respectively the specific heat, group velocity, and phonon mean-free-path, and the sum is over all phonon states. I obtain ℓ~20nm, which is much smaller than the length of the BNNTs. So the ballistic condition is not satisfied in either BNNT sample.

It is worthy to note that the ballistic phonon transport is not a necessary condition for violating Fourier's law [138]. Many one-dimensional models are shown to have anomalous heat transfer without satisfying ballistic conditions [75,143,144,147,148]. Calculations on single-wall carbon nanotubes have suggested β=0.3~0.4 [149]. However,

it should be noted that many earlier works and their analyses on the thermal transport of nanotubes were based on the traditional phonon transport model [38,149], and overlooked the non-perturbative nonlinear effect contributing to the heat transfer.

In chapter 9, I have provided evidence for the existence of solitons in nanotubes. First, I found that the thermal conductivity of nanotubes is surprisingly robust under severe structural deformation. Using Eq. (12.2) to estimate the phonon mean free path of the nanotube, I found that it exceeded the size of the "wiggle" structures induced by deformation. This unusual robustness challenges current understandings of the thermal transport of nanotubes. Since solitons can propagate through barriers without changing shape, the result indicates the presence of solitons in nanotubes. In chapter 11, I have made thermal rectifiers with efficiencies up to 7% by engineering the mass distribution along the nanotubes. The observed asymmetry of thermal transport is deeply rooted in the solutions of soliton models and is impossible to find in other linear or non-linear perturbative wave equations.

Ideally, solitons can freely propagate along the BNNT, thus it leads to $\beta=1$. However, calculations have shown that solitons in nanotubes are accompanied by phonon emission [131]. The accompanied phonon emission leads to a finite soliton lifetime and results in a deviation from $\beta=1$. So the observed $\beta=0.6\sim0.9$ is qualitatively consistent with the soliton picture.

The origin of the anomalous heat conduction in one-dimensional systems has been debated for many decades. In the past, theorists were misguided by the only existing experimental result: Fourier's law of bulk materials. Many models, even unrealistic ones,

have been adapted to explain the discrepancy between the theories and Fourier's law. Here I provide the first experimental evidence showing that Fourier's law is violated in BNNTs. My results confirm theorists' consensus that the breakdown of Fourier's law is generally independent of ballistic conditions or disorder effects. But the observed $\beta=0.6\sim0.9$ differs from some theoretical suggestions that $\beta=0.3\sim0.4$. Instead, it is consistent with the soliton model of nanotubes. Moreover, these studies can go beyond solely academic interest and provide stepping points for new solutions to thermal management problems on nano-scaled materials. Rectification of thermal transport is just one possibility [150,151].

Chapter 13 Prospects of phononics

With the relentless pursuit of the performance of microelectronics, the thermal management problem has become a major challenge. According to *2005 International Technology Roadmap for Semiconductors*, the thermal management problem has become a major obstacle in further improving the device performance. Due to the shrinking size, the problem is further magnified as the localized heat flux is targeted to reach 500 W/cm^2 in the next few years. This localized heat flux is the same as the one seen in the rocket nozzles of the space shuttle, but with the added challenge that the microprocessor must remain below 90°C and operate for many years.

What are the possible solutions? One solution is searching for thermoelectric devices with higher efficiency. Researchers' interests have been triggered due to recent successes in enhancing the figures of merit (ZT) in low-dimensional thermoelectric devices. A thermoelectric device with ZT larger than 3 will compete with the performance of a commercial refrigerator, while at the same time having the advantages of being light-weight and compact [152]. For this approach, one wishes to find materials exhibiting large thermopower, high electrical conductivity, but low thermal conductivity. A usual approach is fabricating a low-dimensional superlattice of a known thermoelectric material [153,154]. Due to increasing boundary scatterings of phonons, κ of two-dimensional superlattices is reduced, thus enhancing its ZT. However, despite that

enormous efforts have been devoted into optimizing thermoelectric device, so far a material with *ZT* greater than 3 has not been found at reasonable temperatures.

Another solution is to find materials exhibiting high thermal conductivity. However, very few materials are known to exhibit high κ at reduced dimensions. Traditional semiconductors like Si show a dramatic suppression of κ at the nano-scale [75]. Insulators used in microelectronic manufacture like Si_3N_4, SiO_2, and Al_2O_3 are all poor thermal conductors in traditional polycrystalline forms.

The experimental works shown in this thesis can provide the solution to the thermal management problem. In chapter 8, I have demonstrated that CNTs and BNNTs are excellent thermal conductors and their thermal conductivity increases as the diameter decreases. For nanotube diameters less than 10nm, their thermal conductivity above room temperature can even exceed that of diamond, the best thermal conductor known so far. More importantly, in chapter 12 I have shown the thermal conductivity of nanotubes diverges with its length. The violation of Fourier's law in nanotubes can solve the current thermal management problem with a fundamentally different approach. Imagine that an infinitely long nanotube will have infinite thermal conductivity!

We can proceed further and utilize the special properties of nanotubes described in this thesis with new prospects. In the past century, people have relied heavily on electrons to carry information, process signals and record data. Phonons, on the contrary, are generally considered as unwanted by-products. In fact, the traditional thermal management in microelectronics focuses entirely on how to efficiently dissipate heat to the environment. Now, with the advancement of nanotechnology, we can take a different

perspective. Phonons, like electrons, carry information, and should be utilized accordingly. In this thesis, I have demonstrated several basic elements of phononics based on CNTs and BNNTs. In analogy to the conducting wires in integrated circuits, I have constructed a phonon waveguide that can be bent to large angles without degrading its thermal conductivity. I have also invented a thermal rectifier, which serves as a thermal diode for heat flow. I have built a nanotube device with a tunable thermal conductance, essentially a phonon transistor. Combining these novel phononic elements with existing calorimeters or bolometers may give us unprecedented energy sensitivity that has not yet been achieved by modern electronics. In the future, we might use phononic sensors to detect thermal signals, then send them through phonon waveguides, amplify them using phonon transistors, process them by phonon rectifiers; finally, record them and read them using calorimeters or bolometers. The field of phononics is now emerging.

Bibliography

[1] H. W. Kroto, J. R. Heath, S. C. Obrien, R. F. Curl, and R. E. Smalley, Nature **318**, 162 (1985).

[2] W. Kratschmer, L. D. Lamb, K. Fostiropoulos, and D. R. Huffman, Nature **347**, 354 (1990).

[3] H. Kasatani, H. Terauchi, Y. Hamanaka, and S. Nakashima, Phys. Rev. B **47**, 4022 (1993).

[4] A. Goldoni, C. Cepek, and S. Modesti, Phys. Rev. B **54**, 2890 (1996).

[5] M. S. Dresselhaus, G. Dresselhaus, and P. C. Eklund, *Science of Fullerenes and Carbon Nanotubes* (Academic Press, New York, 1996).

[6] S. P. Kelty, C. C. Chen, and C. M. Lieber, Nature **352**, 223 (1991).

[7] A. F. Hebard, M. J. Rosseinsky, R. C. Haddon, D. W. Murphy, S. H. Glarum, T. T. M. Palstra, A. P. Ramirez, and A. R. Kortan, Nature **350**, 600 (1991).

[8] C. Cepek, I. Vobornik, A. Goldoni, E. Magnano, G. Selvaggi, J. Kroger, G. Panaccione, G. Rossi, and M. Sancrotti, Phys. Rev. Lett. **86**, 3100 (2001).

[9] N. G. Chopra, R. J. Luyken, K. Cherrey, V. H. Crespi, M. L. Cohen, S. G. Louie, and A. Zettl, Science **269**, 966 (1995).

[10] A committee report of H. Schon's scientific misconduct can be download at http://www.lucent.com/news_events/researchreview.html

[11] A. F. Hebard, C. B. Eom, Y. Iwasa, K. B. Lyons, G. A. Thomas, D. H. Rapkine, R. M. Fleming, R. C. Haddon, J. M. Phillips, J. H. Marshall, and R. H. Eick, Phys. Rev. B **50**, 17740 (1994).

[12] X. D. Xiang, J. W. Brill, L. E. Delong, L. C. Bourne, A. Zettl, J. C. Jones, and L. A. Rice, Solid State Communications **65**, 1073 (1988).

[13] X. Li, Y. J. Tang, H. Wang, H. W. Zhao, W. S. Zhan, and J. G. Hou, Phys. Status Solidi A-Appl. Res. **186**, 57 (2001).

[14] H. Q. Wang, X. Li, B. Wang, and J. G. Hou, J. Phys. Chem. Solids **61**, 1185 (2000).

[15] J. E. Fischer, A. R. McGhie, J. K. Estrada, M. Haluska, H. Kuzmany, and H. U. terMeer, Phys. Rev. B **53**, 11418 (1996).

[16] P. C. Hohenberg, and B. I. Halperin, Rev. Mod. Phys. **49**, 435 (1977).

[17] M. Chung, Y. Q. Wang, J. W. Brill, X. D. Xiang, R. Mostovoy, J. G. Hou, and A. Zettl, Physical Review B **45**, 13831 (1992).

[18] P. G. de Gennes, and J. Friedel, J. Phys. Chem. Solids **4**, 71 (1958).

[19] M. E. Fisher, and J. S. Langer, Phys. Rev. Lett. **20**, 665 (1968).

[20] S. Iijima, Nature **354**, 56 (1991).

[21] S. Iijima, and T. Ichihashi, Nature **363**, 603 (1993).

[22] D. S. Bethune, C. H. Kiang, M. S. Devries, G. Gorman, R. Savoy, J. Vazquez, and R. Beyers, Nature **363**, 605 (1993).

[23] R. Saito, M. Fujita, G. Dresselhaus, and M. S. Dresselhaus, Appl. Phys. Lett. **60**, 2204 (1992).

[24] M. S. Dresselhaus, G. Dresselhaus, and R. Saito, Carbon **33**, 883 (1995).

[25] T. Durkop, S. A. Getty, E. Cobas, and M. S. Fuhrer, Nano Lett. **4**, 35 (2004).

[26] Z. Yao, C. L. Kane, and C. Dekker, Phys. Rev. Lett. **84**, 2941 (2000).

[27] A. Y. Kasumov, R. Deblock, M. Kociak, B. Reulet, H. Bouchiat, Khodos, II, Y. B. Gorbatov, V. T. Volkov, C. Journet, and M. Burghard, Science **284**, 1508 (1999).

[28] Z. H. Chen, J. Appenzeller, Y. M. Lin, J. Sippel-Oakley, A. G. Rinzler, J. Y. Tang, S. J. Wind, P. M. Solomon, and P. Avouris, Science **311**, 1735 (2006).

[29] M. R. Falvo, G. J. Clary, R. M. Taylor, V. Chi, F. P. Brooks, S. Washburn, and R. Superfine, Nature **389**, 582 (1997).

[30] D. H. Robertson, D. W. Brenner, and J. W. Mintmire, Phys. Rev. B **45**, 12592 (1992).

[31] M. F. Yu, O. Lourie, M. J. Dyer, K. Moloni, T. F. Kelly, and R. S. Ruoff, Science **287**, 637 (2000).

[32] V. Sazonova, Y. Yaish, H. Ustunel, D. Roundy, T. A. Arias, and P. L. McEuen, Nature **431**, 284 (2004).

[33] H. B. Peng, C. W. Chang, S. Aloni, T. D. Yuzvinsky, and A. Zettl, Phys. Rev. Lett. **97** (2006).

[34] J. Cumings, and A. Zettl, Science **289**, 602 (2000).

[35] A. Kis, K. Jensen, S. Aloni, W. Mickelson, and A. Zettl, Phys. Rev. Lett. **97** (2006).

[36] A. M. Fennimore, T. D. Yuzvinsky, W. Q. Han, M. S. Fuhrer, J. Cumings, and A. Zettl, Nature **424**, 408 (2003).

[37] P. Tangney, S. G. Louie, and M. L. Cohen, Phys. Rev. Lett. **93** (2004).

[38] J. Hone, Topics in Applied Physics **80**, 273 (2001).

[39] M. A. Osman, and D. Srivastava, Phys. Rev. B **72** (2005).

[40] J. Hone, B. Batlogg, Z. Benes, A. T. Johnson, and J. E. Fischer, Science **289**, 1730 (2000).

[41] W. Yi, L. Lu, D. L. Zhang, Z. W. Pan, and S. S. Xie, Phys. Rev. B **59**, R9015 (1999).

[42] W. E. Mickelson, Ph.D thesis, in *Physics department* (University of California, Berkeley, 2005).

[43] J. Cumings, Ph.D thesis, in *Physics department* (University of California, Berkeley, 2002).

[44] K. Jensen, W. Mickelson, W. Han, and A. Zettl, Applied Physics Letters **86** (2005).

[45] A. Rubio, J. L. Corkill, and M. L. Cohen, Phys. Rev. B **49**, 5081 (1994).

[46] Z. Wengsieh, K. Cherrey, N. G. Chopra, X. Blase, Y. Miyamoto, A. Rubio, M. L. Cohen, S. G. Louie, A. Zettl, and R. Gronsky, Phys. Rev. B **51**, 11229 (1995).

[47] O. Stephan, P. M. Ajayan, C. Colliex, P. Redlich, J. M. Lambert, P. Bernier, and P. Lefin, Science **266**, 1683 (1994).

[48] J. Cumings, W. Mickelson, and A. Zettl, Solid State Communications **126**, 359 (2003).

[49] J. Cumings, and A. Zettl, Chemical Physics Letters **316**, 211 (2000).

[50] X. Blase, A. Rubio, S. G. Louie, and M. L. Cohen, Europhys. Lett. **28**, 335 (1994).

[51] M. Ishigami, J. D. Sau, S. Aloni, M. L. Cohen, and A. Zettl, Phys. Rev. Lett. **94** (2005).

[52] R. Arenal, O. Stephan, M. Kociak, D. Taverna, A. Loiseau, and C. Colliex, Phys. Rev. Lett. **95** (2005).

[53] E. Hernandez, C. Goze, P. Bernier, and A. Rubio, Phys. Rev. Lett. **80**, 4502 (1998).

[54] N. G. Chopra, and A. Zettl, Solid State Communications **105**, 297 (1998).

[55] L. Duclaux, B. Nysten, J. P. Issi, and A. W. Moore, Phys. Rev. B **46**, 3362 (1992).

[56] E. K. Sichel, R. E. Miller, M. S. Abrahams, and C. J. Buiocchi, Phys. Rev. B **13**, 4607 (1976).

[57] A. Simpson, and A. D. Stuckes, J. Phys. C: Solid State Phys **4**, 1710 (1971).

[58] L. Wirtz, A. Rubio, R. A. de la Concha, and A. Loiseau, Phys. Rev. B **68**, 045425 (2003).

[59] Y. Xiao, X. H. Yan, J. X. Cao, J. W. Ding, Y. L. Mao, and J. Xiang, Phys. Rev. B **69**, 205415 (2004).

[60] W. Q. Han, Y. Bando, K. Kurashima, and T. Sato, Appl. Phys. Lett. **73**, 3085 (1998).

[61] C. Tang, Y. Bando, T. Sato, and K. Kurashima, Chem. Commun., 1290 (2002).

[62] R. S. Lee, H. J. Kim, J. E. Fischer, A. Thess, and R. E. Smalley, Nature **388**, 255 (1997).

[63] M. Bockrath, J. Hone, A. Zettl, P. L. McEuen, A. G. Rinzler, and R. E. Smalley, Phys. Rev. B **61**, 10606 (2000).

[64] W. Q. Han, W. Mickelson, J. Cumings, and A. Zettl, Applied Physics Letters **81**, 1110 (2002).

[65] M. S. Fuhrer, K. Cherrey, A. Zettl, M. L. Cohen, and V. H. Crespi, Phys. Rev. Lett. **83**, 404 (1999).

[66] C. C. Tang, Y. Bando, Y. Huang, S. L. Yue, C. Z. Gu, F. F. Xu, and D. Golberg, J. Am. Chem. Soc. **127**, 6552 (2005).

[67] W. Mickelson, S. Aloni, W. Q. Han, J. Cumings, and A. Zettl, Science **300**, 467 (2003).

[68] W. Q. Han, C. W. Chang, and A. Zettl, Nano Letters **4**, 1355 (2004).

[69] W. Q. Han, and A. Zettl, Applied Physics Letters **84**, 2644 (2004).

[70] R. Peierls, Ann. Phys.-Berlin **3**, 1055 (1929).

[71] H. B. G. Casimir, Physica **5**, 495 (1938).

[72] A. N. Cleland, *Foundations of Nanomechanics* (Springer, 2003).

[73] C. S. Yung, D. R. Schmidt, and A. N. Cleland, Appl. Phys. Lett. **81**, 31 (2002).

[74] T. S. Tighe, J. M. Worlock, and M. L. Roukes, Appl. Phys. Lett. **70**, 2687 (1997).

[75] K. Bradley, S. H. Jhi, P. G. Collins, J. Hone, M. L. Cohen, S. G. Louie, and A. Zettl, Phys. Rev. Lett. **85**, 4361 (2000).

[76] K. Schwab, E. A. Henriksen, J. M. Worlock, and M. L. Roukes, Nature **404**, 974 (2000).

[77] L. G. C. Rego, and G. Kirczenow, Phys. Rev. Lett. **81**, 232 (1998).

[78] S. Berber, Y. K. Kwon, and D. Tomanek, Phys. Rev. Lett. **84**, 4613 (2000).

[79] E. G. Noya, D. Srivastava, L. A. Chernozatonskii, and M. Menon, Phys. Rev. B **70** (2004).

[80] G. Zhang, and B. W. Li, J. Chem. Phys. **123** (2005).

[81] T. Yamamoto, S. Watanabe, and K. Watanabe, Phys. Rev. Lett. **92**, 4613 (2004).

[82] J. Hone, M. Whitney, C. Piskoti, and A. Zettl, Phys. Rev. B **59**, R2514 (1999).

[83] D. J. Yang, Q. Zhang, G. Chen, S. F. Yoon, J. Ahn, S. G. Wang, Q. Zhou, Q. Wang, and J. Q. Li, Phys. Rev. B **66** (2002).

[84] M. J. Biercuk, M. C. Llaguno, M. Radosavljevic, J. K. Hyun, A. T. Johnson, and J. E. Fischer, Appl. Phys. Lett. **80**, 2767 (2002).

[85] P. Kim, L. Shi, A. Majumdar, and P. L. McEuen, Phys. Rev. Lett. **87**, 215502 (2001).

[86] T. Y. Choi, D. Poulikakos, J. Tharian, and U. Sennhauser, Appl. Phys. Lett. **87** (2005).

[87] M. Fujii, X. Zhang, H. Q. Xie, H. Ago, K. Takahashi, T. Ikuta, H. Abe, and T. Shimizu, Phys. Rev. Lett. **95** (2005).

[88] E. Pop, D. Mann, Q. Wang, K. Goodson, and H. J. Dai, Nano Lett. **6**, 96 (2006).

[89] H. Y. Chiu, V. V. Deshpande, H. W. C. Postma, C. N. Lau, C. Miko, L. Forro, and M. Bockrath, Phys. Rev. Lett. **95** (2005).

[90] L. Lu, W. Yi, and D. L. Zhang, Rev. Sci. Instrum. **72**, 2996 (2001).

[91] M. F. Crommie, Ph.D thesis, in *Physics department* (University of California, Berkeley, 1991).

[92] R. L. Powell, H. M. Roder, and W. J. Hall, Physical Review **115**, 314 (1959).

[93] J. Wu, W. Q. Han, W. Walukiewicz, J. W. Ager, W. Shan, E. E. Haller, and A. Zettl, Nano Letters **4**, 647 (2004).

[94] J. Hone, M. Whitney, and A. Zettl, Synth. Met. **103**, 2498 (1999).

[95] D. Y. Li, Y. Wu, R. Fan, P. D. Yang, and A. Majumdar, Appl. Phys. Lett. **83**, 3186 (2003).

[96] D. Y. Li, Y. Y. Wu, P. Kim, L. Shi, P. D. Yang, and A. Majumdar, Appl. Phys. Lett. **83**, 2934 (2003).

[97] D. T. Morelli, J. P. Heremans, and G. A. Slack, Phys. Rev. B **66**, 195304 (2002).

[98] L. Shi, D. Y. Li, C. H. Yu, W. Y. Jang, D. Kim, Z. Yao, P. Kim, and A. Majumdar, J. Heat. Transfer. **125**, 881 (2003).

[99] G. B. M. Fiege, A. Altes, B. Heiderhoff, and L. J. Balk, J. Phys. D-Appl. Phys. **32**, L13 (1999).

[100] J. X. Cao, X. H. Yan, Y. Xiao, and J. W. Ding, Phys. Rev. B **69** (2004).

[101] Y. Xiao, X. H. Yan, J. Xiang, Y. L. Mao, Y. Zhang, J. X. Cao, and J. W. Ding, Appl. Phys. Lett. **84**, 4626 (2004).

[102] D. Golberg, Y. Bando, K. Kurashima, and T. Sato, Solid State Commun. **116**, 1 (2000).

[103] P. G. Collins, K. Bradley, M. Ishigami, and A. Zettl, Science **287**, 1801 (2000).

[104] J. Hone, I. Ellwood, M. Muno, A. Mizel, M. L. Cohen, A. Zettl, A. G. Rinzler, and R. E. Smalley, Phys. Rev. Lett. **80**, 1042 (1998).

[105] P. Kim, L. Shi, A. Majumdar, and P. L. McEuen, Physica B-Condensed Matter **323**, 67 (2002).

[106] D. G. Onn, A. Witek, Y. Z. Qiu, T. R. Anthony, and W. F. Banholzer, Phys. Rev. Lett. **68**, 2806 (1992).

[107] R. K. Kremer, K. Graf, M. Cardona, G. G. Devyatykh, A. V. Gusev, A. M. Gibin, A. Inyushkin, A. Taldenkov, and H. J. Pohl, Solid State Commun. **131**, 499 (2004).

[108] M. AsenPalmer, K. Bartkowski, E. Gmelin, M. Cardona, A. P. Zhernov, A. V. Inyushkin, A. Taldenkov, V. I. Ozhogin, K. M. Itoh, and E. E. Haller, Phys. Rev. B **56**, 9431 (1997).

[109] P. C. Collins, M. S. Arnold, and P. Avouris, Science **292**, 706 (2001).

[110] T. D. Yuzvinsky, W. Mickelson, S. Aloni, S. L. Konsek, A. M. Fennimore, G. E. Begtrup, A. Kis, B. C. Regan, and A. Zettl, Appl. Phys. Lett. **87** (2005).

[111] A. Bachtold, C. Strunk, J. P. Salvetat, J. M. Bonard, L. Forro, T. Nussbaumer, and C. Schonenberger, Nature **397**, 673 (1999).

[112] U. C. Coskun, T. C. Wei, S. Vishveshwara, P. M. Goldbart, and A. Bezryadin, Science **304**, 1132 (2004).

[113] T. D. Yuzvinsky, A. M. Fennimore, W. Mickelson, C. Esquivias, and A. Zettl, Applied Physics Letters **86** (2005).

[114] S. Paulson, M. R. Falvo, N. Snider, A. Helser, T. Hudson, A. Seeger, R. M. Taylor, R. Superfine, and S. Washburn, Appl. Phys. Lett. **75**, 2936 (1999).

[115] B. Shan, G. W. Lakatos, S. Peng, and K. J. Cho, Appl. Phys. Lett. **87** (2005).

[116] O. Gulseren, T. Yildirim, S. Ciraci, and C. Kilic, Phys. Rev. B **65** (2002).

[117] M. S. Fuhrer, J. Nygard, L. Shih, M. Forero, Y. G. Yoon, M. S. C. Mazzoni, H. J. Choi, J. Ihm, S. G. Louie, A. Zettl, and P. L. McEuen, Science **288**, 494 (2000).

[118] M. C. Llaguno, J. E. Fischer, A. T. Johnson, and J. Hone, Nano Lett. **4**, 45 (2004).

[119] H. E. Romero, K. Bolton, A. Rosen, and P. C. Eklund, Science **307**, 89 (2005).

[120] Y. H. Kim, K. J. Chang, and S. G. Louie, Phys. Rev. B **6320** (2001).

[121] P. Poncharal, Z. L. Wang, D. Ugarte, and W. A. de Heer, Science **283**, 1513 (1999).

[122] J. Cumings, and A. Zettl, Phys. Rev. Lett. **93** (2004).

[123] J. S. Russell, 311 (1844).

[124] H. A. Haus, and W. S. Wong, Rev. Mod. Phys. **68**, 423 (1996).

[125] A. R. Osborne, and T. L. Burch, Science **208**, 451 (1980).

[126] H. A. M. Degronckel, W. J. M. Dejonge, K. Kopinga, and L. F. Lemmens, Phys. Rev. B **44**, 4654 (1991).

[127] T. Iizuka, and M. Wadati, J. Phys. Soc. Jpn. **61**, 3077 (1992).

[128] S. Sakai, M. R. Samuelsen, and O. H. Olsen, Phys. Rev. B **36**, 217 (1987).

[129] P. Woafo, Phys. Rev. E **58**, 1033 (1998).

[130] T. Y. Astakhova, O. D. Gurin, M. Menon, and G. A. Vinogradov, Phys. Rev. B **6403** (2001).

[131] A. V. Savin, and O. I. Savina, Phys. Solid State **46**, 383 (2004).

[132] K. Jensen, C. Girit, W. Mickelson, and A. Zettl, (to be published).

[133] W. C. Fon, K. C. Schwab, J. M. Worlock, and M. L. Roukes, Nano Lett. **5**, 1968 (2005).

[134] P. L. Richards, J. Appl. Phys. **76**, 1 (1994).

[135] D. R. Schmidt, C. S. Yung, and A. N. Cleland, Appl. Phys. Lett. **83**, 1002 (2003).

[136] W. Feist, J. Schnieders, V. Dorer, and A. Haas, Energy Build. **37**, 1186 (2005).

[137] S. C. M. Hui, Renew. Energy **24**, 627 (2001).

[138] S. Lepri, R. Livi, and A. Politi, Phys. Rep. **377**, 1 (2003).

[139] Z. Rieder, J. L. Lebowitz, and E. Lieb, J. Math. Phys. **8**, 1073 (1967).

[140] A. Casher, and J. L. Lebowitz, J. Math. Phys. **12**, 1701 (1971).

[141] B. B. Hu, B. W. Li, and H. Zhao, Phys. Rev. E **61**, 3828 (2000).

[142] C. Giardina, R. Livi, A. Politi, and M. Vassalli, Phys. Rev. Lett. **84**, 2144 (2000).

[143] O. Narayan, and S. Ramaswamy, Phys. Rev. Lett. **89**, 200601 (2002).

[144] S. Lepri, R. Livi, and A. Politi, Phys. Rev. Lett. **78**, 1896 (1997).

[145] R. Livi, and S. Lepri, Nature **421**, 327 (2003).

[146] R. J. Rubin, and W. L. Greer, J. Math. Phys. **12**, 1686 (1971).

[147] K. Aoki, and D. Kusnezov, Phys. Rev. Lett. **86**, 4029 (2001).

[148] P. Grassberger, W. Nadler, and L. Yang, Phys. Rev. Lett. **89** (2002).

[149] G. Zhang, and B. W. Li, J. Chem. Phys. **123**, 114714 (2005).

[150] D. Segal, and A. Nitzan, Phys. Rev. Lett. **94**, 034301 (2005).

[151] M. Terraneo, M. Peyrard, and G. Casati, Phys. Rev. Lett. **88**, 094302 (2002).

[152] A. Majumdar, Science **303**, 777 (2004).

[153] L. D. Hicks, and M. S. Dresselhaus, Phys. Rev. B **47**, 12727 (1993).

[154] L. D. Hicks, and M. S. Dresselhaus, Phys. Rev. B **47**, 16631 (1993).